Image Segmentation in Microscopic Single Cell Analysis

By

Mischa Dominik Schwendy

DISSERTATION

MAX PLANCK INSTITUTE FOR POLYMER RESEARCH

JOHANNES GUTENBERG-UNIVERSITY MAINZ

MAX PLANCK GRADUATE CENTER

2018

Dissertation zur Erlangung des Grades eines doctor rerum naturalium (Dr. rer. nat.) der Fachbereiche

08 - Physik, Mathematik und Informatik,
09 - Chemie, Pharmazie und Geowissenschaften,
10 - Biologie und Universitätsmedizin

der Johannes Gutenberg-Universität Mainz.

Supervisors:

Prof. Dr. Mischa Bonn, Max Planck Institute for Polymer Research
Dr. Ronald Unger, Universitätsmedizin der Johannes Gutenberg-Universität Mainz
Prof. Dr. Sapun Parekh, University of Texas at Austin/Max Planck Institute for Polymer Research

Declaration:

I hereby declare that I wrote the dissertation submitted without any unauthorized external assistance and used only sources acknowledged in the work. All textual passages which are appropriated verbatim or paraphrased from published and unpublished texts as well as all information obtained from oral sources are duly indicated and listed in accordance with bibliographical rules. In carrying out this research, I complied with the rules of standard scientific practice as formulated in the statutes of Johannes Gutenberg-University Mainz to insure standard scientific practice.

Mischa Schwendy

ISBN:

Publications covered in this thesis

Chapter 3

Mischa Schwendy, Ronald E. Unger, Mischa Bonn, Sapun H. Parekh. *Automated cell segmentation in FIJI® using the DRAQ5 nuclear dye.* Submitted.

Chapter 4

Mischa Schwendy, Ravi Dhiman, Ronald E. Unger, Mischa Bonn, Sapun H. Parekh. *Intracellular lipid accumulation in THP-1 derived macrophages is substrate stiffness dependent.* In preparation.

Chapter 5

Mischa Schwendy, Ronald E. Unger, Mischa Bonn, Sapun H. Parekh. *EVICAN – Expert Visual Cell Annotation.* In preparation.

Other publications

Zhijun Chen, Raweewan Thiramanas, Mischa Schwendy, Chaoming Xie, Sapun H. Parekh, Volker Mailänder, & Si Wu (2017). *Upconversion Nanocarriers Encapsulated with Photoactivatable Ru Complexes for Near-Infrared Light-Regulated Enzyme Activity*. Small, 13(46), 1700997.1

Frederik Fleissner, Sabine Pütz, Mischa Schwendy, Mischa Bonn, Sapun H. Parekh (2017). *Measuring Intracellular Secondary Structure of a Cell-Penetrating Peptide in Situ.* Analytical chemistry, 89(21), 11310-11317.

For my parents.

Thank you for your support, your guidance, and your love!

Abstract

Since its inception, microscopy has been primarily used as a qualitative tool to explore the previously imperceptible microcosmos. However, microscopy images not only provide qualitative features, but can also be used to extract quantitative measures. Nowadays, cell microscopy images in digital form can be processed to extract quantitative information on cell morphology, e.g. spreading area, circularity of cellular outlines, and elongation. The central idea behind this thesis was to analyze how the stiffness upon which macrophage cells grew influenced intracellular lipid accumulation. To achieve this goal, automated methods for image segmentation and analysis that produced accurate cellular outlines needed to be developed and cytosolic lipid volumes measured in 3D in confocal microscopy image stacks.

Identifying cellular outlines in confocal microscopy images is the topic of chapter 3. The adherent cell lines THP-1 (phorbol 12-myristate 13-acetate/PMA-differentiated), HeLa, and CHO were stained with the nuclear dye DRAQ5 and confocal microscopy stacks were acquired. Z-projecting the nuclear signal image stack resulted in a 2D image with strong signal intensities in the nucleus and weak signal intensities in the cytosol regions. An automated algorithm implementing adaptive background subtraction, thresholding, and watershedding was created to accurately segment single cells (i.e. determine individual cellular outlines) within the images according to their weak cytosolic and strong nuclear signal. Evaluating the segmentation algorithm showed 86 % of the segmented cells correctly and an average intersection over union score of 0.83. These values were on par with comparable modern image segmentation algorithms. Using the algorithm to monitor THP-1 cell morphology during PMA-induced differentiation showed two phases of increasing cell area (24 – 48 h and after 120 h) with the second growth phase that was correlated to cell elongation. In a second application, CHO cell spreading area was shown to decrease by more than 40 % during low-temperature cell culture (31°C instead of 37°C).

Chapter 4 addresses the question of whether lipid accumulation in macrophages is dependent on the mechanical microenvironment. In this sub-project, hydrogel cell culture was used to mimic mechanical differences in atherosclerotic plaque development *in vitro,* and cells were fed a lipoprotein-rich medium. Atherosclerosis is a lifelong disease triggered by lipid-rich diets, which results in plaque development (containing lipid-rich material) within the arterial wall. This plaque consists of a soft lipid-rich necrotic core, various cell types, with a majority being lipid-laden macrophages (so-called “foam cells”), and an outer shell of smooth muscle cells that contribute to a remodeled and stiffer tissue environment. To assess whether foam cell development is influenced by tissue stiffness, THP-1-derived macrophages were cultured on collagen-coated polyacrylamide hydrogels of varying stiffness with medium containing aggregated low-density lipoprotein (LDL). 3D confocal microscopy stacks of stained intracellular lipids and nuclei were acquired, 2D cellular outlines were detected using the segmentation-algorithm created in Chapter 3. The detected cell frames were applied to the individual frames in the lipid image stack and lipid signals within the cell frames quantified in each microscopic slice (i.e. volumetrically). Thus, lipid volumes for individual cells could be quantified and categorized, which enabled the identification of the foam cell subpopulation. Comparing the foam cell subpopulation on substrates ranging in stiffness from 4 kPa (comparable to lipid-rich regions in the necrotic core) to 50,000 kPa (glass substrate), an increasing foam cell subpopulation from 10 to above 30 % was observed. The enhancement of foam cell formation correlated with an amplified expression of the scavenger receptor A and CD36 (two prominent LDL receptors) as substrate stiffness increased.

Chapter 5 describes the creation of a machine learning assisted computer vision algorithm for cell and nucleus segmentation and classification (i.e. identification of the segmented object as either “cell” or “nucleus”) in **unstained** microscopy images. Like many current computer vision algorithms, the implementation in this final project was based on convolutional neural networks (CNN). CNNs extract image features based on self-trained convolution filters. Training of a CNN-based algorithm requires large amounts of annotated image data (i.e. manually segmented cells and nuclei in example images). In this final project, a large-scale annotated image dataset containing more than 4,600 brightfield and phase contrast images with ~53,000 annotated cells and nuclei was assembled. Applying the annotated training dataset, a computer vision algorithm was created with an average precision exceeding 58 % (at IoU thresholds of 0.5), reaching precision values comparable to modern every-day scene classification- and segmentation-algorithms.

In summary, my work contributed methodologically to efficient image processing in microscopy and cell biology by delivering algorithms for cell segmentation, classification, and volumetric quantification. There is a clear potential for these methods in cell biology as clearly demonstrated and the applicability of efficient image processing going forward will only increase in the future.

Zusammenfassung

Seit Beginn der Mikroskopie, wurde die Methode hauptsächlich für die qualitative Erforschung des vorher nicht wahrnehmbaren Mikrokosmos genutzt. Allerdings bietet Mikroskopie nicht nur qualitative Merkmale, sondern kann auch für quantitative Messungen genutzt werden. In der heutigen Zeit können digitale zellmikroskopische Bilder prozessiert werden um quantitative Informationen über die Zellmorphologie zu extrahieren, wie z.B. zelluläre Flächenausbreitung, Rundheit des Umrisses und Ausdehnung. Der Kerngedanke dieser Dissertation war es, die Abhängigkeit der zellulären Lipidakkumulation von der Steifheit des Kultursubstrats zu analysieren. Um dieses Ziel zu erreichen, mussten automatisierte Methoden zur präzisen Zellumriss-Segmentation und -Analyse in Mikroskopbildern entwickelt und cytosolische Lipidvolumina dreidimensional in konfokal-mikroskopischen Aufnahmen gemessen werden.

Die Identifikation der Zellumrisse in konfokal-mikroskopischen Aufnahmen ist Thema in Kapitel 3 dieser Thesis. Die adhärent wachsenden Zelllinien THP-1 (differenziert mittels Phorbol-12-myristat-13-acetat/PMA), HeLa und CHO wurden mit dem Nukleus-färbenden Fluoreszenzfarbstoff DRAQ5 angefärbt und schichtweise volumetrische Bildaufnahmen mittels Konfokal-Mikroskopie angefertigt. Durch eine Z-Projektion des schichtweise aufgenommenen Nukleussignals, entstand ein zweidimensionales Bild mit starker Signalintensität im Nukleus und schwacher Signalintensität in cytosolischen Regionen. Ein vollautomatisierter Algorithmus auf der Basis von adaptiver Hintergrundsubtraktion, Schwellenwertverfahren und Watershed-Prozessierung wurde erstellt, um einzelne Zellen innerhalb des Bildes anhand ihres cytosolischen und Nukleus-Signals zu segmentieren (d.h. die individuellen Zellumrisse zu bestimmen). Die Evaluation des Segmentationsalgorithmus ergab 86 % korrekt segmentierte Zellen und ein Schnittmengen-zu-Vereinigungsmengen-Verhältnis von 0.83. Diese Werte waren auf einer Stufe mit vergleichbaren modernen Segmentationsalgorithmen. Mittels des Algorithmus beobachtete, morphologische Zellveränderungen während PMA-induzierter Differenzierung von THP-1 Zellen ergaben ein zweiphasiges zelluläres Flächenwachstum (24 – 48 h und nach 120 h) sowie eine korrelierende Zellausdehnung nach 120 h. In einer zweiten Anwendung konnte eine 40 % reduzierte Zellfläche von CHO Zellen bei niedriger Kultivierungstemperatur nachgewiesen werden (31°C anstatt 37°C).

Kapitel 4 behandelt die Frage, ob Lipidakkumulation in Makrophagen von der Steifheit des Kultursubstrats abhängig ist. In diesem Teilprojekt wurde Hydrogel-Zellkultur eingesetzt um mechanische Gewebeveränderungen während der Entstehung atherosklerotischer Plaques *in vitro* zu imitieren und die Zellen mit Lipoprotein-reichem Medium versetzt. Atherosklerose ist eine lebenslange Krankheit, die durch fettreiche Ernährung ausgelöst wird, wobei sich eine fettreiche Ablagerung innerhalb der Arterienwand entwickelt. Diese Ablagerung besteht aus einem weichen, fettreichen, nekrotischen Kern, diversen Zelltypen mit einer Mehrheit aus fettreichen Makrophagen (sogenannten „Schaumzellen“) sowie einer äußeren Hülle aus glatten Muskelzellen, die zur Ausbildung von neugeformtem steiferem Gewebe beitragen. Um zu beurteilen, ob die Schaumzellentstehung von der Gewebesteifheit beeinflusst wird, kultivierte ich aus THP-1 entwickelte Makrophagen auf Collagen-beschichteten Polyacrylamid-Hydrogelen unterschiedlicher Steifheit mit aggregierten low-density Lipoproteinen (LDL). 3D konfokal-mikroskopische Schichtaufnahmen angefärbter intrazellulärer Lipide und Nuklei wurden angefertigt und zweidimensionale Zellumrisse mittels des Segmentationsalgorithmus aus Kapitel 3 detektiert. Die erfassten Zellumrisse wurden auf die einzelnen Lipidsignal-

Schichten projiziert und Lipidsignale innerhalb der Zellrahmen schichtweise quantifiziert (d.h. volumetrisch). Auf diese Weise konnten Lipidvolumina in den Zellen individuell quantifiziert und kategorisiert werden, was die Identifikation der Schaumzell-Subpopulation ermöglichte. Beim Vergleich der Schaumzell-Subpopulationen auf Substraten der Steifheit 4 kPa (vergleichbar zu fettreichen Regionen im nekrotischen Kern) bis 50000 kPa (Glassubstrat) beobachtete ich eine steigende Schaumzell-Subpopulation von 10 auf über 30 %. Die gesteigerte Schaumzellbildung korrelierte mit verstärkter Expression von scavenger receptor A und CD36 (zwei bedeutende LDL Rezeptoren) bei steigernder Substratsteifheit.

Kapitel 5 beschreibt die Erzeugung eines maschinelles Lernen-gestützten Computervision-Algorithmus für Zell- und Nukleussegmentation sowie -klassifizierung (d.h. Identifizierung des segmentierten Objekts als „Zelle“ oder „Nukleus“) in **ungefärbten** Mikroskopieaufnahmen. Wie viele moderne Computervision-Algorithmen, war auch die Implementierung in meinem letzten Projekt auf convolutional neural networks (CNN) gestützt. Anhand von selbst erlernten Filtern extrahieren CNNs Strukturen aus Bildern. Die Ausbildung eines CNN-basierenden Algorithmus erfordert große Mengen an annotierten Bilddaten (z.B. manuell segmentierte Zellen und Nuklei in Beispielbildern). In diesem letzten Projekt stellte ich eine großmaßstäbliche annotierte Bilddatenbank zusammen, die mehr als 4600 hellfeld- und phasenkontrastmikroskopische Aufnahmen mit ~53000 annotierten Zellen und Nuklei beinhaltet. Mithilfe dieses annotierten Datensets erstellte ich einen Computervision-Algorithmus mit einer durchschnittlichen Präzision von über 58 % (bei Schnittmengen-zu-Vereinigungsmengen-Grenzwerten von 0.5). Damit erreichte ich Präzisionswerte, die mit modernen Klassifizierungs- und Segmentations-Algorithmen für Alltagsszenen vergleichbar sind.

Zusammenfassend hat meine Arbeit methodologisch zur effizienten Bildverarbeitung in der Mikroskopie und Zellbiologie beigetragen, da Algorithmen zur Segmentation und Klassifizierung sowie der volumetrischen Quantifizierung bereitgestellt wurden. Wie ich zeigen konnte, gibt es bereits ein deutliches Potential für diese Methoden in der Zellbiologie und gesteigerte Anwendungsmöglichkeiten von effizienter Bildverarbeitung sind auch in Zukunft zu erwarten.

Contents

1 Introduction

1.1 Structure of this thesis

This thesis covers three research projects that I completed during my PhD studies in microscopic image analysis. In the first project, I created a hard-coded image processing algorithm that segments cells after fluorescent nuclear staining. The established algorithm was subsequently used in the second project to determine intracellular lipid accumulation in macrophages cultured on hydrogels of varying stiffness. Lastly, a cutting-edge computer vision algorithm was created to segment cells in unstained brightfield and phase contrast microscopy images.

Chapter 1 establishes the background knowledge for the topics covered in this thesis. First, characteristics of cellular morphology are introduced and an overview on influences of substrate properties on the shape of cultured cells is given. Subsequently, atherosclerotic plaque development is described on a cellular level with a focus on lipid uptake and mechanical remodeling of the extracellular matrix during the disease. Then, fundamentals of light and fluorescence microscopy, spatial resolution, and historic technical advancements in microscopic imaging are presented. Lastly, an introduction to the concept of machine learning in image processing is given with information about image dataset generation, algorithm training and evaluation.

Chapter 2 reviews the applied methods within this thesis: Cell culture and manipulation (using hydrogel culture and cytoskeletal drugs), as well as cell staining with small molecule probes and immunofluorescence with antibodies. In addition, it describes applied microscopic techniques and training of a machine learning based computer vision algorithm with a focus on dataset generation, model training and segmentation evaluation.

Chapter 3 describes how to implement an accurate and automated hard-coded algorithm for quantification of cell shape changes. This algorithm was subsequently used to observe cell morphology and spreading area during cellular maturation using a single nuclear dye together with the software ImageJ. (Publication 1)

Chapter 4 focuses on the quantitative characterization of foam cell generation by lipid loading and the influence of tissue substrate stiffness, *in vitro*, using the automated image analysis module from Chapter 3 for analysis. (Publication 2)

Chapter 5 displays the segmentation and characterization capabilities of a cutting-edge machine learning-based cell-detection algorithm. The Chapter ends with a discussion about the importance of appropriate datasets and a need for accurate preparation steps to produce an annotated image dataset for training, validation and evaluation of computer vision algorithms. (Publication 3)

Chapter 6 gives an outlook on future directions in the fields of atherosclerotic research and image processing.

1.2 Overview

Microscopy, since its inception over 350 years ago has been a qualitative method. The technique was essential to enlighten the, at the time, unrecognized cosmos of microorganisms[1] and the concept of cells as the smallest living units of a body[2]. Over the next centuries, microscope manufacturing underwent dramatic improvements: The problem of chromatic aberration was solved by Chester More Hall in the 1730's[3]. Abbe discovered in the 1870's that the resolution of a microscope depends on the wavelength of light and the numerical aperture of the light capturing system[4], which paved the way for the production of microscopes with mathematically defined resolution powers together with Carl Zeiss. The rise of phase contrast techniques[5], invented by Fritz Zernike, was another milestone for light microscopy. After these manufacturing and technological advancements, the focus was directed to signal specificity and spatial resolution enhancement. Specific dyes as well as genetically encoded biosensors, such as the green fluorescent protein[6], allowed for precise determination of cellular entities within a microscopic image, often even in live-cell experiments. Resolution enhancement was achieved by using electron microscopes with electrons that have much shorter wavelengths[7] compared to visible light and therefore enabled higher resolution as determined by the physical diffraction limit. However, improved spatial resolution came with a major drawback: electron beams only travel in ultra-high vacuum, which significantly limited the biological applications to non-living (and extremely dry) states. Recent breakthroughs in superresolution fluorescence microscopy, most notably the concepts of stimulated emission depletion[8] and localization microscopy[9], circumvented the diffraction limit in fluorescence microscopy. This allowed scientists to observe cellular processes at the nanoscale with specific staining and fluorescent proteins even in live-cell microscopy[10,11].

In addition to sharp images of cellular (and subcellular) features, microscopy also offers remarkable opportunities for quantitative interpretation, as objects within an image can be directly linked to their actual length scale and fluorescence intensity can be correlated to a fluorophore's abundance at the location of the signal. The concept of quantitative microscopy has been growing over the last two decades, with most measurements relying on quantification of fluorescence *intensity* within the sample. If segmentation was performed, it was either based on previous fluorescent staining of the sample or even performed manually.

In my doctoral thesis projects, I explored how to use microscopic imaging techniques not only for quantitative measurements, but also for subsequent cellular characterization. The main scientific objective was to elucidate how macrophage lipid uptake behavior was influenced by substrate stiffness with an image-based approach to identify different cell sub-populations based on lipid uptake and cell morphology. As arterial stiffening is a naturally occurring process in the onset of atherosclerotic heart disease, a possible interplay of matrix remodeling and amplified cellular lipid uptake is expected. Substrate stiffness is a known driving force of cell morphology, often guiding cell spreading area by interfering with the cytoskeleton. Conventional quantification methods rely on extraction of lipids from large cell populations, associating the per cell values to a population-based average lipid uptake. Microscopy-based quantification, however, allows for single cell observations and therefore monitoring of subpopulations such as extremely lipid-rich cells.

For this purpose, I generated computational methods to automatically segment microscopic images of cultured cells stained for nuclei and lipids. Based on extracted values, I was able to characterize cellular morphology by means of spreading area, elongation, and circularity. The

segmented cell frames, together with lipid signals in stained cell samples could in turn be used to quantify lipid volumes within individual cells, defining lipid volume thresholds for the characterization of foam cells. Comparing the macrophage populations cultured on soft substrates with the populations cultured on stiff substrates enabled me to identify the lipid laden foam cells as subpopulations within each culture condition. Although this subpopulation makes up a small fraction of cells cultured on soft substrates, the fraction grows substantially when macrophages are cultured on glass. Flow cytometry (FC) analysis identified the scavenger receptor A as a driving force behind this finding.

The established hard-coded algorithm for segmentation of fluorescently stained cells in microscopy images enabled a downstream characterization of cell subpopulations according to their intracellular lipid accumulation. The next goal was to develop a combined approach, in which segmentation and characterization was coupled in a single image processing step (i.e. without a need for manual characterization *after* image processing). For this purpose, I employed a convolutional neural network-based computer vision algorithm (explained in detail in the next chapter) that performs image segmentation and classification according to convolution matrices (image filters that are set to highlight features in an image, e.g. edge-filter). The numerical values in the convolution matrices are designed by the algorithm itself in a "training" phase, during which it "learns" to detect object features from a provided dataset of manually labeled example images. The computer vision concept was applied to segment cell bodies and nuclei in **unstained** microscopy images and characterized the segmented area as either "cell" or "nucleus" (= "class labels", objects distinguishable by a classification algorithm). In the course of this final project, I assembled a large-scale cell imaging pipeline to acquire an image collection with partially segmented and labelled cells and nuclei in each image (= "ground truth", manually labelled data that is regarded as the true state). This was necessary, as convolutional neural network-based algorithms require thousands of training images to adapt meaningful convolution matrices. The cell/nucleus image collection will be made freely available, to increase the creation of computer vision algorithms in the field of microscopy.

1.3 Cellular shape and the role of microenvironments

All higher organisms are composed of cells that live in association with and are dependent on one another. The degree of this association varies according to the hierarchical structure of the cellular community. In the human body, cells can be organized as forms such as organs, nerves, vessels and layers, and therefore exhibit different characteristics based on factors such as dimensionality, mechanical properties, chemical and physical conditions. Cellular shapes and even functions are influenced by these environmental factors. However, naturally occurring factors like cyclic blood pressure, substrate stiffness, or tissue tension during movement are difficult to reproduce under laboratory cell culture conditions and often complicate scientific measurements. In this thesis, the biological focus is on cell shape quantification and substrate stiffness-mediated effects on macrophage lipid uptake, mimicking the onset of atherosclerotic heart disease. This chapter will introduce the significance of cell shape and its influence on cellular phenotype and vice versa. Additionally, an overview of the pathogenesis of atherosclerosis and associated effects on the microenvironment is given.

1.3.1 The cytoskeleton

The cytoskeleton is a network of proteins that provides shape to the cell, organizes structures in the cytosol via vesicle transport and organelle anchorage, and provides mechanical resistance to deformation. The cytoskeletal architecture in mammalian cells is formed by three different polymers:

- Filamentous actin: A flexible polymer with a diameter of 8 nm[12] that has a role in intracellular transport, cell movement[12], cell shape[12], and internalization of membrane vesicles[13]. Concentration is highest in the cell cortex[12].
- Microtubuli: Stiff cylindrical polymers, forming hollow fibers with a diameter of 25 nm[12]. Microtubules are organized in a microtubule-organizing center and from there stretch throughout the cell[12]. The fibers have a role in intracellular transport[14] and form the mitotic spindle[12,15].
- Intermediate filaments: Ropelike polymers with a diameter of 10 nm[12]. Supports the cell by providing mechanical strength[12,16]

F-actin and microtubules are composed of the units actin and tubulin (α-tubulin-β-tubulin dimers), respectively[12], from which the names are also derived. In contrast, intermediate filaments are cytoskeletal structures consisting of a large variety of proteinogenic subunits[12]. **Figure 1** schematically displays F-actin, microtubules, and intermediate filaments in a cell.

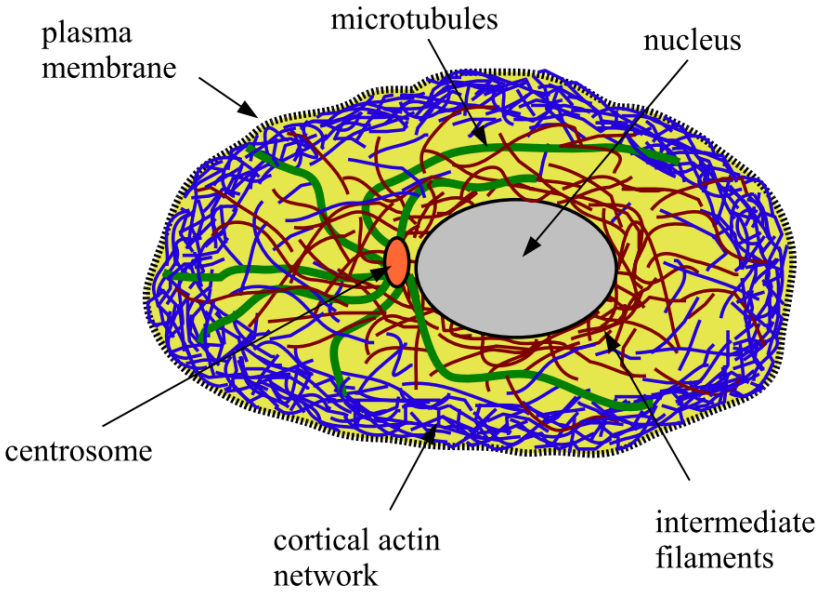

Figure 1 Cytoskeletal networks in a cell (image from [17])
Microtubuli (green) are hollow tubes and form long polymers throughout the cytosol, that serve as intracellular "highways" for motorproteins that transport vesicles or organelles. Intermediate filaments (red), form a meshwork around the nucleus, providing mechanical strength. Actin filaments (blue) in cellular protrusions are assembled as filamentous networks that guide cellular movement and spreading as well as force generation.

Assembly and disassembly of the cytoskeletal network are continuous processes within the cell and are controlled by several regulatory protein classes, such as nucleation-promoting factors (that initiate filament formation), capping proteins (terminate filaments), polymerases (accelerate filament growth), depolymerizing and severing factors (disassemble filaments), and crosslinkers as well as stabilizing proteins (organize higher network-structures)[15].

Filamentous actin and especially microtubules serve as transport "highways" for travel by motor proteins such as kinesins and dyneins (microtubules) as well as myosins (filamentous actin)[12]. These motor proteins are involved in the transportation of vesicles, organelles, and are the driving force for movement within the cell.

The cytoskeleton is also the component of the cell that “feels” mechanical properties of the extracellular matrix or other extracellular forces by translating inputs such as substrate stiffness or pressure into intracellular biochemical signals and ultimately downstream cell responses. Receiving mechanical stimuli that spark a cellular reaction is known as “mechanotransduction”. This is of particular interest in cells that exist in various mechanical locations throughout the body or in tissues that undergo a mechanical transition such as in development or in disease progression. The importance of mechanotransduction as a guiding force in the context of cellular morphology is presented in the following section.

1.3.2 Cellular morphology and substrate influence

Cells are highly heterogeneous entities that can morph into various shapes, depending on the substrate they are cultured on, the availability of nutrients and chemical substances (e.g. in cell migration studies), as well as the degree of confluency to which they are cultured. This makes it difficult to define effective shape descriptors for each cell line. However, trends are visible for cell lines, which are often associated with their original function in the body. For instance, in **Figure 2** three adherent cell lines are displayed: NIH/3T3, MCF-7, and RAW 264.7. NIH/3T3 is an embryonic fibroblast cell line that does not form confluent monolayers. They connect to each other via their cytoplasmic extensions and are known to synthesize the extracellular matrix for connective tissues in the body. In contrast, epithelial cells (like MCF-7) that form connected layers to cover structures within the body, show extended cell spreading and tend to assemble in colonies or monolayers. Lastly, RAW 264.7 cells, here exhibiting an early macrophage phenotype, are small and spherical, which helps as they migrate through dense tissues towards locations of inflammation.

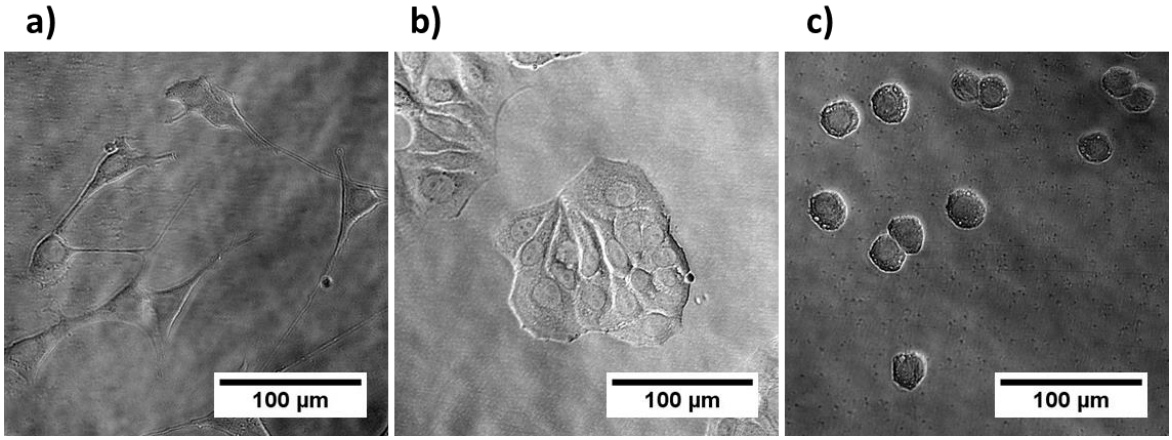

Figure 2 Examples for different shape characteristics in three cell lines

Qualitative shape features include: a) elongated, fibroblast-like growth (NIH/3T3 cells); b) regular epithelial-like growth without the formation of pseudopodia and often with a tendency to form small colonies, even at low confluency (MCF-7 cells); c) small, spherical shape (RAW 264.7 cells). All cells cultured on tissue culture polystyrene.

The occurance of specific cell shape changes can also reflect differentiation states[18–20]. Cell shape can be tuned via printed micropatterns[20,21] that restrict the available spreading area of seeded cells, changes in substrate stiffness that lead to reduced adhesion of many cell types[19,22,23], and chemical interference with the cytoskeleton (e.g. via Latrunculin A, Blebbistatin, or Colchicine). While chemical influences on cells have been subject to broad research, the influence of mechanotransduction from the microenvironment on cell shape have only recently begun to receive significant attention. Since the range of stiffness in the body spans a broad range from below 1 kPa within brain tissue to above 100 kPa in bone (**Figure 3a**), it is not surprising that cells exhibit varying morphology and phenotype characteristics, depending on their surrounding mechanical environment. Cell types that occur in numerous different microenvironments within the body are of special interest due to their morphology-induced differentiation. Engler *et al.*[19] cultured human mesenchymal stem cells (HMSC) on hydrogels of varying stiffness to analyze their lineage fate. HMSCs cultured on 0.1 – 1 kPa hydrogels mimicking brain tissue elasticity levels adopted a neurogenic phenotype, cultivation on 8 – 17 kPa hydrogels imitating muscle tissue stiffness resulted in a myogenic appearance, and lastly culturing cells on 25 – 40 kPa hydrogels approaching bone stiffness lead to an osteogenic morphology (**Figure 3b**).

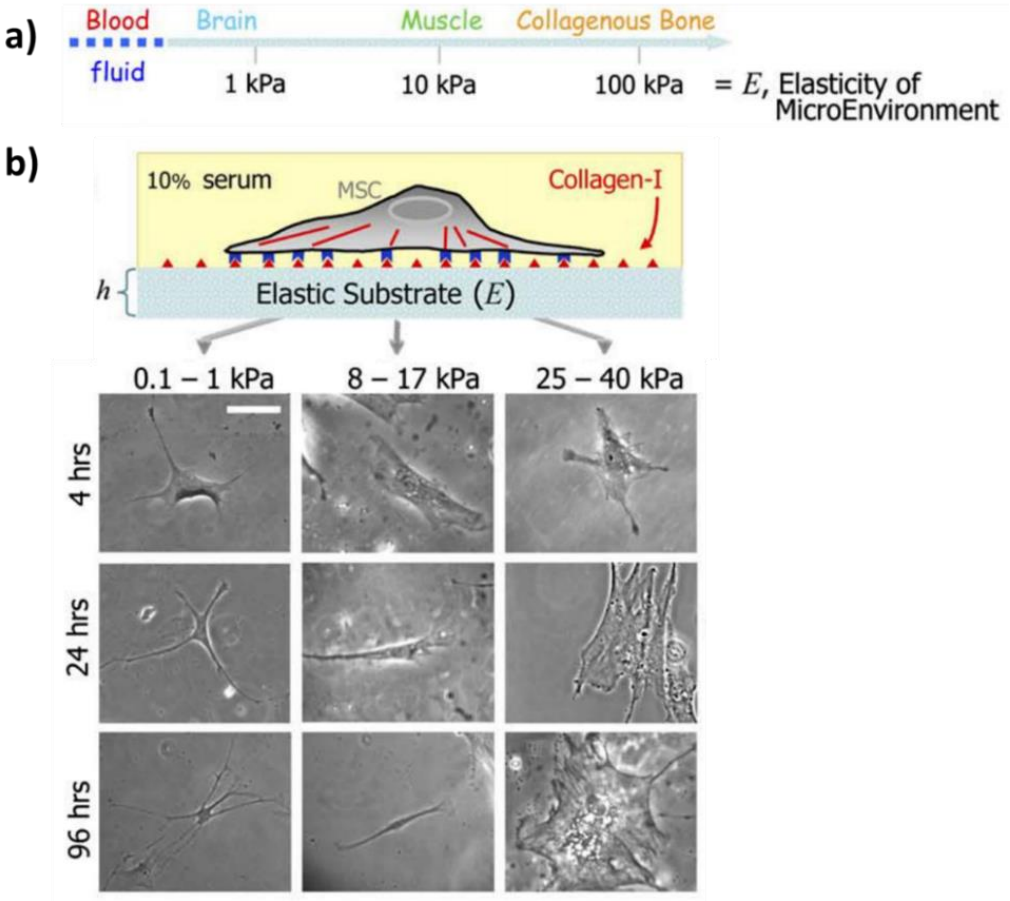

Figure 3 Cell morphology heterogeneity guided by substrate stiffness(adapted from[19])

a) Different stiffness regimes in the human body spanning several orders of magnitude from below 1 kPa to more than 100 kPa in bone tissues. b) Mesenchymal stem cells cultured on hydrogels of varying stiffness adopt different morphologies matching cell types present in the body's stiffness regime.

Stem cells are of particular interest, as they play a pivotal role in organism development and can adopt several different phenotypes depending on their environment. In addition to stem cells, immune cells, particularly macrophages that must migrate within tissues in order to fight foreign bodies, are subject to numerous different microenvironments. These cells are derived from monocytes floating throughout the blood stream and become chemo-attracted to diverse tissues in the body where they then differentiate to macrophages in response to inflammation markers.

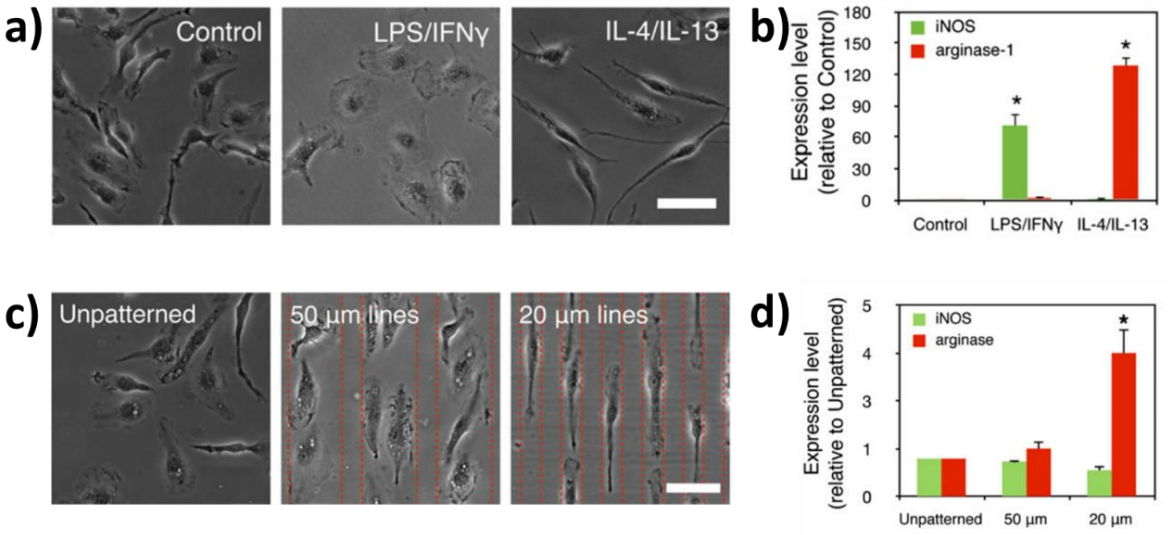

Figure 4 macrophage polarization guided by micropatterning (adapted from[20])

a) Effect of chemical polarization on macrophages: Heterogeneous morphology of unpolarized macrophages (left), pan-fried egg shape of proinflammatory M1 macrophages activated with lipopolysaccharides (middle), and elongated shape of anti-inflammatory M2 macrophages exposed to interleukin 4 and 13 (right). b) Verification of the activated state with expression levels of inducible nitric oxide synthase (iNOS) and arginase-1 (marker for M1 and M2 activation, respectively). c) Effect of micropatterns on macrophages: Heterogeneous morphology on unpatterned substrate (left), increasing degree of elongation with narrowing of patterned lines from 50 (middle) to 20 µm (right). d) Expression levels of iNOS and arginase-1 in cells on micropatterned substrates: Narrow lines lead to increasing M2 polarization phenotype.

Recent studies have pointed out that macrophage morphology and behavior are susceptible to the substrate topography[20,21,24]. When macrophages are forced to elongate, using micropatterned lines coated with the extracellular matrix proteins they exhibited a phenotype corresponding to anti-inflammatory polarization (see **Figure 4**).[20] This proved that cellular shape alone can also guide cell function, instead of cellular function dictating cell shape. The ability to influence cell function makes substrate mechanics and topography an interesting tool for cell behavior and morphology analysis. The following section introduces a special case of mechanical microenvironmental remodeling, which happens in arterial walls during disease state: atherosclerosis.

1.3.3 Atherosclerosis and lipid uptake of macrophages

Atherosclerotic heart disease is a lifelong process that is triggered by lipid retention in the arterial wall[25,26]. It is the underlying cause of coronary heart disease, which is still the leading

cause of death worldwide, despite decreased mortality rates in high-income regions since 1980[27]. **Figure 5** outlines the onset of atherosclerosis in the arterial wall. The disease is caused by high-lipid diets, as excessive lipid uptake results in elevated lipoprotein levels in the blood, especially lipid rich low-density lipoprotein (LDL). If this excessive lipid uptake is persistent, endothelial cells absorb (or take up) lipoproteins from the blood stream and store them inside the underlying tunica intima. Biochemical transformation of the lipoproteins renders the particles proinflammatory, which in turn attracts leukocytes. In particular, monocytes "sniff" this inflammatory signal, adhere to the endothelial vascular layer, and subsequently transmigrate into the tunica intima, where they differentiate to macrophages and start ingesting the proinflammatory lipoproteins[28,29]. Accumulation of absorbed lipid-rich particles within macrophages results in considerable lipid droplet development in their cytosol, leading to a characteristic "foamy" appearance, hence the name foam cells[30]. As more lipoproteins are retained, the vicious cycle of monocyte attraction, macrophage differentiation, and foam cell formation continues. With the onset of the disease, an atherosclerotic plaque develops, including a pool of necrotic cells and extracellular lipids in its core and a mix of cellular entities in the outer regions. This plaque causes physical narrowing of the artery, restricting blood flow to downstream organs. In case of a plaque rupture, subsequent thrombus formation can lead to even more severe arterial blocking[31]. To counteract plaque rupture, smooth muscle cells migrating from the tunica media to the atherosclerotic regions synthesize collagen to build up a fibrotic cap around the plaque for stabilization. This leads to substantial remodeling of the surrounding extracellular matrix, with tissue elastic modulus ranging from 5.5 kPa in lipid rich regions to over 10.4 kPa in cellular fibrotic regions, to 59.4 kPa in the fibrous cap[32] (see **Figure** 5). Notably, the fibrous cap shows strong heterogeneity in elastic measurements locally rising to levels around 250 kPa[32].

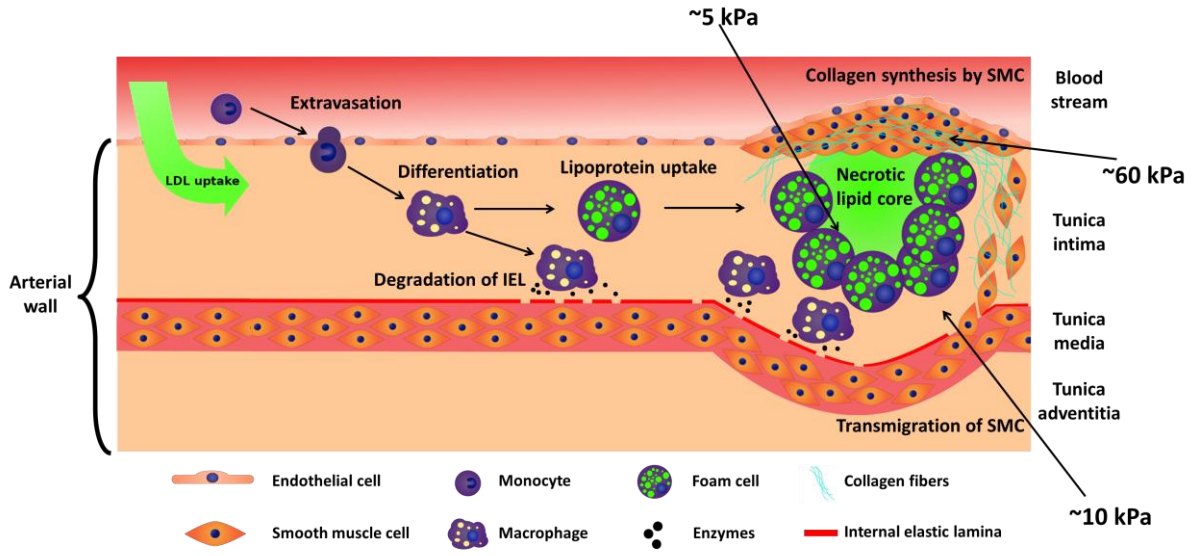

Figure 5 Onset of Atherosclerosis

Low density lipoprotein (LDL) from the blood stream is transported into endothelial cells and retained in the tunica intima. Enzymatic activity forms proinflammatory LDL particles, attracting monocytes from the blood stream that migrate into the arterial wall, differentiate to macrophages, and start clearing the LDL from the tissue. Accumulation of lipids in the macrophage cytosol transforms macrophages into foam cells. Persistent high lipid diets lead to atherosclerotic plaque formation along with a remodeling processes around the plaque resulting the stiffness regimes indicated with black arrows (stiffness values from[32]).

Interestingly, macrophages have several routes for lipid uptake and it is unclear about the uptake efficiency and overall impact on the respective receptors in atherosclerosis[33]. Receptors mostly associated with lipoprotein uptake in macrophages include the scavenger receptor A (SR-A) class[34–36], CD36[37–39], the LDL receptor (LDLR)[40,41], and the LDL receptor-related protein (LRP)[42,43]. This multitude of entry pathways account for the various forms of modified LDL uptake. The most commonly used LDLs in studies are native LDL, oxidized LDL (oxLDL), acetylated LDL (acLDL), and aggregated LDL (agLDL)[44–46]. There is, however, no evidence of LDL acetylation in the body[44]. Additionally, LDLR (the receptor for native LDL) is regulated via a negative feedback loop that prevents excessive lipid accumulation[44]. Therefore, foam cell formation is believed to depend on oxLDL and agLDL[44]. agLDL is formed in the subendothelial space via protease and esterase activity[47]. The proteolytic activity is believed to result in exposure of lipophilic areas on the surface of the lipoprotein and aggregation would therefore be energetically favorable for modified LDL in an aqueous environment[48]. oxLDL is thought to be produced by reactive oxygen species, that are more abundant in atherogenic conditions (e.g. hypercholesterolemia, elevated blood pressure)[49]. The influence of substrate stiffness on intracellular lipid accumulation in THP-1 derived macrophages is analyzed in chapter 4.

1.4 Light microscopy for cell culture observations

Most cellular examinations in this work were carried out using microscopy. Therefore, in this chapter, I want to review the process of image generation based on the microscopic techniques used in my studies.

1.4.1 Physics of light microscopy

Microscopy is traditionally performed using visible light to probe light-matter interactions (LMI) within an object of interest, thereby determining its structure. Light is an electromagnetic field that exhibits a sinusoidally oscillating electric and magnetic field, which are mutually perpendicular towards each other and the direction of propagation. The distance covered by a wave during one full field oscillation denotes the wavelength (see **Figure 6**).

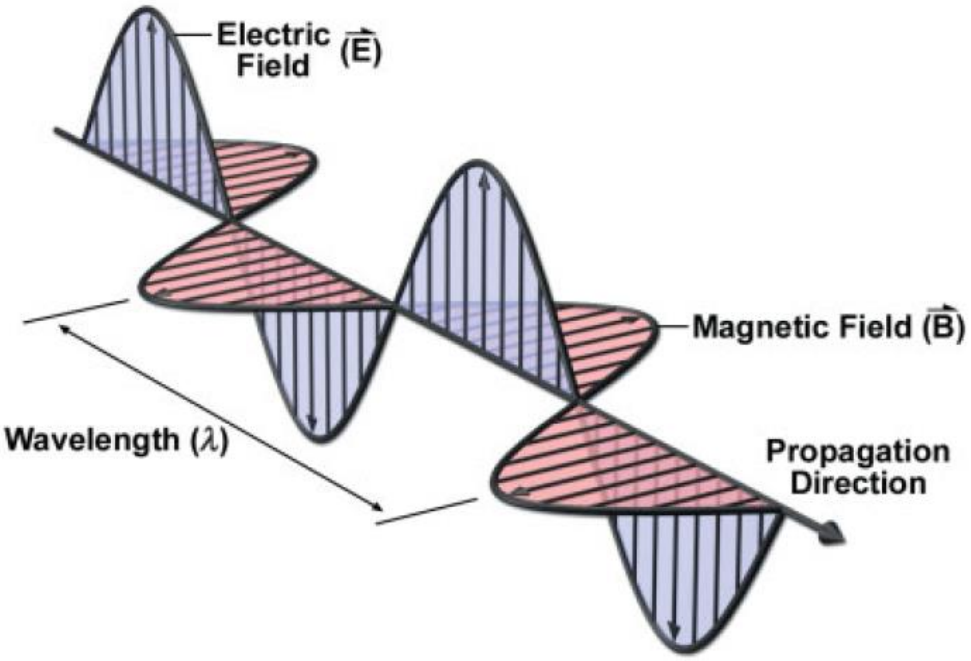

Figure 6 Light as an electromagnetic wave (image from[50])
The electromagnetic wave consists of the mutually oscillating electric and magnetic fields. The distance traveled during one oscillation is described by the wavelength.

Light exhibits features of both waves (such as diffraction and interference) and particles (e.g. in the photoelectric effect), the so-called wave-particle duality. This duality is of remarkable importance regarding energy forms. While energy of light is proportional to the amplitude of its oscillating fields, the photon energy (i.e. in particle mode) is proportional to the reciprocal of the wavelength and the speed of light. Therefore, two features of the electromagnetic wave are of major importance: The wavelength and the amplitude of the wave.

First, we will focus on the wavelength as it provides information about the photon energy. The photon energy E in a light field can be calculated based on the speed of light c, the Planck's constant h, and the wavelength λ.

$$E = \frac{h \cdot c}{\lambda} \qquad \textbf{1.1}$$

Frequency v, which denotes the number of oscillation cycles within an electromagnetic wave travelling a distance of 1 cm, is equal to the speed of light divided by the wavelength:

$$v = \frac{c}{\lambda} \qquad \textbf{1.2}$$

Therefore, photon energy is directly proportional to its frequency and inversely proportional to its wavelength:

$$E = h \cdot v = \frac{h \cdot c}{\lambda} \qquad \textbf{1.3}$$

With E being the photon energy [ergs] and h being the Planck's constant [$6.62 \cdot 10^{-27}$ erg-seconds], v being the frequency of light [cm^{-1}], c being the speed of light [$3 \cdot 10^{10}$cm/s], and λ being the wavelength [cm][50].

Photon energy (or wavelength) is of particular interest in image generation, as all sensors, including the human eye have different sensitivities for various photon energies. Physically, blue light in the range of 400 – 460 nm is more energetic than red light in the range of 650 – 800 nm. Beyond the detection limit, photonic energy transfer LMIs in samples can be detected by observing wavelengths other than those used for excitation. LMI induced shifts in wavelength yield qualitative information about the observed system. So-called "red shifts" (or Stokes shifts) result in emissions of longer wavelengths (less energy photons) than what was used for excitation, denoting an energy loss in the system. In contrast "blue shifts" (or anti-Stokes shift) come from the transition from longer excitation wavelengths to shorter emission wavelengths, denoting energy gains. Energy gains of photons during LMI are extremely rare and need specialized laser setups to be exploited for scientific analyses (e.g. in nonlinear microscopy), while red shifts are commonly used in conventional microscopy and spectroscopy.

The second outstanding feature of electromagnetic waves, is the amplitude of the field, which is a quantitative measure indicating the brightness of light. Nearly all photoreceptors, such as photoreceptive cells in the retina, react proportionally to light *power* instead of *amplitude*. Power is loosely defined as being proportional to the square of the amplitude (or brightness), and it denotes the energy – or photon – flux, the rate of flow of light energy per unit time across a detector surface. Light intensity is further defined as the power per unit area; different light intensities allow the eye to discriminate between objects by exerting contrast:

$$C = {}^{\Delta I}/_{I_{BG}} \qquad \textbf{1.4}$$

With ΔI being the difference in light intensity between object and background and I_{BG} being the intensity of the background.

Different light intensities and wavelengths in microscopy arise from various forms of LMI:

- Transmission
- Reflection
- Diffraction
- Absorption

While contrast generation in conventional light microscopy (such as brightfield and phase contrast microscopes) is mainly based on scattering and transmission, fluorescence microscopes are built on the principle of light conversion in the sample to separate excitation and emission.

1.4.2 Spatial resolution

Spatial resolution of a microscope not only depends on the wavelength used, but also on the objective applied. The resolution achievable with a given objective is determined by the angle by which it captures diffracted rays from the specimen and the refractive index of the

immersion medium used[50]. The contribution of both factors is summarized as numerical aperture (NA):

$$NA = n \cdot \sin(\theta) \quad \textbf{1.5}$$

Where n is the refractive index of the immersion medium and θ is the maximum half-angle of the cone of light accepted by the objective. Influences by immersion medium and light angle are shown in **Figure 7**.

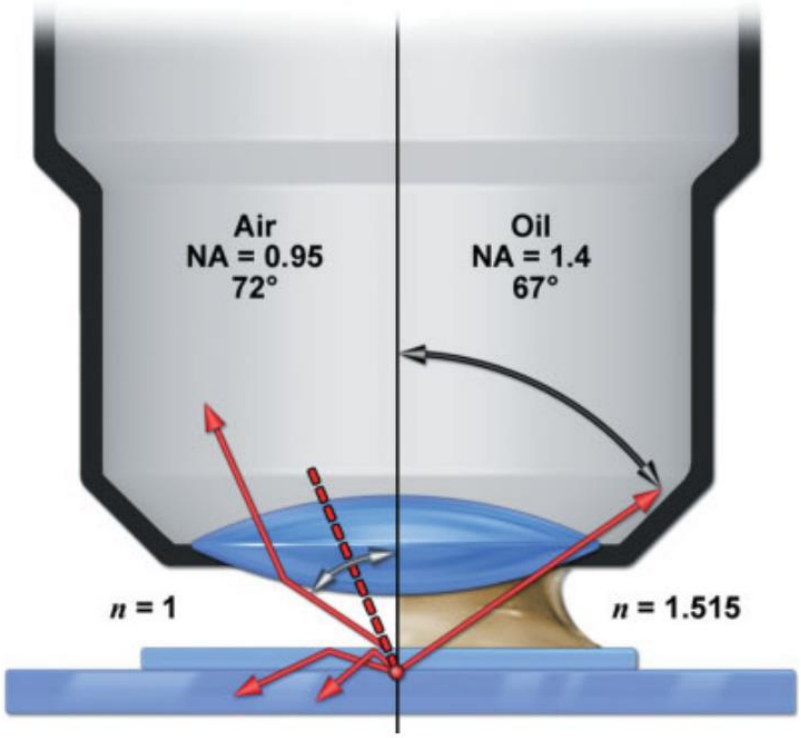

Figure 7 Numerical aperture influenced by light angle and immersion medium (from [50])
Left: NA is limited in dry objectives, as rays exceeding the critical angle (critical angle marked as red dotted line) are subject to total internal reflection. The change of refractive index from glass to air extends the acceptance angle to 72°. Right: Using oil as immersion medium with a refractive index similar to glass prevents total internal reflection (no rays lost) and results in an acceptance angle of 67°. The higher NA of the oil immersion objective results from higher refractive index of the immersion medium (1.515 of oil versus 1 of air) that is a multiplication factor in NA calculation.

Lastly, as spatial resolution is also dependent on the wavelength used for microscopy, the resolving power d of an objective is given by:

$$d = \frac{0.61\lambda}{NA} \quad \textbf{1.6}$$

Where d is the minimum resolved distance in µm, λ is the applied wavelength in µm, and NA is the numerical aperture as calculated above[50].

1.4.3 Brightfield microscopy

Brightfield microscopy is undoubtedly the least complex form of microscopy: The sample is homogeneously illuminated from one side and transmitted light is collected with an objective on the opposite side. Magnification by a lens system in the objective produces an image with contrast originating mostly from the scattering of light by dense regions of the sample. Since almost no sample preparation is required, live cell imaging is possible, even for several days, in combination with appropriate environmental conditioning devices (e.g. temperature and humidity). However, as compartments within cells show only limited scattering, contrast is often quite low. Staining cellular structures can enhance contrast via absorption of certain wavelengths, but it is often accompanied by a need to fix the cells prior to image acquisition, thereby destroying the possibility of live-cell imaging.

1.4.4 Phase contrast microscopy

In the early 1930's, Dutch physicist Frits Zernike discovered a phenomenon called phase contrast[5], in which he translated differences in phase, which are invisible to the human eye, into differences in amplitude. Contrast added in this way, led to a substantial advancement of light microscopic techniques in the 1940's. The underlying principle is the retardation of light in materials with higher refractive indices than their surroundings. For instance, the lipid membrane of a cell will have a higher refractive index than the aqueous medium surrounding it, i.e. light will travel faster in the aqueous medium, than in the cell. This difference in velocity results in a phase shift.

As **Figure 8a** shows, light passing through a phase object results in three waves: The surrounding wave (S-wave) that does not interact with the object, the diffracted wave (D-wave) that shows a reduced amplitude and a phase shift depending on the refractive index and thickness of the objective (in cellular dimensions typically $\lambda/4$), and a particle wave (P-wave) that is the wave generated from interference of S- and D-wave. However, as light interaction with phase objects is scarce and the phase shift between S- and D-wave insufficient for complete destructive interference, the effect needs to be amplified. This is achieved by decoupling surrounding waves from diffracted waves in phase contrast microscopy (**Figure 8b**). A hollow cone of illumination light is formed via an annular aperture in the condenser. After passing through the specimen, the S-waves are guided through an etched ring inside a phase plate, while D-waves are diffracted from the specimen and travel through the center of the phase plate. As the center of the phase plate is thicker than the etched ring surrounding it, D-waves are retarded relative to the S-waves, thereby extending the relative phase shift to $\lambda/2$. In addition, the semitransparent ring around the center reduces the amplitude of S-waves by 70 – 75%[50]. The resulting S- and D-waves now interfere at the detector (**Figure 8c**), and the effect on the generated P-wave is amplified due to comparable amplitudes of both waves.

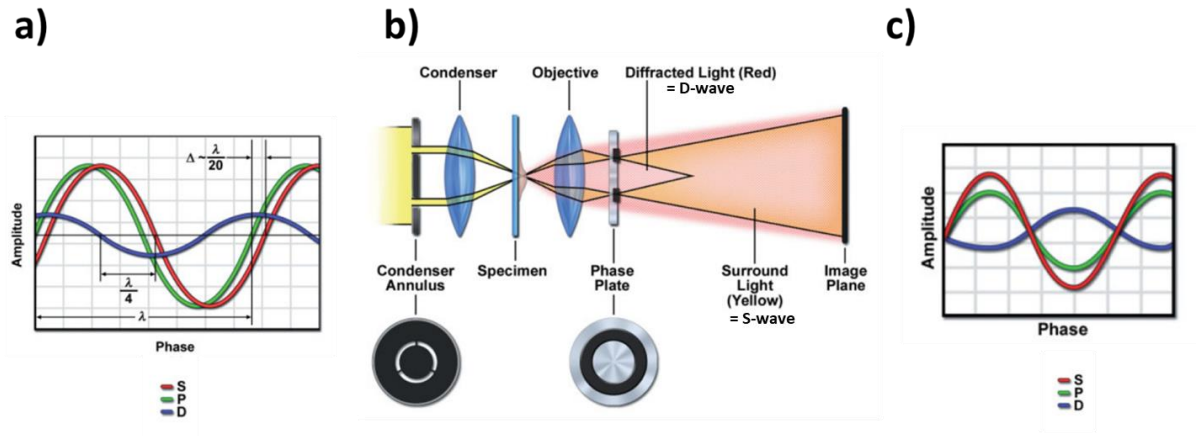

Figure 8 Principle of phase contrast and design of a phase contrast microscope (adapted from [50])

a) Phase relations of light transiting through phase objects: S-wave (red) does not interact and phase remains unchanged, D-wave (blue) generated by diffraction in phase object exhibits a ~ λ/4 phase shift and decreased amplitude, P-wave (green) generated from interference of S- and D-wave shows only minor differences to S-wave. b) phase contrast microscope design: an annular aperture generates a hollow cone of light to illuminate the sample. While light interacting with the object is diffracted from the light path, non-interacting waves are guided through a semitransparent etched ring in a phase plate. The phase plate has two functions: (1) It reduces the path length of the S waves through high refractive index medium relative to D-waves travelling through thicker regions in the center of the phase plate, thereby amplifying the phase shift between S- and D-wave and (2) it reduces the amplitude of S-waves to approx. 25 % its original value. c) Resulting phase and amplitude relations after phase contrast modification: The overall phase shift of ~ λ/2 to the D-wave results in destructive interference, the reduced amplitude of the S-waves amplifies this effect.

1.4.5 Fluorescence microscopy

Fluorescence is a form of luminescence, the process of light emission from the relaxation process of an electronically excited molecule. Electronic excitation can be explained by Jablonski energy diagrams (**Figure 9**) in which electronic states are shown as either ground state (S_0), or excited states (S_1, S_2) with corresponding vibrational states. Upon absorption of photons, electrons can be excited from the ground state to higher electronic states. As a precondition, the wavelength of exciting light needs to match the energy level needed to overcome the energy gap from ground to excited state. After excitation, the electron can either relax to the ground state immediately or lose a part of its energy via internal conversion. When electrons relax from an excited state back to the ground state, they emit electromagnetic radiation. The loss of energy in internal conversion is typically non-radiative, and therefore the relaxation of the electron to the electronic ground state results in an emission of lower energy (longer wavelength) or Stokes shifted light, compared to the excitation light.

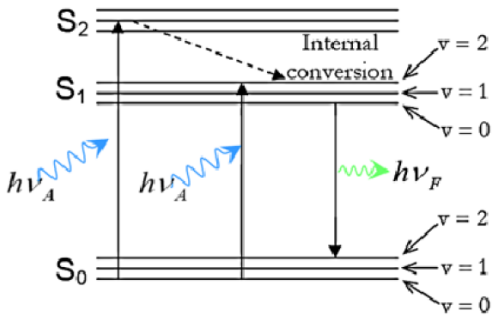

Figure 9 Jablonski diagram for electronic excitation (adapted from[51])

Fluorescence depends on an electron excitation. Excitation photons ($h\nu_A$, blue) excite electrons from ground state (S_0) to higher energetic states (S_1 and S_2) depending on the energy (the wavelength) of the incoming light. Internal conversion leads to radiation-free energy loss, while a drop back from excited to ground state is connected to photon emission ($h\nu_F$, green), which in red-shifted light emission.

In fluorescence microscopy, fluorophores in the specimen are excited using a specific wavelength band via a lamp or laser source. As excitation and emission wavelengths are different from each other, filters can be used to block the excitation light prior to the detector. In this way, excitation and emission light is separated and only emission light is collected. The signal intensity arriving at the detector therefore corresponds to the fluorescent light emitted by the fluorophores in the specimen.

Currently, literally thousands of fluorescent dyes for a broad range of organelles and cellular compartments as well as different wavelength ranges exist. Below in Table 1 are four dyes used in this work, just to name a few:

Table 1 Examples of fluorescent probes used in this thesis

Name	**Subcellular localization**	**Excitation maximum**	**Emission maximum**	**Supplier (catalog number)**
DAPI	Nucleus	350 nm	470 nm	Thermo Fisher (D1306)
DRAQ5	Nucleus	647 nm	681 nm	Thermo Fisher (62251)
CellMask Orange	Cytoplasm	554 nm	567 nm	Thermo Fisher (C10045)
BODIPY 493/503	Lipid droplets	503 nm	512 nm	Thermo Fisher (D3922)

Additionally, the ability to conjugate fluorophores to highly specific antibodies has enabled researchers to detect virtually any protein or organelle within a biological sample. Finally, the advent of fluorescent proteins like GFP, that can be genetically fused to proteins of interest allow live-cell observations without any sample preparation.

1.4.6 Confocal microscopy

Confocal microscopy is an imaging technique intended to reduce out-of-focus blur by physically blocking out-of-focus light; a side benefit of this process is also three-dimensional

(3D) resolution enhancement. In widefield fluorescence microscopy the entire optical field-of-view in 3D is illuminated and the emitted fluorescent light from the entire 3D excitation volume is collected with a detector, which includes in-focus and out-of-focus light. In confocal microscopy, point illumination is used and the emitted fluorescence is then spatially filtered by a pinhole such that only light from precise, in-focus axial locations in the specimen are collected (see **Figure 10**). Using a motorized stage or motorized mirrors, one can produce 3D volume representations of the imaged sample by scanning several X-Y-planes in varying z-depths.

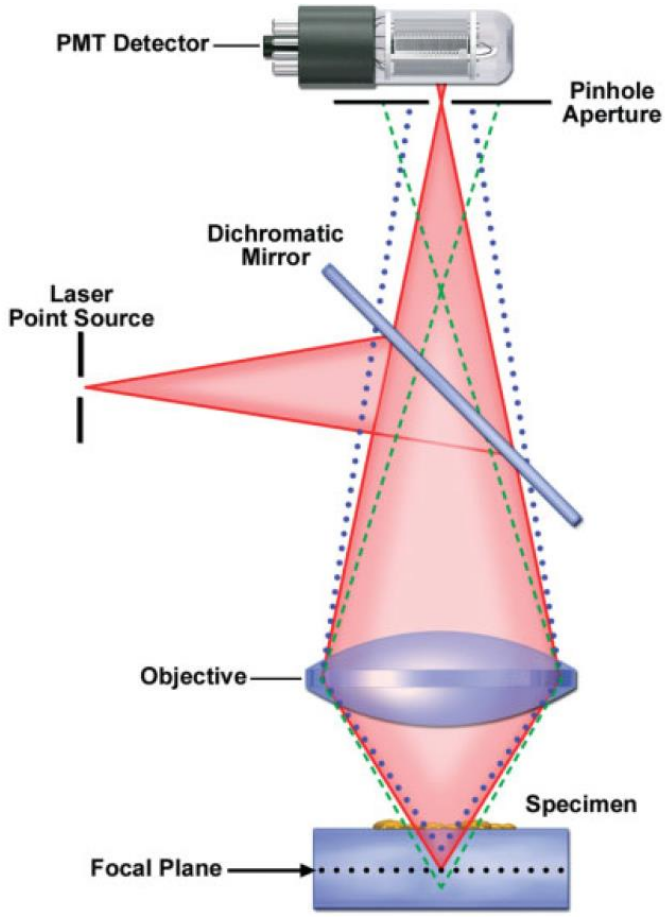

Figure 10 Design of a confocal microscope (image from[50])

A laser beam is focused onto a focal plane inside a specimen (indicated with dotted black line) for excitation. Fluorescent emission of light must pass through a pinhole aperture in front of the detector in the detection path. Note that light emitted from the focal plane (red) passes through the pinhole completely, while out-of-focus light from above (blue) and below (green) the focal plane is blocked.

Reductions in pinhole size lead to better resolutions but also decrease signal intensity as more light is filtered out. Z-step sizes must therefore be chosen carefully, as overlapping image planes can falsify volume detections in downstream image processing (e.g. double detection of features such as overlaying lipid droplets).

1.5 Image processing

After image acquisition, the raw data produced exhibits several obstacles in the form of background noise (e.g. through uneven illumination), touching objects, cellular debris, etc., that prevent quantitative image analysis. Image processing, in the context of this work, is

aimed at extracting quantitative geometric features of detected objects, and it is imperative that appropriate measures are taken to overcome the obstacles listed above to locate the objects of interest within the image with high precision. To generate meaningful quantitative statements from images, features of displayed objects must be converted into machine-readable data. The creation of hard-coded software solutions for batch image processing is almost always the ultimate goal and can be extremely laborious, as features for every object of interest must be identified by the programmer and transformed into algorithms that recognize these object classes (e.g. here: cells) automatically. An example of such an algorithm for cell detection after fluorescent nucleus staining can be found in Chapter 3. Outlining the basic steps of this algorithm shows the processing actions that hard-coded image processing algorithms typically include: Background reduction is achieved by subtracting a blurred copy of the original image, cell outlines are detected by low-value thresholding the fluorescence signal and touching cells are split by watershedding. Lastly cell debris is ignored by inserting a size and signal intensity filter. As Chapter 3 covers conventional microscopy image processing in detail, I will focus on the application of computer vision in image processing in this section.

1.5.1 Machine learning assisted image analysis

Machine learning is a sub-field of artificial intelligence, that deals with the ability of computer algorithms to make decisions or predictions for previously unknown input data. For instance, such algorithms decide which emails are regarded as spam[52], which items are proposed to the customer on shopping websites[53], or which advertisement users see in online social networks[54]. The decision-making process in this software is not handcrafted by computer scientists, but instead **"learned" automatically from data** and adapted accordingly for individual users. The individual adaptation is the reason why e.g. online advertisements after recent searches for motorbikes differ from online advertisements after recent searches for diagnostic antibodies. The decision-making ability arises from *feature-extraction* performed by the algorithm on training datasets. The extracted features are in turn used to categorize, predict, or classify *new* input data. In practice, datasets of labeled emails can be used to train a classification algorithm, that extracts and learns word combinations (i.e. *features* in the message) typically used in spam emails. Consequently, the trained classifier can be used to characterize previously unseen emails.[52]

After feature extraction from input data, machine learning algorithms need to classify the data accordingly. One of the most common mathematical models for classification are support vector machines (SVM). SVMs assume instances (i.e. objects within the data; e.g. emails to classify) as datapoints in n-dimensional systems, where the number of dimensions n is given by the number of detected features (e.g. number of words indicating spam vs. words indicating non-spam mails). To separate groups of datapoints in this system, an (n-1)-dimensional plane (SVM Hyperplane) is computed with support vectors. The SVM Hyperplane and the respective support vectors are calculated to span the largest distance (margin width) between the two separated datapoint groups (see **Figure 11**).

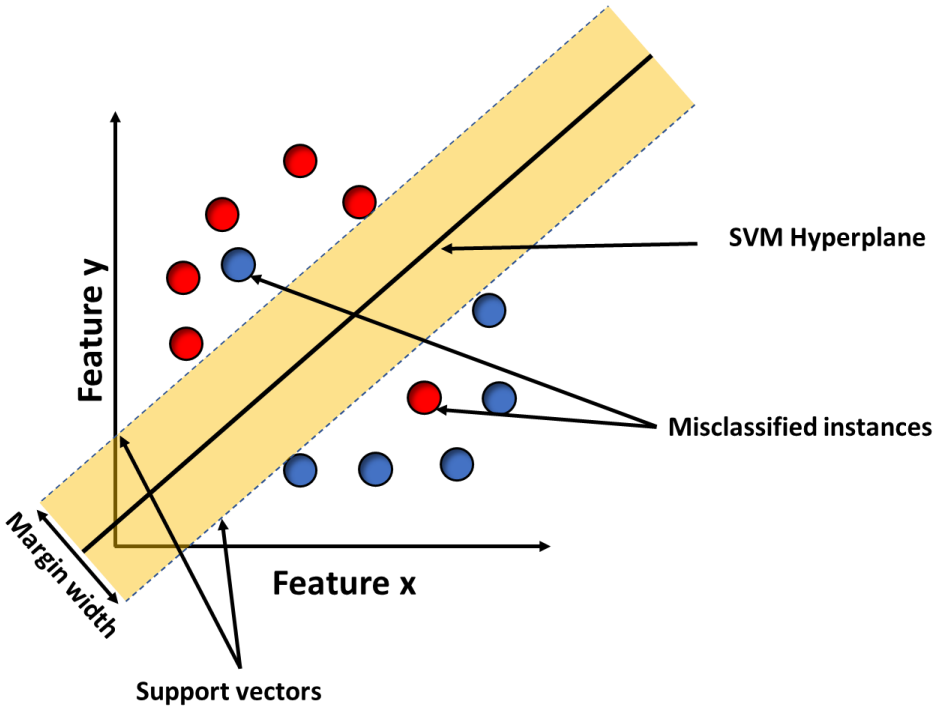

Figure 11 Concept of support vector machines in 2D. (adapted from[55])
Two selected features span a coordinate system and data objects are inserted as datapoints according to the magnitude of the features adopted (red = group 1, blue = group 2). A support vector machine (SVM) hyperplane and two corresponding support vectors are computed to form a maximum margin width between the two support vectors. The required maximum margin width results in a maximum distance between the two separated groups. As shown in the graph, misclassifications can occur (red datapoint in blue group and blue datapoint in red group). Optimally, features are selected that minimize the occurrence of misclassifications.

A machine learning algorithm seeks to find features that allow for highly specific identification of the classes it is trained on. If the classification algorithm is trained on identifying multiple classes, support vector machines will plot the data in multidimensional graphs.

However, feature detection in text or in other "clean" data (such as numerical values) is far simpler than feature detection in images. As text and numerical values are machine-readable, no substantial data preparation is required. Unfortunately, images are raw data and hence, need to be prepared for the algorithm to recognize patterns within the data. An additional procedure is necessary in addition to machine learning-based classifiers, that produces meaningful machine-readable data from images. Convolutional neural networks (CNN, more information in section 1.5.3), which extract image features using **filters generated from provided data itself**, can overcome this bottleneck. This not only drastically amplifies the precision of image classification and segmentation algorithms, but also facilitates the development process, as algorithms can learn features from provided datasets, independent from the programmer. One main accomplishment of this thesis was the training of a machine learning-assisted algorithm for cellular image processing. In this work, I applied the concept of supervised learning, i.e. the training of an algorithm using labeled data (e.g. class labels such as "cats", "dogs", or "cars" on images) as opposed to unsupervised learning, which is performed with unlabeled data. To generate an appropriate dataset for supervised learning, two components had to be provided: Data – in this case microscopy images - and annotations for objects within these images. Annotations can be "global" labels (one label for each image, "local" labels via bounding boxes (frames around objects within the image) or segmentation

masks (selection of the object outlines in the image). Class labels and segmentation masks are also called “ground truth”, since they specify object outlines and class labels with human accuracy. The remainder of this chapter gives an overview of convolutional neural networks, algorithm training, and computer vision developments. Finally, an introduction into the evaluation of image segmentation algorithms is given and the role of datasets is reviewed.

1.5.2 Image convolution

Digital images are, strictly speaking, nothing more than a grid of numbers. The numerical values making up an image can be transformed in order to emphasize certain structures within the image. Highlighting numerical values according to their surrounding can be achieved by a process called image convolution. Edge detection is a prominent example for image convolution: Numerical values forming edges in the image are highlighted, while pixel values in areas without edges are set to zero.

Figure 12 Image convolution for edge detection
Left: Input image (Lena, ImageJ sample photo); Right: Output after convolution with an edge detection filter. Edge detection highlights edge lines and sets pixel values in edge-free areas to zero.

Image convolution is the process of passing a convolution matrix (also called filter or kernel) across an image, forming a new output image. The pixel values in the new output image correspond to the dot product formed from overlapping values of the filter matrix and input image (see **Figure 13**).

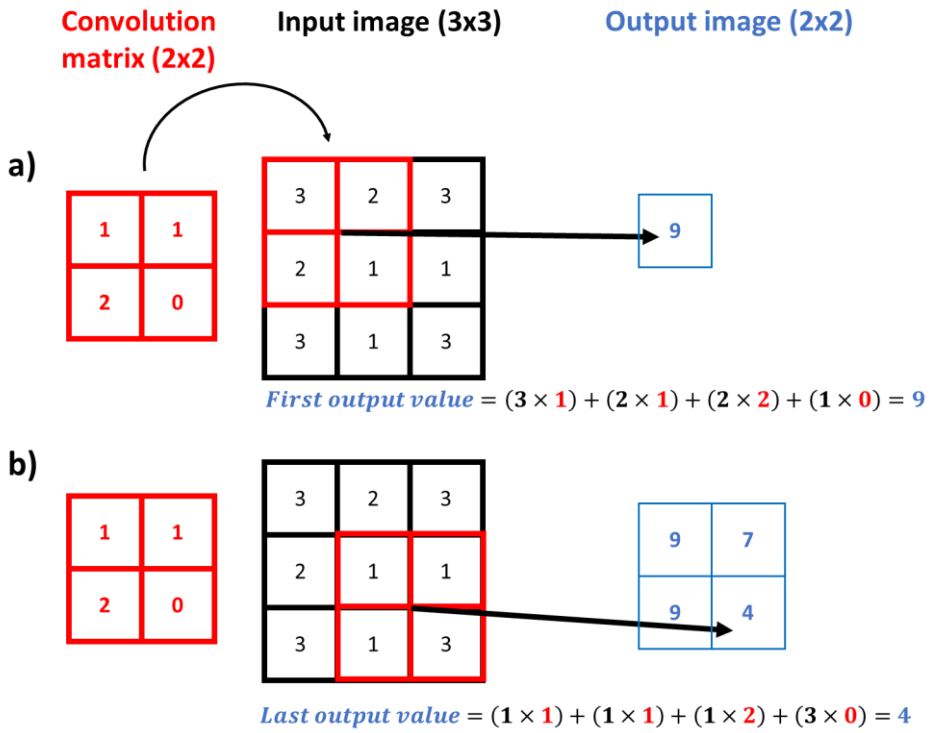

Figure 13 Convolution of an image using a convolution matrix

A filter matrix (red) is placed on an input image (black), forming the dot product with underlying pixels. The value of the dot product is assigned to a newly formed (blue) pixel (a). Passing the filter incrementally over the entire image, forms a new output image with pixel values generated from the image convolution with the filter (Last step shown in b). The output image (blue) is reduced in length and width according to the filter dimensions and ending conditions. Here: A 2x2 pixel convolution matrix can be shifted once in length and width on a 3x3 pixel input image, which results in a 2x2 pixel output image. Solutions to the size reduction include padding, which adds extra pixels with specific values to the input image or mirroring outer edge pixels. Padding artificially extends the input image and hence counteracts the loss in size during convolution.

For machine learning-assisted image processing it can be beneficial to reduce the resolution of images. The reduction can be achieved by down-sampling (also called subsampling), a process that derives a single value from several pixel values. The most prominent representative of a down-sampling mechanism is max-pooling. A filter matrix is passed over an image and selects the highest value captured in the filter frame as a value for the output image. Choosing bigger steps (strides) that are used to shift the filter over the image further decreases the image size. Selecting a 2x2 pixel max-pooling filter together with a 2-pixel stride, results in an output image that is reduced by 50 % in each dimension (see **Figure 14**).

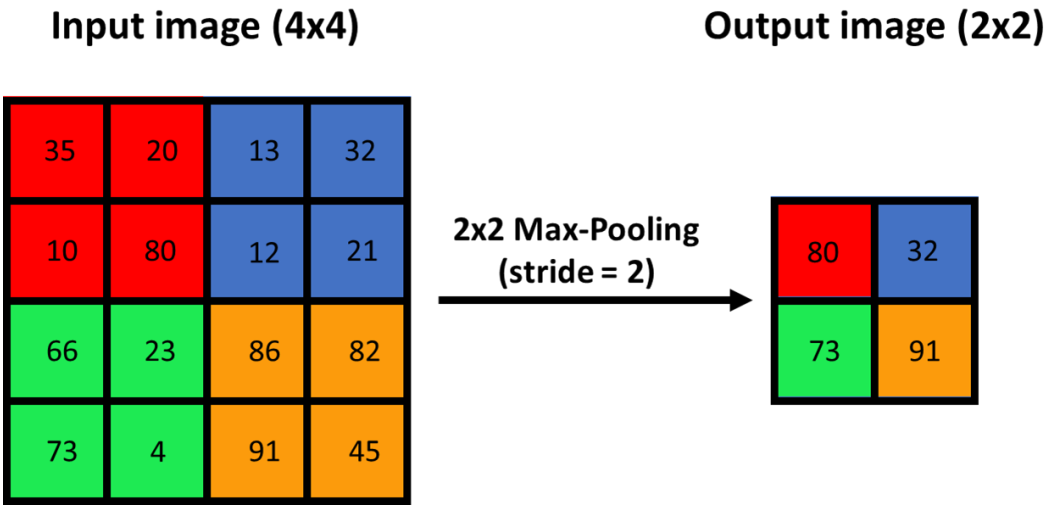

Figure 14 Concept of Max-Pooling

A filter selects only maximum values in the area covered by the filter-frame. The selected value is subsequently assigned to a pixel in the output image. The settings pictured here (4x4 input image, 2x2 max-pooling filter, stride of 2) result in an output image that is reduced in pixel-size by 50 % in each dimension.

As described in this section, filter matrices can be designed to highlight certain features within the image and down-sample image resolution. The next chapter introduces the importance of filter matrices in preparing images for classification and segmentation.

1.5.3 Convolutional neural networks

This section introduces the concept of convolutional neural networks for image classification and highlights historic achievements in improving this method. CNNs are used to process data in the form of multiple arrays[56]. One-dimensional multiple arrays can be sequences such as DNA or protein sequences. 2D multiple arrays would be images and lastly, 3D multiple arrays could be videos that add time as an additional dimension. The founding stone for CNNs was laid in the 1960's by Hubel and Wiesel who discovered that cats' visual cortexes contained at least two types of cells with hierarchical organization: simple cells detecting edges and orientations, and complex cells that respond to movement[57]. Although this was a biological finding it showed the complexity in image reception, as the output of one cell type (simple cells) was the input for the next cell (complex cells).

The hierarchical structure in neural processing later inspired computer scientists to adopt a similar structure in algorithms, where the output of one computational step (the pendant to a neuron) was the input for the next. Connecting several artificial neurons creates an artificial neural network. **Figure 15** shows the scheme of an artificial neural network with nodes representing individual computational processing steps that are organized in layers. Users of algorithms based on an artificial neural network architecture will typically come into contact with input and the resulting output layers. For instance, in email classification input would be a message, while output would be a class label like "spam" or "regular text".

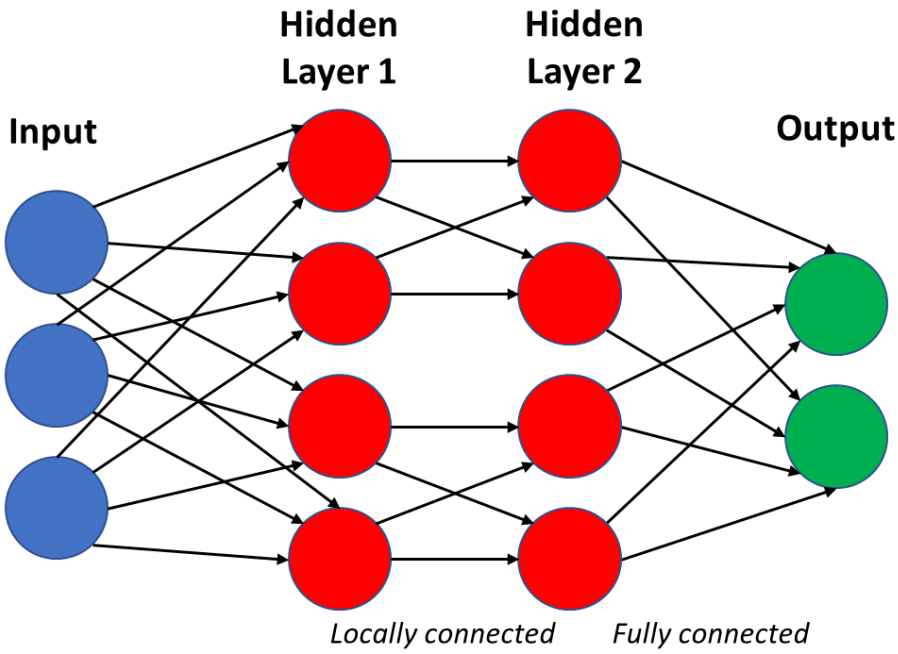

Figure 15 Scheme of an artificial neural network

Artificial neural networks connect computational processing steps (nodes). Outputs of one layer serve as inputs for the next layer (arrow-connections). Layers in which individual nodes are connected to a *portion* of the nodes in the previous layer are called "locally connected". Layers in which individual nodes are connected to *all* nodes of the previous layer are called "fully connected".

In between the input and output layer, hidden layers are inserted that perform various functions on the data that is processed by the artificial neural network[58]. During data transfer from a previous node to the next (arrows in **Figure 15**), parameters - so-called "weights" - adjust the impact of the individual input on the next node[58] (e.g. total neglection of the input value by multiplying it with zero). Weights are essential for appropriate data transformation and their adjustment will be the topic of section 1.5.4. One can discriminate between *fully connected* layers, i.e. individual nodes in the layer receive inputs from all nodes of the previous layer, or *locally connected* layers, i.e. individual nodes in the layer are connected to **some but not all** nodes of the previous layer. Fully connected layers by far prevail in modern artificial neural networks as they allow for a simultaneous consideration of all parameters from the previous layer without restricting the "receptive field" (number of connections) of a node.

As the name suggests, CNNs are artificial neural networks that perform matrix convolutions. The possibly most important step in CNN development was made in 1998 by Yann LeCun, who built a neural network, applying multiple convolutional layers with a built-in self-training mechanism[59].

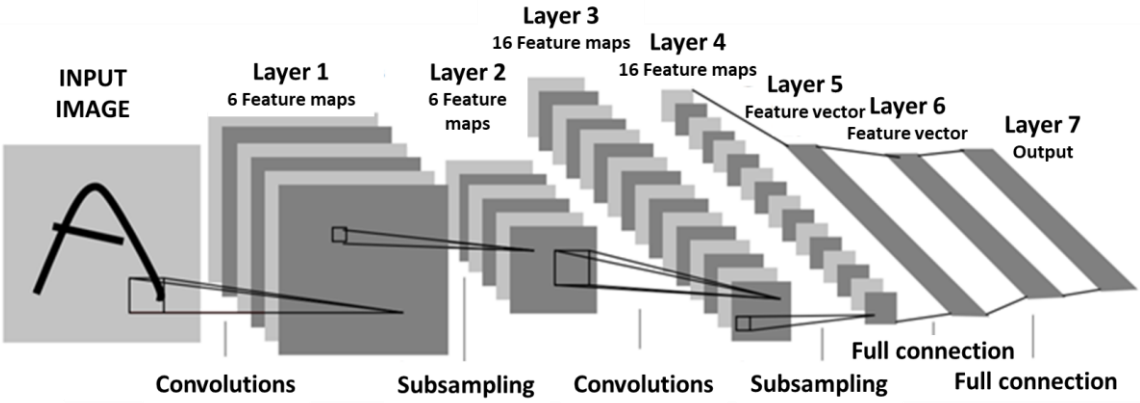

Figure 16 Convolutional neural network created by LeCun et al(adapted from [59])

The convolutional neural network consists of seven layers. An image with the letter "A" serves as input. The first four layers alternatingly perform convolutions and subsampling creating feature maps that highlights structures in the image. 16 small feature maps created in the 4th layer are miniature representations of features extracted from the original image. Layers five to seven are fully connected layers that derive numerical values from the multiple feature maps and compute an output. In this case the output is a class label, predicting the object detected within the image (In this example handwritten digits).

In the CNN created by LeCun *et al* (see **Figure 16**), four layers performed image convolutions (e.g. edge detection or color sorting) and subsampling, creating a multitude of low-resolution feature maps. The maps were used as an input to fully connected layers. Fully connected layers transformed the low-resolution feature maps into numerical value representations (a so-called feature-vector) of the features extracted in the convolution layers. In the output layer, a class label is computed using the numerical feature representations for classification. The implementation was extremely successful in recognizing hand-written digits, eventually being used for zip code reading in postal services. However, the algorithm could not be applied to higher resolution images, as it was limited by computing capacity, restricting the algorithm to fairly simple tasks.

It was not until 2012, when Alex Krizhevsky applied a CNN in a large-scale image recognition challenge[60] and proved the applicability of the method for high resolution images and multi-class recognition (1000 classes from every-day scenes, e.g. "person", "car", etc.). For training the classification-algorithm, Krizhevsky was building on the vast amounts of labeled image data, as well as the parallel computing power of graphic processing units (GPU). Since 2012 we have seen a tremendous use of CNNs not only for image recognition, but also object localization[61–63] and lastly segmentation[64] of object outlines within the image.

The revolutionary capability of CNNs is that the algorithm adjusts filters automatically by "learning" from a labeled training dataset. More information on the learning process is provided in Chapter 1.5.4. Although convolutional filters are learned individually based on the training data, the process usually leads to a hierarchical structure of convolutional layers that resembles the structure of simple and complex cells for visual processing in the brain. In essence, CNNs mostly start a feature detection process by extracting low-level features such as edges and then combines the detected structures to search for high-level features like shape motifs in later convolutional layers.

1.5.4 Learning process

As mentioned above, a CNN based algorithm needs to be trained to set its own weights, which are essentially the adjusted filter matrices for image convolution. However, to achieve appropriate filter adjustments, the algorithm needs a guiding process. This is started by providing exemplary weights (either starting from previously trained CNNs or initiated with random weights) and passing data (which might be images, speech, etc.) through the CNN, which is called a "forward pass" (see **Figure 17a** for an exemplary schematic forward pass). It is highly improbable that the classification will result in a successful prediction at the end of the first forward pass. Therefore, an objective function needs to determine correctness and, if incorrect, the distance of the prediction to the ground truth[56]. Depending on the result of the objective function, weights must be adjusted by tiny fractions for each image in a way that minimizes incorrect detections and maximizes the probability for the correct output[56]. To achieve this, gradients for each weight must be computed that decipher the contribution of the specific weight to the result of the objective function. **Figure 17b** shows the principle of backpropagation, which is basically applying the chain rule for derivatives.

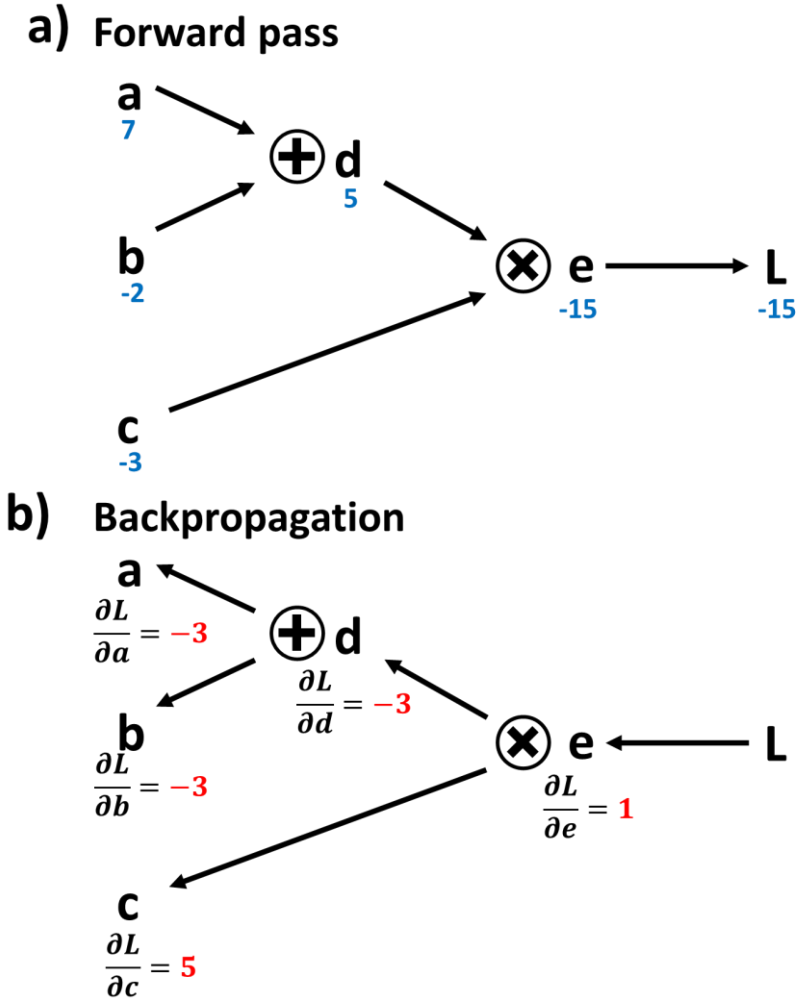

Figure 17 Principle of backpropagation

Weights a, b, c, d, and e have an influence on the result L. Feeding exemplary values into this process tree (blue) shows the process of a forward pass (a). Back propagation (b) is calculated in the opposite direction to decipher influences of all weights according to the chain rule for derivatives. To manipulate the result L, all weights can be changed in very small increments.

Gradients of the weights “a”, “b”, “c”, “d”, and “e” are computed with respect to their contribution on the result “L”. Thus, if the goal is to determine the difference in “L”, triggered by the change of weight “a”, one needs to multiply the effect of “d” on “L” with the effect of “a” on “d”:

$$\frac{\partial L}{\partial a} = \frac{\partial L}{\partial d} \cdot \frac{\partial d}{\partial a} = -3 \qquad \textbf{1.7}$$

In this way contributions of each weight in the network can be determined and values updated according to the results from the last forward pass. In the example depicted in **Figure 17**, an incremental change of +1 on weight “a” would decrease the value of “L” by 3. If the lowest possible value for “L” is to be achieved, an incremental change of +1 on weight “a” would be beneficial. Whether “L” should be high or low depends on the respective application. The incremental change of weights depends on a predefined **learning rate**. The learning rate is a numerical value that dictates the amount a weight is changed in each backpropagation. Although it is beneficial to start the training with high learning rates, lower learning rates are recommended in later fine-tuning when it is necessary to adjust for subtle changes in the data.

In the case of image classifiers, forward passes are performed with images and the weights correspond to the convolutional filter matrices. The “objective function” is a loss function that calculates the probabilistic difference from the *predicted class label* to the *provided ground truth class label*. Filter matrices are adjusted using the backpropagation mechanism. To build robust image classifiers based on CNNs, several forward passes of images have to be carried out with subsequent backpropagation and weight adjustments. A large number of images are needed for the algorithm to generate meaningful filter sets, based on feature variations depicted by the objects with the images. If only a small amount of data or highly homogeneous data is provided, the problem of overfitting arises, in which the filters are guided towards image features instead of object features. In such a case, classification would then be based on image specific illumination and shadowing instead of object shape. In scientific imaging modalities, limited and especially homogeneous data (e.g. one microscope, with one objective, and one illumination lamp configuration that is used to produce few images of a single cell line for training) can produce algorithms that are in turn restricted to the particular configuration that captured the dataset. In case of limited data availability, image augmentation like flips and rotations can be employed to combat overfitting.

1.5.5 Object localization

Image classification only assigns predicted class labels to an image with scores denoting the probability or confidence for the output. Therefore, it is a merely qualitative method that lacks crucial parts for quantitative image analysis. The next step in image analysis is object localization, which not only predicts class labels for input images, but also draws frames, so-called bounding boxes, around the predicted objects within the image. Good examples for object localization are the applications of the “regions with CNN features” (R-CNN) method[61–63]. These approaches first use a region proposal system, that identifies potential object containing areas within an image and subsequently classifies the extracted regions via a CNN and SVMs. Region proposal was first performed using an algorithm called “selective search”[65]

which groups similar regions in an image, thereby forming areas that are likely to belong together.

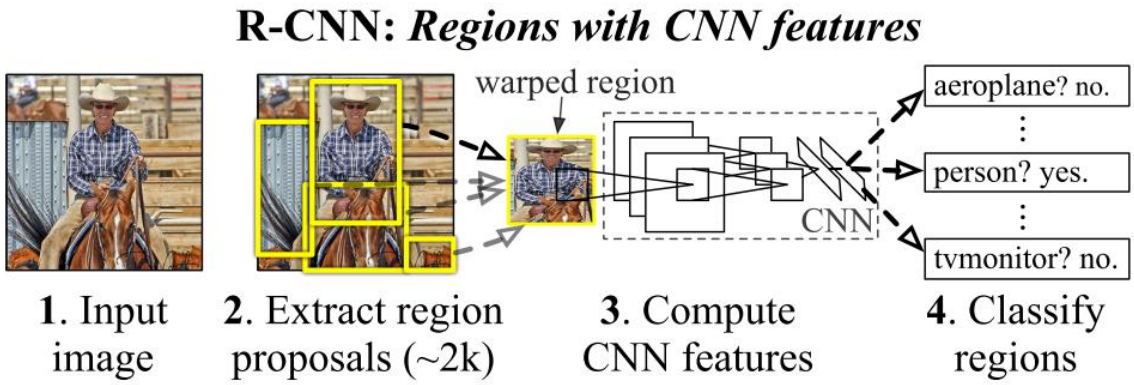

Figure 18 R-CNN process[61]

Input images are regionally scanned for possible objects. Region proposals (yellow frames) are extracted and passed into a convolutional neural network for feature extraction. The object within the frame is classified according to the feature vector using support vector machines.

However, this system is a multi-stage process that includes individual CNN training on several proposed regions of the image, SVM computation, and bounding-box regressor training. Computation is not shared during these stages, offering a potential for enhancement which is introduced with Fast R-CNN[62]. The advancement of Fast R-CNN mainly results from the combination of all stages from R-CNN to one single stage, in which an entire image, along with a set of region proposals, is used as input to a CNN. After passing convolutional and max pooling layers, a feature vector for each region proposal is extracted from the feature map produced and passed into fully connected layers that eventually produce classification probability and bounding box regression. The highly simultaneous architecture significantly speeds up the process, as entire images rather than individual image regions are convolved. Together with subsequent advancements in region proposal systems, using convolutional feature maps instead of raw image input, image detection can now be run at 5 frames per second, approaching real-time object detection[63].

1.5.6 Object segmentation

Object classification and detection give a rough estimate of object size at best but lack the true quantitative nature of image analysis. To properly quantify objects within images, algorithms need to accurately map object outlines. The process of appropriately classifying each image pixel to an object class is called segmentation. Segmentation masks, the outlines of segmented image areas, are by far more meaningful than bounding boxes, as object outlines allow for pose (e.g. cheering, walking, jumping) estimation, shape characterization, and area quantification relative to image size. Given the pixel-to-length calibration ratio (as is the case in microscopy), absolute number calculations, e.g. for object area, are possible.

In many algorithms, every-day scenery has been segmented by classifying pixels into classes without accounting for individual object detection (semantic segmentation). In this case, segmentation of groups often results in detection of a single instance (such as in the algorithm ENet in **Figure 19**).

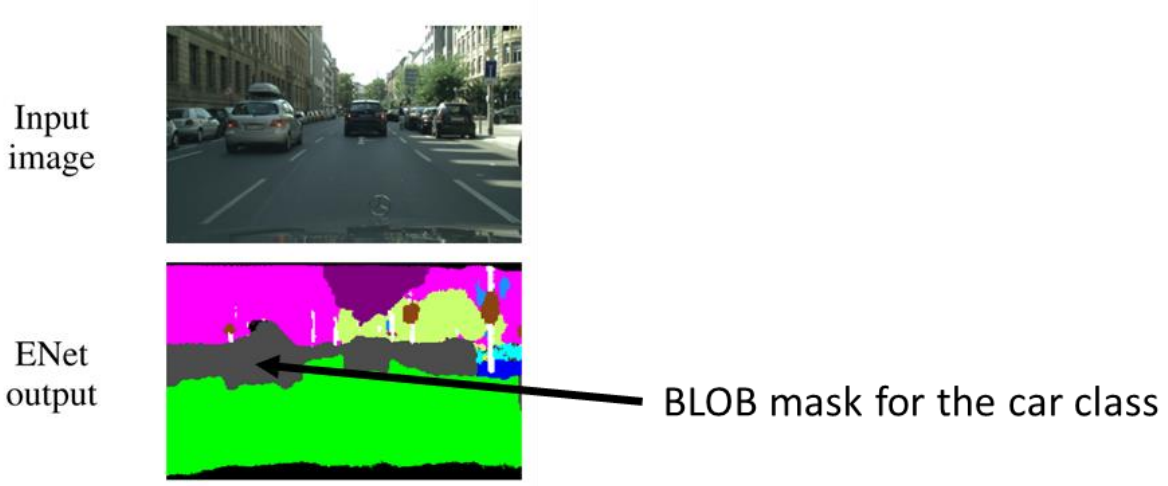

Figure 19 Output of semantic segmentation algorithm ENet[66]

Note detection of car class as one broad binary large object (BLOB). The concept of semantic segmentation lacks assignment of segmented outlines to *individual* objects within the image.

The combined detection of multiple objects in one single segmentation mask was prevented by applying *region proposals* to subdivide the image before the segmentation process. Region proposals "cropped" single objects within the image into a region of interest (RoI) frame. Subsequent segmentation of the single object within the predefined RoI resulted in segmentation of *individual* objects in an image (instance segmentation). Again, it was an R-CNN based system that showed impressive results. Since it added a mask branch to the R-CNN system it was called Mask R-CNN[64]. The mask branch consists of convolutional layers that preserved the spatial layout of the proposed region, while filtering the region of interest (ROI) for object masks (see **Figure 20**).

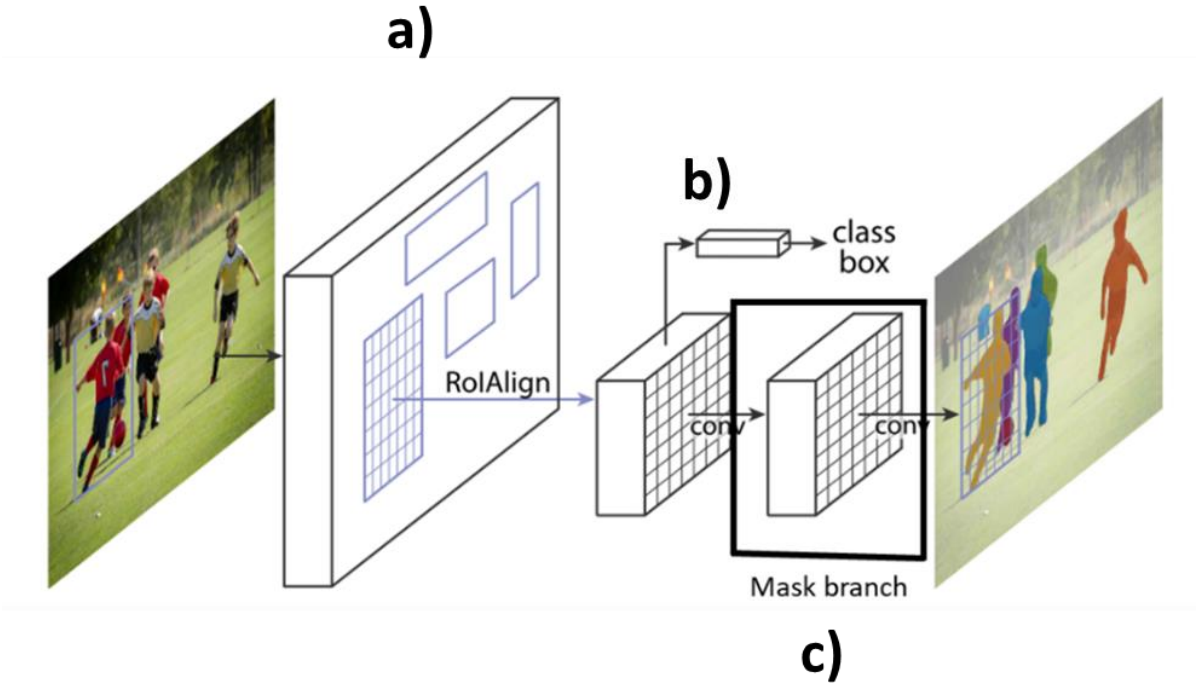

Figure 20 Mask R-CNN architecture (adapted from [64])

In the mask R-CNN approach, object features are highlighted in a first CNN for region proposal (finding *single* objects within the image, here: persons) (a). The features detected in the first CNN stage (i.e. convolutional feature maps of the regions of interest) are shared with the second CNN stage for classification (b) and the third CNN stage for mask generation. This parallel-step structure speeds up image processing and allows for segmentation of *individual* objects within the image.

While further progress is being made in this sector, classification and segmentation results are currently increasingly dependent on appropriate datasets. CNN-based algorithms are particularly dependent on large datasets, thus I will briefly describe important factors in dataset development.

1.5.7 Datasets

As CNN training relies on appropriate feature detection, a large collection of feature examples needs to be available for the training of a new algorithm. Essentially, the collection must account for differences that affect the feature quality in an image, e.g. in angle, shading, shape, pose, distance, and color of an object. Therefore, exemplary situations need to be present in such a highly heterogeneous dataset. The classifier will eventually learn from the diverse features present in the dataset but will be limited by overrepresentation of single features. For instance, if a dataset contains nothing but front views of a red car, the resulting algorithm will not work correctly on the rear view of a yellow car. Diversity is overwhelming in everyday images. Thus, image collections for common objects can reach enormous sizes (see the Imagenet database[67]: 1.2 million labeled images, coco dataset[68]: 330,000 images with >2.5 million labeled instances). In life science research, this diversity is often restricted to grayscale images (e.g. CT, MRI, or X-ray scans) or limited in the availability of angles or distances within a single image (e.g. microscopy). Therefore, scientific datasets are often restricted to relatively small-scale collections from single setups, single magnifications, and

often even single measurements. Although resulting algorithms, arising from such homogeneous datasets often show overwhelming precision when applied to data from the very same instrument, reproducibility when using other instruments is often weak. The lack in reproducibiity with diverse data sets is the reason why computer vision algorithms are regularly retrained on specific datasets[69]. Therefore, in many fields of science, heterogeneous image datasets should not be built upon color or angle diversity but should instead rely on heterogeneous imaging modalities with multiple setups or varying magnification and resolution. In addition, biological entities such as cells in culture or tumors on a CT scan tend to show remarkable variability, therefore, a special focus must be put on shape heterogeneity. Building appropriate datasets is crucial for future algorithm development and therefore of key interest for computer scientists and automation engineers.

1.5.8 Evaluation

Evaluation of segmentation algorithms is often based on precise values. In classification tasks, precision relates the number of correctly detected instances (true positives) to the number of *all* detections, no matter if correct or incorrect (false positives).

$$Precision = \frac{True\ Positives}{True\ Positives + False\ Positives} \quad \textbf{1.8}$$

However, the obstacle in defining "true positive" detection clearly arises. When is a detected mask accurately representing the pixel area of the object within the image? To solve this issue, the intersection over union (IoU) score is employed which divides the overlapping area of two objects A and B (see **Figure 21a**), and divides it by the area of union of A and B (see **Figure** 21**b**).

$$IoU = \frac{A \cap B}{A \cup B} \quad \textbf{1.9}$$

Figure 21c displays area overlaps corresponding to their IoU scores from 0.33 to 0.75. This concept is used to characterize instances detected according to the overlap shared with the ground truth segmentation area. True positives are regarded as such if they exceed predetermined IoU thresholds. For more details on the thresholds used see chapter 2.3.3.

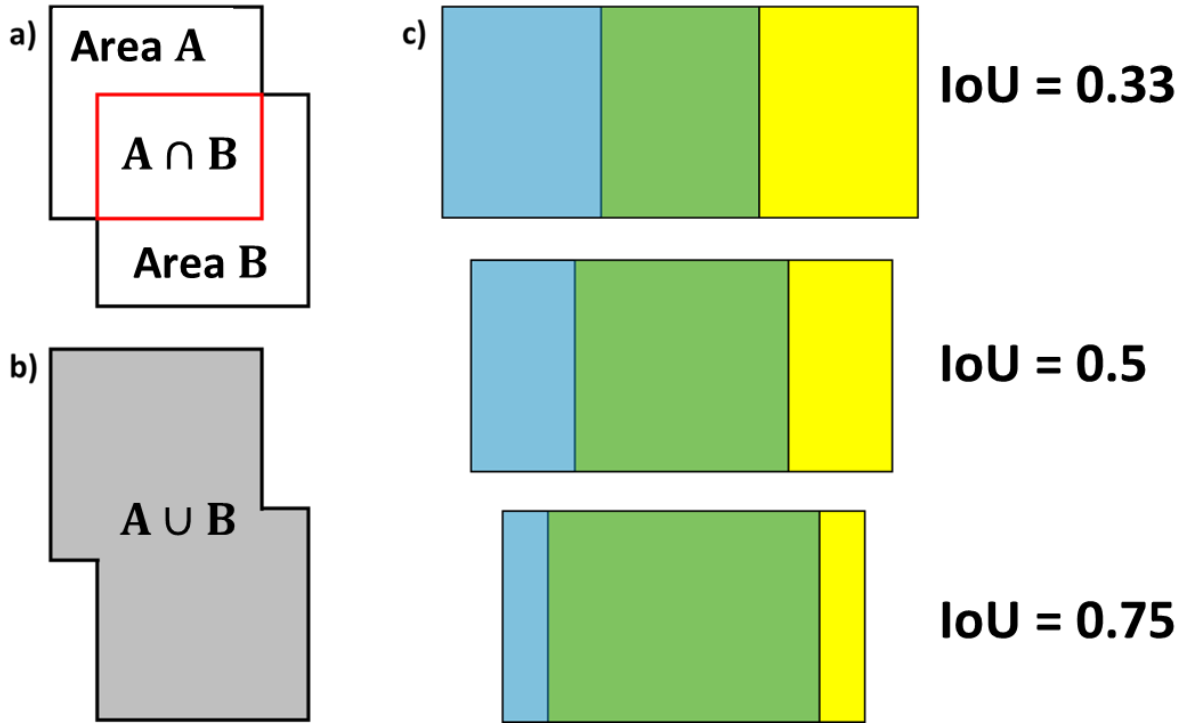

Figure 21 Concept of Intersection over Union

Two areas A and B overlapping with intersection shown in red frame (a). Union of areas A and B in gray (b). Overlapping areas with respective IoU scores (c).

2 Experimental Methods

In this chapter I will introduce the core methods used in this thesis. As this work was driven by interdisciplinary approaches, combining bench work with computational methods, I categorized the methods in three types: wet lab, semi-dry lab and dry lab (see **Figure 22**).

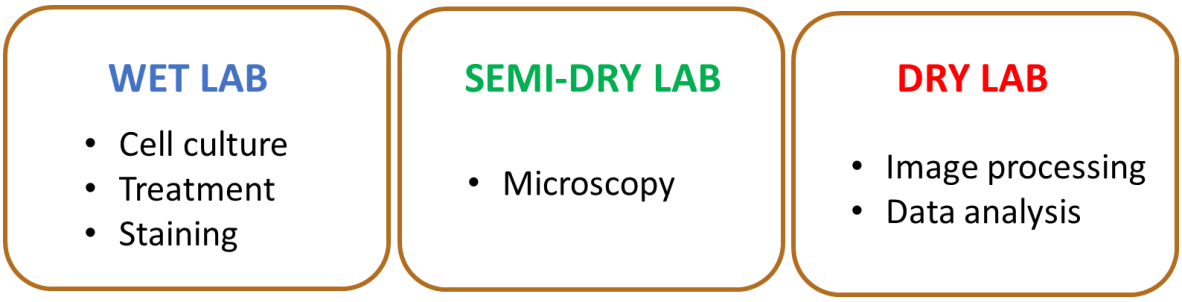

Figure 22 - Methods can be divided in wet lab, semi-dry lab and dry lab work

First, cell cultivation, cell treatments as well as cell staining are described. Subsequently, the applied microscopy techniques, including confocal and automated high-content screening systems are introduced. Lastly, computational approaches such as image processing and data interpretation are explained.

2.1 Cell culture

In this work, a multitude of cell lines was cultured for different purposes. Amongst the most important was THP-1, a monocytic cell line derived from the blood of a one-year old monocytic leukemia patient in 1980[70]. It was used as a model cell line for lipid uptake studies and its handling was therefore of importance for the following subchapters. Hence, the differentiation protocol and general cultivation procedure is introduced here. For further details, see Chapters 3 and 4. One hallmark of these cells is the adoption of a macrophage-like phenotype upon initiation of differentiation using phorbol esters. The transformation of the suspension cell line THP-1 to the adherent macrophage phenotype is accompanied by reduced proliferation, higher rates of phagocytosis and a resemblance to macrophages in the vascular wall[71]. In Chapter 4, the cell line was used as a model for lipid accumulation in macrophages within the arterial wall as previously described[71]. If not stated otherwise, differentiation was initiated by employing a protocol described by Chanput *et al*[72], in which cells were treated with phorbol-12-myristate-13-acetate (PMA) (Sigma) for 48 hours before entering a recovery phase of 24 hours, during which macrophage markers increase. RPMI (Gibco) supplemented with 10 % fetal calf serum (FCS) (Gibco) and 10 U/mL Penicillin/Streptomycin (Gibco) was used for culturing and for differentiation of cells. After differentiation, FCS content was reduced to 1 %, if not stated otherwise.

In another study (Chapter 5), a dataset was assembled, which consists of microscopic images of numerous cultured mammalian cell lines. A special focus in selecting these cells was on their representation of a broad range of cellular shapes.

Cell types chosen for this purpose can be categorized in five main tissue-specific groups:

- **Colon:** Colo320, SW-480, HT-29, Caco-2, DLD-1, HCT116, RKO
- **Mammary gland:** T47D, SK-BR-3, MDA-MB-2311, MCF-7
- **Kidney:** 786-O, 769p, ACHN, CAKI-2
- **Prostate:** PC-3, LNCaP, DU-145
- **Bone:** MG-63

Additionally, we used cell lines that are commonly found in cell biological labs, but do not belong to the main tissue groups: HeLa (cervix), HT1080 (connective tissue), NIH/3T3(embryo), RAW 264.7 (Ascites macrophages), HEL 299 (lung), FaDu (pharynx), MCC26 (skin), C2C12 (muscle), CHO-K1 (ovary), hMSC (mesenchymal stem cells), SH-SY5Y (bone marrow neuroblastoma). Details on culture media are given in Chapter 5.

2.1.1 Microscale culture

The parallel cultivation of 30 cell lines is labor intensive and costly in terms of supply materials. For this reason, a microculture was established, using 96-well plates as culture vessels (see **Figure 23**). In this approach, all wells were pre-filled with 200 µL of the cell-specific medium. After this, serial dilutions were carried out with the respective cell line using multichannel pipets, applying step-wise dilution of cell numbers by mixing 100 µL of the previous well into the following well. This resulted in a more than 1000-fold dilution when comparing first and last wells in the column. For reseeding every 3 – 4 days, subconfluent wells for each cell line were picked, medium aspirated, washed with PBS twice, and cells detached with 15 µL of a 0.05 % solution trypsin/EDTA. After detachment, the trypsin containing cell suspension was diluted with respective cell medium to 200 µL of which 100 µL was used for replating into new 96-well plates. To avoid elevated levels of trypsin during experiments, medium in the wells was exchanged after cell attachment (~2 h).

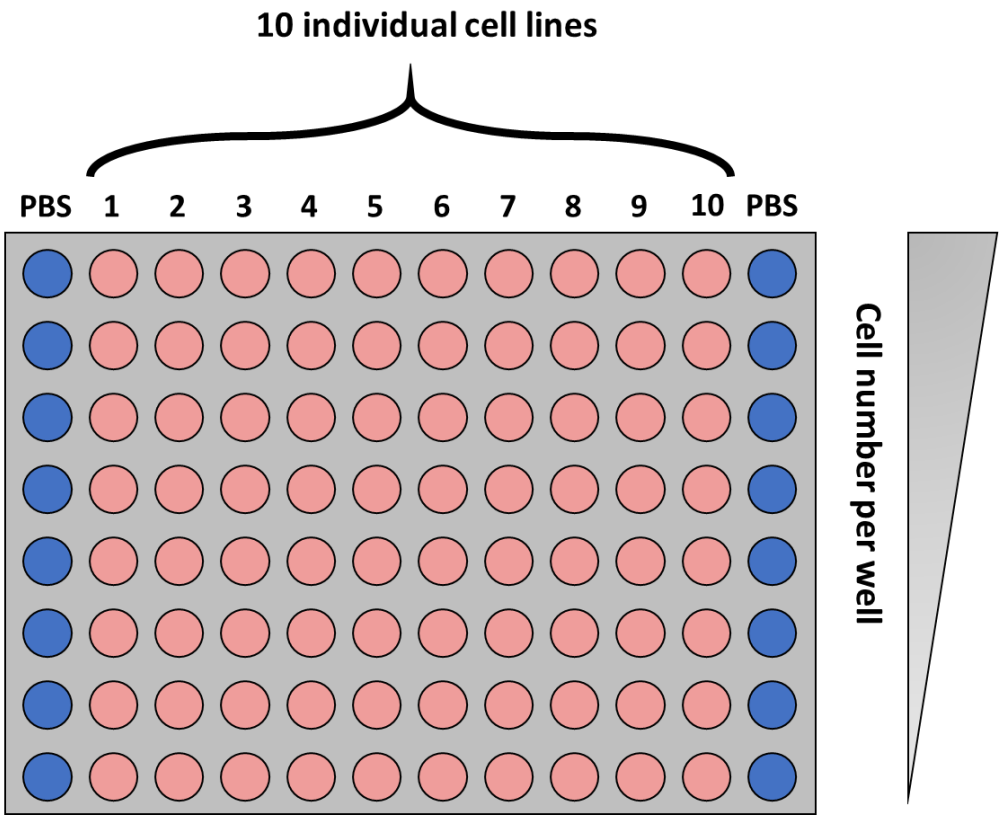

Figure 23 Principle of microscale cell cultivation
Different cell numbers per well were cultured column-wise in 96-well plates. Left and right columns were filled with PBS to account for water evaporation.

2.1.2 Hydrogel culture

One main goal of the thesis was to analyze substrate stiffness mediated effects on cellular lipid uptake. Therefore, a mechanically tunable cell culture vessel was required. For this approach, we cultured THP-1 cells on hydrogel coated vessels using two approaches:

- High-throughput screening format (Matrigen Life Technologies): 96-well plates with a column-wise change in hydrogel stiffness ranging from 0.2 kPa to 50 kPa and glass (several GPa range) as control.
- PetriSoft dishes (Matrigen Life Technologies): Petri dishes coated with hydrogels of defined stiffness for larger cell quantities.

#1.5 glass bottom 96-well plates were used for microscopic intracellular lipid quantification, PetriSoft dishes were used for flow cytometry analyses. Hydrogels were fabricated from polyacrylamide, which can be prepared to exhibit a wide range of stiffness[73]. Stiffness variations in polyacrylamide gels are achieved by tunable degrees of crosslinking using varying concentrations of bisacrylamide as crosslinking reagent. For cell adhesion, all hydrogel and glass surfaces were collagen I-coated by the supplier. Since THP-1 derived macrophages exhibited less adhesion with lower substrate stiffness, hydrogels with Young's moduli below 4 kPa were not used and measurements were focused on surfaces with 4 kPa, 25 kPa, 50 kPa, and glass. A cell density of $3 \cdot 10^4$ cells per cm² was seeded and differentiation initiated on the respective substrate, to allow cellular adaptation to the varying stiffnesses during monocyte

to macrophage transition. Medium was changed by carefully aspirating and refilling at the corners of the vessels to reduce cellular detachment, especially on soft substrates.

2.1.3 LDL modification for cytosolic lipid droplet accumulation

As described in the introduction section, native LDL is subject to negative feedback regulation, which prevents excessive lipid accumulation within the cytosol. To evaluate this in our cells, a modified protocol presented by Khoo *et al*[74] was established to modify LDL by aggregation via vortexing. 1 mg/mL Human LDL (Lee Biosolutions) in PBS was vortexed for 30 s and subsequently mixed with RPMI culture medium containing 1 % FCS and 10 U/mL Penicillin/Streptomycin. The 10% FCS in the culture medium was reduced to decrease bovine lipoprotein levels in the final medium present in serum that could affect the cytosolic lipid content unspecific to human LDL addition. THP-1 derived macrophages were incubated with final concentrations up to 100 µg/mL aggregated LDL (agLDL) and without agLDL in control experiments. Cytosolic lipid droplet (LD) formation was strongly suppressed under control conditions, as expected. Lipid signals moderately increased upon addition of 50 µg/mL LDL while addition of 50 µg/mL aggregated LDL lead to excessive LD formation with cells exhibiting the characteristic foam cell appearance (**Figure 24**).

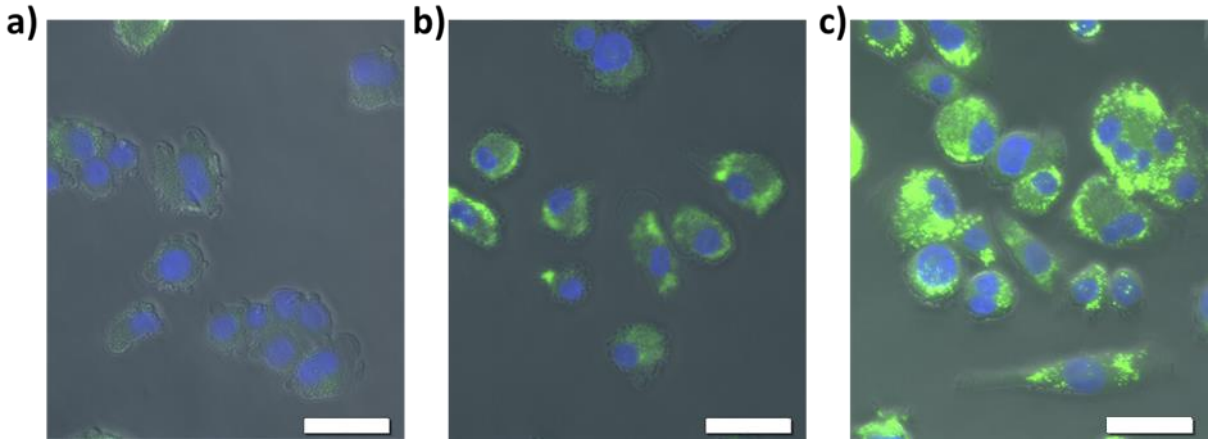

Figure 24 Qualitative comparison of lipid uptake in THP-1:

PMA-differentiated THP-1 were cultured for three days without LDL addition (a), with 50 µg/mL human LDL in native state (b) or after aggregation via vortexing (c). BODIPY staining indicates cytosolic lipid droplet formation (green) increasing from a) to c). DAPI staining indicates nuclei (blue). Scale bars = 50 µm.

To assess the influence of incubation time and LDL concentration on cellular LD formation, lipid signals were quantified during a five-day incubation period with varying concentrations of aggregated LDL (**Figure 25**). Cells were stained with BODIPY for lipids and DAPI for nuclei after three and five days, respectively. Mean lipid fluorescence intensity in the image was divided by number of cells and all results were normalized to the control (LDL-free; 10 % FCS) value after 3 days incubation. Monitoring the lipid uptake showed time- and concentration-dependence, with incubation time having the stronger impact. According to these findings, 100 µg/mL was chosen for agLDL concentration with a five-day incubation time.

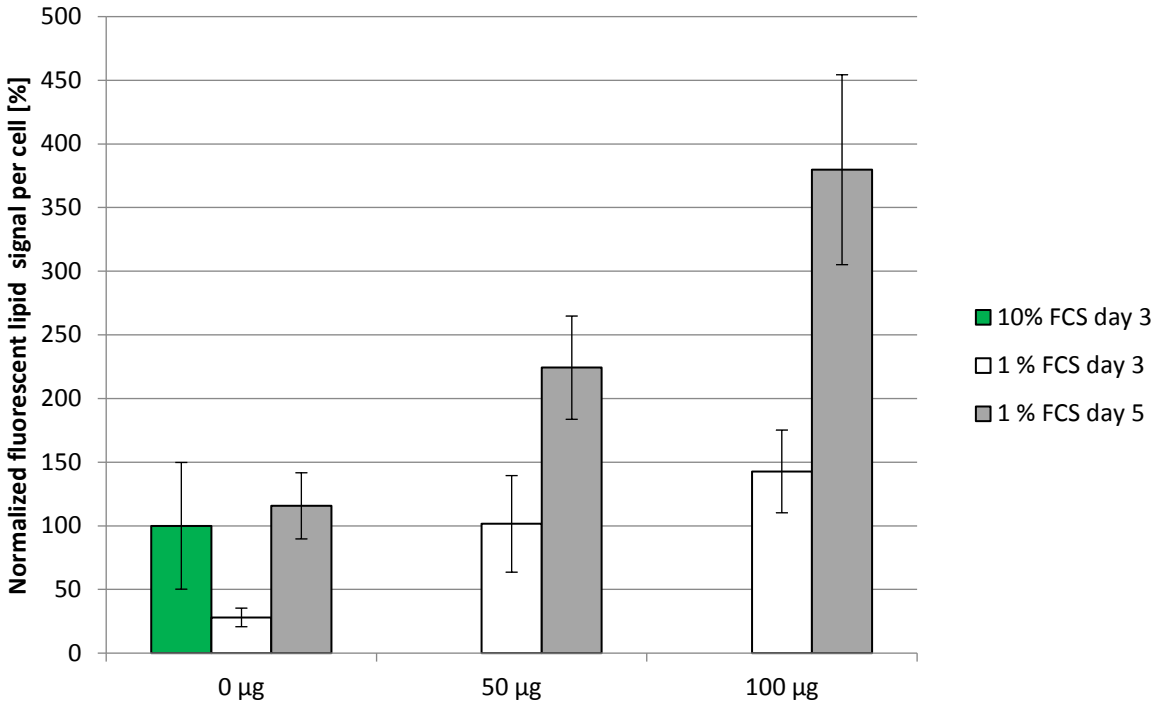

Figure 25 Lipid signal quantification per cell

THP-1 derived macrophages were incubated for 3 days with 10 % FCS containing medium (green) or 3 days (white) and 5 days (gray) without LDL addition, with 50 µg/mL agLDL, and with 100 µg/mL agLDL in 1 % FCS containing medium. Cell samples were stained with BODIPY for lipids and corresponding mean fluorescence intensity for each image was divided by number of cells in the field of view (manually counted). For comparison, all values are normalized to the fluorescence per cell after 3 days in 10 % FCS containing medium. Error bars indicate standard deviation from 12 microscopic fields of view acquired in 3 independent, pooled experiments.

2.1.4 Cytoskeletal drug treatment

To assess the influence of cytoskeletal components on stiffness-mediated lipid uptake, two different cytoskeletal drugs were applied:

- Latrunculin A binds monomeric actin units and thereby prevents polymerization[75,76]. Latrunculin A has been shown to inhibit actin cytoskeleton assembly in various cell types including human bone marrow stromal cells[77], human mesenchymal stem cells[78], and macrophages[45].
- Colchicine binds to tubulin and inhibits microtubule polymerization[79], its applicability in cell culture experiments was demonstrated before[80,81].

Latrunculin A was administered at 1 mM and Colchicine at 10 mM. Efficacy of drug treatments was demonstrated by confocal fluorescent microscopic imaging (**Figure 26**).

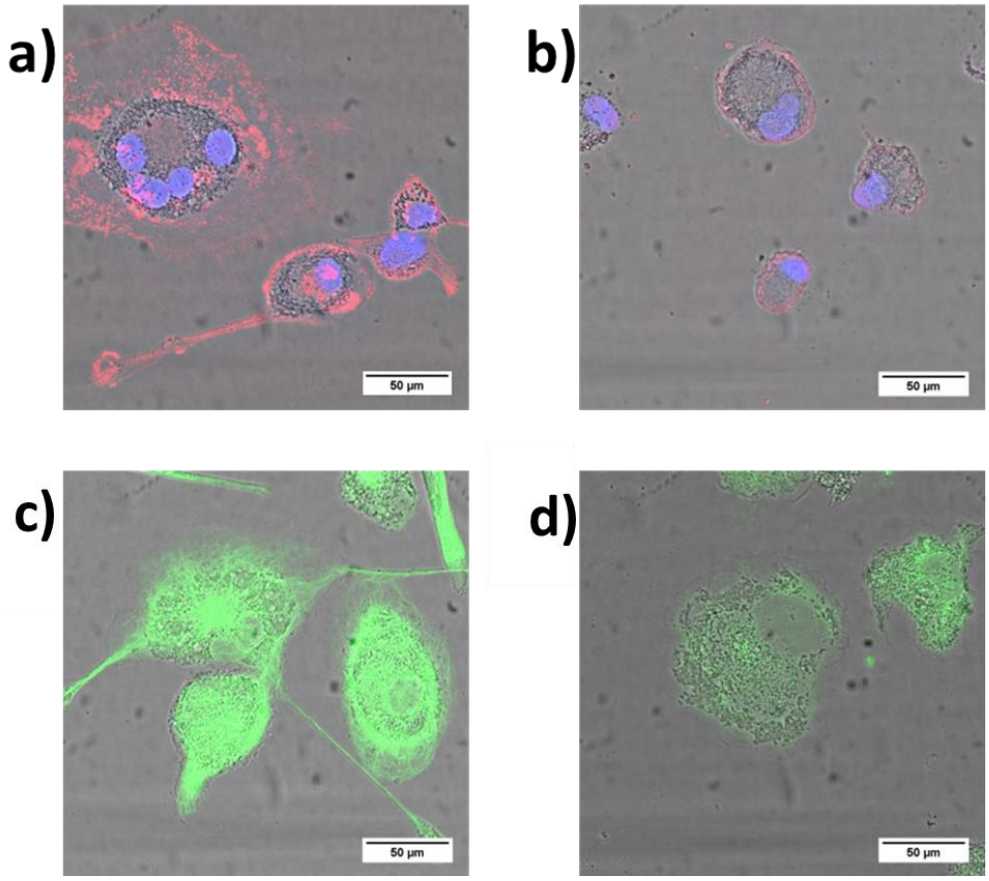

Figure 26 Effects of the applied cytoskeletal drugs on THP-1 derived macrophages

Actin filaments stained with 555-Phalloidin (red) show broad cell spreading in native state without drug application (a), Latrunculin A treatment prevents cell spreading and leads to spherical shape, with no visible filamentous actin (b). Microtubule staining using Tubulin Tracker shows filamentous structures in native state (c) and no polymerization during colchicine treatment (d).

2.1.5 Cell staining

As described in the introductory section, fluorescence microscopy is dependent on accurate staining of the observed specimen. We applied fluorescent dyes as well as fluorophore coupled antibody staining. While most fluorescent dyes stain chemical moieties upon integration (e.g. intercalation into the DNA or preferred solvation in lipids), antibody staining is highly specific to proteinogenic domains. Therefore, chemical dyes were used for nucleus, membrane, and lipid droplet staining prior to fluorescence microscopic imaging, while antibodies were applied to test for expression of proteinogenic differentiation markers in the cell membrane using flow cytometry (FC).

The most important dye used in this work was the membrane permeable fluorescent dye DRAQ5. DRAQ5 is often used for staining the nucleus and exhibits a maximum excitation around 647 nm and emission between 665 nm and 780 nm[82]. Excitation and emission in the red color spectrum allows the simultaneous use of DRAQ5 with frequently applied fluorophores like fluorescein, CY3, or EGFP with lower emission spectra. DRAQ5 shows a particular imprecision, as its staining activity is not restricted to the primary target nucleus, but also weakly stains the cytosol (because of missing fluorescence enhancement upon DNA-binding[82]). This feature makes the dye a unique candidate for the cell segmentation algorithm

studies, as it shows an intensifying signal gradient from the cell borders towards the nuclei enabling cell body detection via thresholding and the identification of individual cells by watershedding using nuclei as seeds. Cell samples were washed three times with PBS and stained for 40 minutes with 5 µM DRAQ5 in PBS (in contrast to common protocols applying 15 mins[82]). After staining, cells were washed three times with PBS to reduce unwanted non-cellular background fluorescence during imaging.

To quantify intracellular lipid volumes in images in Chapter 4, cells were stained with BODIPY. This dye stains neutral lipids and is therefore highly specific for lipid droplets[83]. Its narrow excitation and emission peaks at 493 and 503, respectively, do not interfere with DRAQ5, which was essential when combining DRAQ5 based cell segmentation with BODIPY based lipid quantification stainings. Antibodies directed against human CD36 and scavenger receptor A (SRA) were used to determine expression of the respective protein on agLDL treated THP-1 derived macrophages (see Table 1). These cells were subjected to FC analysis, which is described in Chapter 4.

Table 2 Antibodies and Fluorophores used for labeling

Antibody	**Fluorophore**	**Host**	**Supplier (catalog number)**
Anti-SRA	Alexa Fluor 647	Mouse	Santa Cruz (sc-166184)
Anti-CD36	Phycoerythrin	Mouse	EXBIO (1P-451-T025)

For the creation of the image dataset in Chapter 5, cell membranes and nuclei were stained to facilitate manual ground truth determinations of cellular and nuclear segmentation lines. CellMask Orange was applied to stain plasma membranes as previously described[84,85] and DAPI for nucleus staining[86,87].

2.2 Microscopic analyses

2.2.1 Confocal microscopy

Confocal microscopy was used for optical sectioning of stained cells (see **Figure 27**). Shifting the focal plane by the step size d several times while moving through the cell results in a volumetric Z-stack with depth D. The step size must be chosen larger than the theoretical depth resolution of the objective to avoid multiple detections of the same entity by overlapping Z-regions from lower or higher image planes.

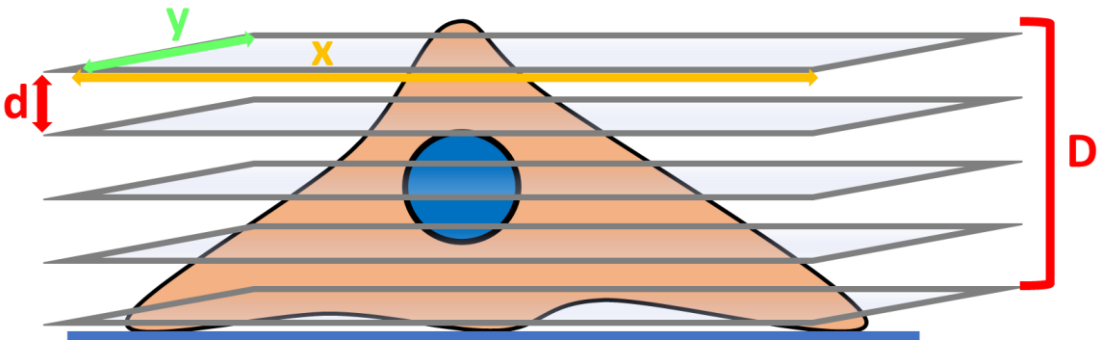

Figure 27 Optical sectioning of cells using confocal microscopic imaging

Image planes (gray) separated by step size d were generated by scanning stepwise through the specimen, collecting a stack of 2D images, spanning a total depth D. Multiplication of image width x and height y with depth D results in 3D volume covered by the Z-stack.

All measurements were performed on a TCS SP5 confocal microscope (Leica Microsystems), using a HeNe laser set to 632.8 nm for excitation and fluorescent emission detection set to 680 – 730 nm. Detector gain was adjusted for minimum saturation within the nucleus to use nuclei as maxima for each cell during downstream image processing. As cytosolic fluorescence signals were vital for cell segmentation during image processing, no detector offset was applied which would cut off weak signals. Confocal stacks with a step size of 1.51 µm between each image plane were recorded. Lateral resolution was 0.6 µm per pixel with image widths and heights of 1024 pixels, respectively. Scanning speed was set to 400 Hz. Detailed information on settings for BODIPY-stained lipid signal acquisition is given in Chapter 4.

2.2.2 High-throughput microscopy

For large-scale experiments using high-throughput microscopy offers a straight-forward solution to produce large amounts of data. To assemble a microscopic image dataset with the diverse set of cell lines described in 2.1, the high-content-screening system Opera Phenix (PerkinElmer), as well as the screening microscope AF7000 (Leica) with a programmable microcontroller was employed. By scanning each well in 96-well plates in brightfield (Opera Phenix) or phase contrast (AF7000) modes as well as with widefield fluorescent microscopy (together), thousands of images were generated using objectives ranging from 10 – 40 X (see **Table 3**). To guide the autofocus algorithms in both systems, plate dimensions were defined and a height range based on manual focus determination at several spots were set. Image acquisition was fully automated and low-quality images (e.g. out of focus images) were discarded manually.

Table 3 Microscope setups, objectives, and Software used for automated image acquisition

Setup	Objectives (part number, magnification, numerical aperture, immersion medium)	Software
Opera Phenix	• HH14000403 10x/0.3 Air • HH14000404 20x/0.4 Air • HH14000422 40x/1.1 Water	Harmony 4.5
AF7000	• HC PL Fluotar 10x/0.3 Air • HC PL Fluotar L 20x/0.4 Air	LASX

2.3 Image processing

All image processing steps for DRAQ5-based cell segmentation are explained in detail in Chapter 3. Therefore, this section will focus on introducing image processing steps utilized to prepare the microscopic image dataset and the training of a machine-learning algorithm. Finally, algorithm evaluation and data interpretation are explained.

2.3.1 Image preparation for manual annotation and dataset creation

Image data for the dataset was produced with automated, as well as conventional setups. The setups consisted of brightfield or phase contrast channels, and if needed, additional channels from fluorescent nucleus and membrane staining. Two versions of each image were generated:

- An 8-bit grayscale image of the brightfield or phase contrast channel without any processing
- A combined RGB image, overlaying all available channels (brightfield or phase contrast channel as grayscale image, fluorescent channels color coded)

The combined RGB image was used for manual cell segmentation to produce training data for the machine-learning algorithm. To enhance contrast in this image, the built-in FIJI auto-contrast function was utilized for each channel. This processing step sometimes resulted in an oversaturated appearance of the fluorescent channels, which complicated the manual identification of cellular or nuclear outlines during the annotation process. To counteract this issue, signals in fluorescent channels were attenuated by a factor of 0.6 after automated contrast adjustment.

Manual ground truth segmentation masks were created by several individuals with cell culture experience using the selection brush tool in FIJI. Five to ten nuclei and cell instances were annotated per image. After manual segmentation was complete, image pixel height and width, as well as polygons of selections were extracted and saved in a JavaScript Object Notation (JSON) text file, using the coco annotation format (see Table 4). This file was a collective library that compiled object annotations from the selection polygons and category inputs and assigned these annotations to the list of images that made up the dataset.

Table 4: Coco-like annotation format used in dataset production

Format	Comments

{
"info": info,
"images": [image],
"licenses": [license],
"annotations": [annotation],
"categories": [category]
}
	General structure
	• Information about dataset
	• List of image dictionaries
	• List of license dictionaries
	• List of annotation dictionaries
	• List of category dictionaries

info
{
"description": "EVICAN 2018 Dataset",
"url": "www…de",
"version": "1.0",
"year": 2018,
"contributor": "Mischa Schwendy",
"date_created": "2018/07/01"
}
	Information about dataset
	• Short description [string]
	• Web access to dataset [string]
	• Version number [string]
	• Creation year [integer]
	• Contributors [string]
	• Exact date of creation [datetime]

image
{
"license": int,
"file_name": "1_C2C12.jpg",
"width": 1200,
"height": 800,
"id": int
}
	Image dictionary (input for list in "images")
	• ID of license applied [integer]
	• Image file name [string]
	• Image pixel width [integer]
	• Image pixel height [integer]
	• Serial number assigned to image [integer]

license
{
"url": "http://creativecommons.org/
Licenses/by-nc-sa/2.0/",
"id": 1,
"name": "Attribution-NonCommercial-
ShareAlike License",
}
	License dictionary (input for list in "licenses")
	• Web access to license[string]
	• Serial number assigned to license [integer]
	• Name of license [string]

annotation
{
"category_id": 1,
"iscrowd": 0,
 	
"image_id": 1,
"id": 1,
"segmentation": [X_1,Y_1,…, X_n,Y_n]
}
	Image dictionary (input for list in "annotations")
	• ID of object category [integer]
	• Crowd identification (0 for individual instances, 1 for group detections) [integer]
	• ID to link respective image [integer]
	• Serial number assigned to annotation [integer]
	• Segmentation points [polygon]

category
{
"supercategory": "Cell",
"id": 1,
"name": "HeLa",
}
	Category dictionary (input for list in "categories")
	• Collective term for similar categories [string]
	• Serial number assigned to category [integer]
	• Name of category (e.g. cell lines) [string]

The dataset was split into three parts:

- Training dataset (4.644 images, partially annotated)
- Validation dataset (1.176 images, partially annotated)
- Evaluation dataset (98 images, fully annotated)

Training a convolutional neural network depends on annotated instances, as well as unannotated background in an image, from which the classifier learns to disregard objects not connected to a learned class. Theoretically, this requires full annotation (i.e. manual segmentation of each cell and each nucleus in all images) of all dataset parts. As the overall cell number in the entire dataset easily surpassed 500000 cells, a complete annotation was not manually feasible. Instead, a background in training and validation images was created by blurring the images with a Gaussian blur, saving the annotated instances plus an additional 10 pixel "buffer zone" surrounding the segmentation outlines. This degraded unannotated cells, that otherwise would have been associated as the "background class" by the trained algorithm. In addition to these processed background images, the background class must include objects common in microscopy but not associated with living cells (e.g. cell debris, scratches on the glass surface, diffractions from bubbles in the medium). Therefore, unprocessed background images also including debris, scale bars, etc. were included in the dataset (750 in the training part, 250 in the validation part). The evaluation dataset was used to test the algorithm produced with real imaging modalities. Therefore, the evaluation dataset was fully annotated manually (i.e. *all* cells in *all* images of the evaluation dataset) without any image processing (i.e. raw brightfield or phase contrast images).

2.3.2 Algorithm training

During training of a CNN-based machine-learning algorithm, weights and therefore convolutional kernels are adjusted based on annotated instances in the training dataset. As training is a stepwise process, one small batch of images from the training set is picked randomly and passed through the CNN. Predictions of annotated instances within a training image are counted as correct, if class prediction (e.g. "nucleus" class) matches the provided class label and mask prediction (i.e. detected segmentation area) and matches the provided ground truth segmentation area with IoU scores above 0.5. After each step, weights in the CNN are incrementally updated to better fit to a detection of instances in the last batch of images. To create an algorithm that is independent of individual image properties (e.g. brightness, microscopic technique, resolution) and more specific to the object class features (e.g. granularity, protrusions), a large quantity of images needs to be passed through the CNN and correspondingly adjusted weights. Based on this, the majority of partially annotated images was used for training. To further increase the diversity of available data, a set of image augmentation techniques was applied randomly for each step:

- horizontal and vertical mirroring
- 90°, 180°, and 270° rotations
- Rescaling between 50 % and 150 % of the original image size

The computer vision algorithm applied in this thesis was a mask R-CNN implementation in python using the machine learning library TensorFlow and the CNN library Keras. The software released by Matterport Inc.[88] (under an MIT license) was originally designed for every-day

scene segmentation and classification. The underlying CNN structure was based on a previously published network called ResNet-101[89] comprised of 101 convolutional layers subdivided into 5 stages and so called network "heads". Network heads were fully convolutional layers for class prediction based on the features extracted by the convolution process. A simultaneous training of **all** layers without pre-adjustment resulted in poor training efficiency. Hence, the training process was subdivided into three parts: first the network heads were trained (i.e. using convolutional filters previously designed for every-day scene images without adaptation and limited by only adjusting the decision-making process for class prediction and mask generation). The next training step consisted of using the last convolutional stages, i.e. the 4^{th} and 5^{th} stages of the ResNet-101 structure adapted convolutional filters for motif-recognition. In the last step, the training process was finetuned to all layers (i.e. also containing the early convolutional stages, detecting low-level features such as edge-detection or color sorting).

In practice, the CNN training schedule was performed using 2 images per training step. Training steps are essentially forward passes of images through the CNN with subsequent backpropagation to adapt image filters or the weighting process in fully connected layers. 1000 training steps were bundled to form an "epoch", i.e. each epoch consisted of 2000 image passes through the network with subsequent adjustment of the weights. After *each* training epoch, 25 validation steps with a batch size of 2 were executed, i.e. 50 images were passed through the network and checked for accurate segmentation and classification. Validation was performed on a separate dataset to prevent a mislead test process: Testing images that were used for training does not provide insight into the general applicability of the algorithm on other images. Network heads were trained for 40 epochs, 4^{th} and 5^{th} stages for 8 epochs, and finetuning on all layers was performed in 4 epochs. I.e. in total, 104,000 images were passed through the CNN for training.

2.3.3 Algorithm evaluation

The trained algorithm's capability to correctly detect instances in an image was tested on 98 fully annotated images in the evaluation dataset part. Average precision (AP), as defined in Chapter 1, was calculated on the basis of IoU thresholds:

- $AP_{0.5}$ denotes the average precision at IoU thresholds of 50 %
- $AP_{0.75}$ applies for precision at IoU thresholds of 75 %
- AP corresponds to the averaged AP-values at IoU thresholds incrementally increased from 50 – 95 % in 5 % steps (Averaged $AP_{0.5}$, $AP_{0.55}$,…,$AP_{0.90}$, and $AP_{0.95}$)

2.3.4 Data interpretation

Results generated with this method included object area, circularity, and aspect ratio. The importance of these parameters in a cellular context is reviewed in brief below:

- Projected cell area
  One of the most valuable information features of cells is their area. It provides a quantitative, often characteristic description of cell size that is subject to little change even during cell movement. It carries information about proliferation, enables categorization into subgroups and measures cell spreading. Cell area analysis can be used in several experimental contexts where cell sizes are expected to decrease, for

example, for the comparison of cellular growth on hydrogels of different stiffness or in the application of cytoskeletal drugs that restrict cell spreading. It can often be more accurate to normalize downstream measured intracellular entities to cell area than on a per cell basis to account for differently sized cells within a given population.

- Circularity
  The circularity parameter relates the area of a detected object to its perimeter.
  $$Circ = 4 \cdot \frac{Area}{(Perimeter)^2}$$
  In the case where the object has a perfect circle shape, that is, with the highest possible area to perimeter ratio, then the circularity parameter equals 1. From a perfect circle shape the perimeter can increase with the area staying constant, but not vice versa. Therefore, it follows that the circularity will approach 0 with increasing perimeter in the denominator.
  Based on the above, a cell, will have lower circularity values the less even its silhouette is. As this can be exhibited by several phenotypes including one dimensional elongation, the formation of pseudopodia, or the apparent surface roughness formed by lamellipodiae, one cannot rely on circularity as a single shape descriptor.
- Aspect ratio
  If the goal of an experiment is to probe the axial elongation of cells, the best marker to use is the aspect ratio. The aspect ratio relates the length of the major axis to the length of the minor axis of an ellipse that is fitted to the object. In a cellular context this means that the longest side is divided by the shortest side of an elliptic cell. High values in this parameter represent a high degree of elongation.
  $$AR = \frac{\text{major axis}}{\text{minor axis}}$$

These three parameters provide robust quantitative measures for commonly observed qualitative cell shapes.

3 Automated cell segmentation in FIJI® using the DRAQ5 nuclear dye

Submitted.

Mischa Schwendy[1,*], Ronald E. Unger[2], Mischa Bonn[1], Sapun H. Parekh[1,*]

[1] Max Planck Institute for Polymer Research, Ackermannweg 10, 55128 Mainz, Germany

[2] Institute of Pathology, Universitätsmedizin-Mainz, Langenbeckstraße 1, 55131 Mainz, Germany

[*] corresponding authors: schwendym@mpip-mainz.mpg.de, parekh@mpip-mainz.mpg.de

3.1 Abstract

Background: Image segmentation and quantification are essential steps in quantitative cellular analysis. In this work, we present a fast, customizable, and unsupervised cell segmentation method that is based solely on Fiji (is just ImageJ)®, one of the most commonly used open-source software packages for microscopy analysis. In our method, the "leaky" fluorescence from the DNA stain DRAQ5 is used for automated nucleus detection and 2D cell segmentation.

Results: Based on an evaluation with HeLa cells compared to human counting, our algorithm reached accuracy levels above 0.92 and sensitivity levels of 0.94. 86 % of the evaluated cells were segmented correctly, and the average intersection over union score of detected segmentation frames to manually segmented cells was above 0.83. Using this approach, we quantified changes in the projected cell area, circularity, and aspect ratio of THP-1 cells differentiating from monocytes to macrophages, observing significant cell growth and a transition from circular to elongated form. In a second application, we quantified changes in the projected cell area of CHO cells upon lowering the incubation temperature, a common stimulus to increase protein production in biotechnology applications, and found a stark decrease in cell area.

Conclusions: Our method is straightforward and easily applicable using our staining protocol. We believe this method will help other non-image processing specialists use microscopy for quantitative image analysis.

3.2 Background

Fluorescence microscopy is the method of choice to visualize specific cellular organelles, proteins, or nucleic acids with high sensitivity and selectivity. Importantly, fluorescence is, in principle, quantitative in that intensity of fluorescence from each position in a sample is proportional to the abundance of the fluorescent moiety in that region of the sample. Once fluorescence images are properly corrected, quantitative image processing can provide abundant information about the imaged species – most notably its spatial distribution within single cells[90–92]. The commercialization of automated microscopes, together with thousands of different fluorescent proteins, cell stains, and digital microscopy, has catalyzed the production of a staggering amount of high-quality imaging data. Thus, it is indispensable to automate the process of image quantification of which one essential step is image segmentation, i.e., the selection and compartmentalization of regions of interest (ROI) within the image. In mammalian cell culture experiments, which are the focus of this work, these ROIs are quite often single cells.

Proprietary image processing software from microscope manufacturers or software specialists such as Imaris or Metamorph offer potent and ready-to-use solutions for image segmentation and further processing. These programs are user-friendly and do not require deep knowledge of data processing nor any programming skills but require a monetary expenditure. CellProfiler is an open-source, alternative tool that offers a platform with a graphical user interface to customize a pipeline for cell detection and geometric quantification based on pre-programmed methods[91]. The method presented in this work is an algorithm built within FIJI (is just ImageJ)® – hereafter called FIJI, a popular and effective alternative to CellProfiler, which is bundled with the open-source Micro-Manger microscopy control software[93,94]. Because FIJI is widely used in the microscopy community, it offers a broad toolbox with several

basic and (user-provided) advanced processing steps (via plugins) that can be combined to produce powerful image processing methods.

Automated fluorescence microscopy based cell segmentation algorithms from cytoplasmic stains can exhibit correct segmentation results above 89 %[95]. Modern computer vision algorithms for cell microscopy generate highly accurate segmentation lines with intersection over union (IoU) scores above 0.9, even in unstained samples (U-Net)[96]. However, training computer vision algorithms requires large annotated datasets and can be challenging to adapt for additional imaging modalities when the training dataset does not sufficiently account for image diversity. In this contribution, we present a practical, automated algorithm for mammalian cell segmentation and geometric feature quantification in FIJI that can be extracted from fluorescent images using a single nuclear stain – in this case, DRAQ5, as opposed to more frequently used cell body stains. Because DRAQ5 does not exhibit fluorescence enhancement upon intercalating into DNA, as opposed to the almost omnipresent DAPI, it produces a moderate, “leaky”, cytosolic fluorescent DRAQ5 signal, which is still detectable within the dynamic range of our PMT in the confocal microscope. This “leaky” signal is crucial for our cell segmentation method. Our algorithm is based on appropriate background subtraction and the identification of the weak cytosolic DRAQ5 signals to properly identify cell bodies. Subsequent watershedding using the strong nuclear signal as the respective local maxima allows for efficient, and more importantly, accurate cell border detection. The modularity and delivery of our algorithm as an ImageJ macro should make it readily customizable to other end user's needs. Moreover, it should be no problem to use this algorithm with other nuclear dyes so long as the dye exhibits sufficient cytosolic fluorescence along with strong nuclear fluorescence.

We start by describing the algorithm and demonstrating its quantitative accuracy by comparing automated analysis against human detection of HeLa cells. In two applications of our algorithm, we analyzed the cell growth of THP-1 cells during differentiation and the change in spreading area of Chinese hamster ovary (CHO) cells during low-temperature cultivation – a perturbation regularly used for biotechnology applications[97].

3.3 Results

Algorithm development

The overall processing scheme is outlined below in **Scheme 1**.

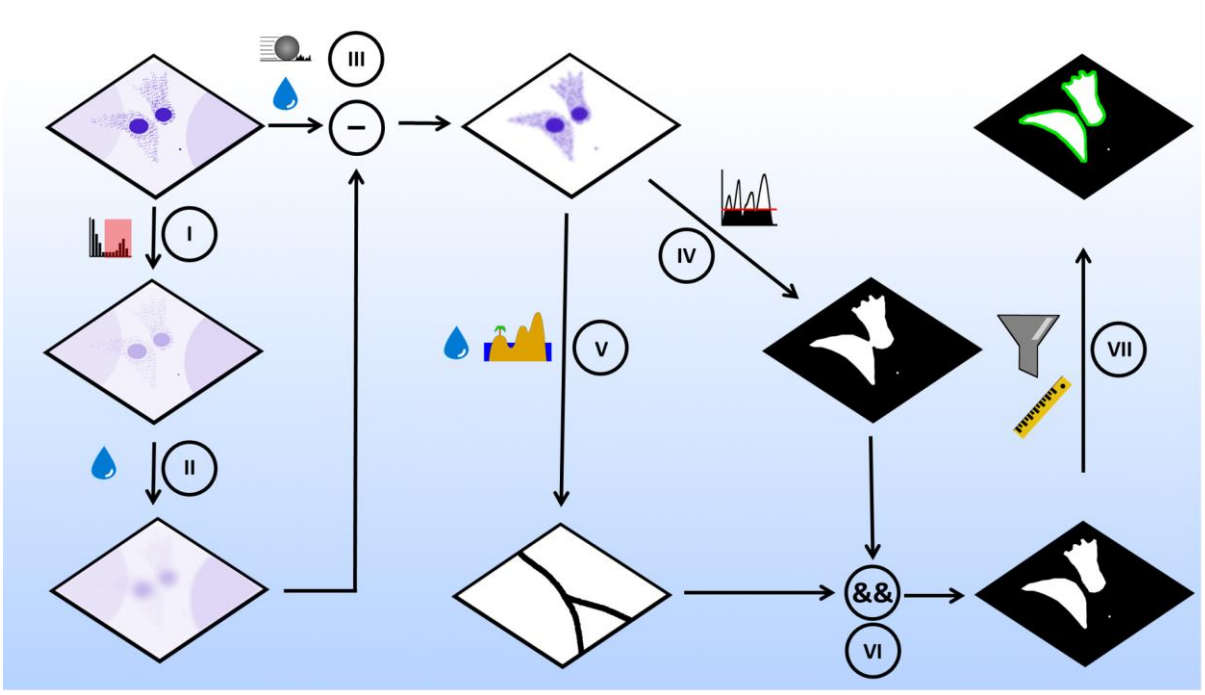

Scheme 1 Steps in image processing and segmentation algorithm.
(**I,II**): Production of a subtraction mask for background subtraction by duplicating the raw image and constraining maximum to three-fold the mean gray value of the image **(I)**. Gaussian blurring (shown here as the water droplet) of the constrained image **(II)** generates a background image for background subtraction in **III**. **III**: The background in the original Z-projected image is reduced via a double subtraction step. First, a rolling ball subtraction is performed (ball radius is set larger than cell radius, to leave the cytosolic signal unaffected) with a subsequent Gaussian blurring of remaining punctate background signals. Secondly, the background image (made in **II**) is subtracted from the (already background reduced) version of the original image. This background subtraction procedure results in an almost flat background image containing only nuclear and cytosolic intensity components. **IV**: Thresholding the blurred, background-subtracted image results in a binary cytosol mask. **V**: The image from **III** was further blurred, and watershedded to produce a binary image of lines that split touching cells. **VI**: The logical (pixel-wise) AND operation combined cytosolic mask (from **V**) and the watershed lines (from **VI**) to a binary image of segmented cells. **VII**: Particle analysis with a size filter allows neglecting small particles in the image and selection of the segmented cells for further analysis.

All image processing was performed on a Z-projected image – projected according to the standard deviation – of DRAQ5 fluorescence; each pixel in the projected image had an intensity value given by the standard deviation of the pixels in Z-direction. This highlights zones with a high degree of variation in the Z-direction, which enhances weak and punctate signals. To reduce the background signal in Z-projected images caused by uneven illumination or non-specifically bound fluorophores, we applied a two-step process. First, a background image was produced by constraining the maximum of the original image and Gaussian blurring the constrained image with a sigma of 100 µm (**Scheme 1, I and II**). This process coerced high-intensity signals to a new maximum value of the threefold global mean gray value and blurred the leaky cytosolic DRAQ5 signal so that it would remain after subsequent subtraction from the original image. This background image was subtracted from the pre-flattened version of the original Z-projected image that was generated using a rolling ball subtraction with a radius

of 100 µm followed by smoothing with a Gaussian blur filter with a sigma of 1 µm. Subtracting the background image from the processed original image resulted in a near-zero background except for the nuclear and cytosolic DRAQ5 signals (**Scheme 1, III**). The resulting image (from step III) was duplicated and used for thresholding and watershedding (**Scheme 1, IV and V**). Specifically, to produce a binary image of the cell bodies, a threshold at a gray value of 1 was sufficient as all background values were strongly reduced (**Scheme 1, III**). This produced a binary image that highlights complete cell bodies and nuclei. Adjacent and overlapping cells were divided in the further Gaussian blurred (sigma = 2 µm) copy from step III by applying the "find maxima" command with "Segmented Particles" as the output and a noise value given by a threefold mean gray value of all non-zero gray values in the image (**Scheme 1, V**).

Combining the thresholded image (**Scheme 1, IV**) with the watershed lines (**Scheme 1, V)** via the logical (pixel-wise) "AND" operation produced a binary mask of the cell population in the image with juxtaposed cell borders of individual cells separated (**Scheme 1, VI**). A size filter was applied, detecting cells with sizes bigger than 200 µm² to avoid detection of cell debris (**Scheme 1, VII**).

To analyze cell shape, we probed three parameters: projected cell area as a measure of cell spreading, circularity as a measure of cellular protrusions and aspect ratio as a measure of elongation. These quantities are exported in an automated fashion in a table format at the end of the analysis. An example of the Macro is given in the Supplemental Information. All images used in this work and the example Macro is additionally available in[98].

Evaluation of the cell detection and segmentation method

An exemplary output of segmented cells within a processed image is shown in **Figure 28a**. To evaluate the segmentation from the leaky DRAQ5 signal, we used an established approach that relies on manually monitoring the automated detection results on a set of test images[99]; similar human-comparison approaches have been used elsewhere[100,101]. The evaluation was performed by applying the selected frames on the corresponding bright-field image (**Figure** 28**b**), and three individuals, each with more than three years of experience in cell biology, manually counted cells and checked for appropriate segmentation produced by our automated algorithm. Manually checking for correctly segmented cells, true positive (including full cell bodies, largest fragment of over-segmented cells and one cell per under-segmented multi-cell detection), false positive (cell debris, thresholding errors, etc.) and false negative (missed cells, undetected cells in under-segmented multi-cell detections) detections from our algorithm, we found that 86 % of cells were correctly segmented, with accuracy and sensitivity values better than 92 % (**Figure 28c)**. Additionally, comparing the overlap of manually segmented cells (as the ground truth) with algorithm detections yielded an intersection over union (IoU) score (explained in the Methods) of 0.83 ± 0.05.

a

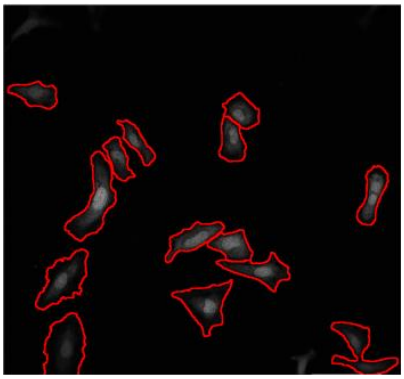

b

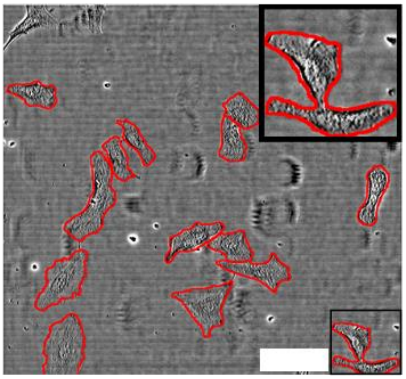

c

Category for comparison	Mean ± SD
Manually counted cells	134 ± 3
Correctly detected cells	116 ± 2
Missed cells	1 ± 2
Under-segmented cells	8 ± 2
Over-segmented cells	2 ± 2
Cell debris	4 ± 2
True positives	126 ± 2
False positives	3 ± 2
False negatives	8 ± 3
Accuracy	0.92 ± .01
Sensitivity	0.94 ± .02

Figure 28 Exemplary output of cellular detection from leaky DRAQ5 staining and evaluation of the automated segmentation algorithm.

a) Z-projected DRAQ5 signal. b) Z-projected brightfield (transmitted laser light) image. Inset shows an example of undersegmented cells. Red lines in a and b are segmentation lines produced by our algorithm. c) Quantitative evaluation of the segmentation algorithm showed mean accuracy and sensitivity values of 0.92 and 0.94 respectively when compared to three human detections. The specific categories are defined in the Methods section. The evaluation was performed on 136 cells in n = 8 images from two experiments. Scale bar is 100 µm.

Having established that our segmentation algorithm was accurate and specific compared to human evaluation and with respect to IoU scores compared to literature (see Discussion for details), we next focused on demonstrating the application of this method in different cell biology applications. We quantifed geometrical features of THP-1 cells during differentiation and spreading characteristics of CHO cells during low-temperature cultivation (often used to increase protein production yield in biotechnology applications – reviewed in[97]).

Quantifying projected area, aspect ratio, and circularity of HeLa and THP-1 from automated cell segmentation

To demonstrate the ability of our algorithm to measure cell morphology accurately, we compared two cell lines with different growth behavior: HeLa and THP-1 cells. We picked freshly differentiated THP-1 (after 48 hours differentiation and 24 hours of recovery) showing a predominantly round, almost protrusion-free shape and HeLa cells showing a larger, more elongated cell shape (**Figure 29a and b**). Both cell lines were cultured on collagen-coated glass-bottom MatTek dishes (as supplied by the manufacturer).

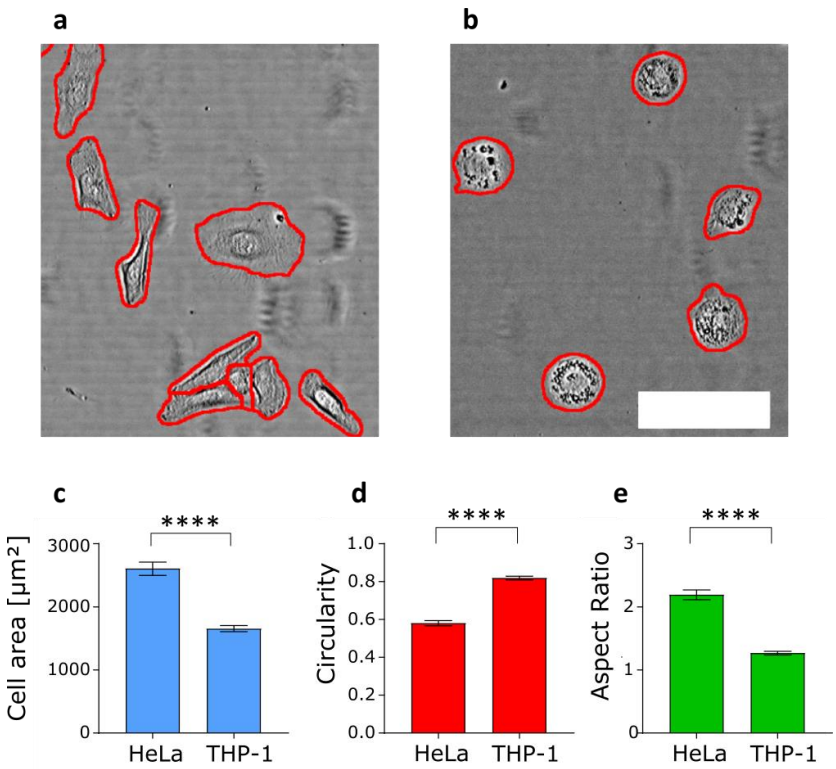

Figure 29 Exemplary images and shape descriptors for HeLa and differentiated THP-1 cells.
a) Brightfield (transmitted laser light) image of HeLa with segmentation lines (red) produced by our algorithm. **b)** Brightfield (transmitted laser light) image of differentiated THP-1 with segmentation lines (red) produced by our algorithm. **c)** Mean projected cell area of differentiated THP-1 and HeLa cells shows that THP-1 cells have a 36 % smaller area compared to HeLa. **d)** Quantification of cell circularity confirms that THP-1 cells have a 41 % higher (mean) circularity value compared to HeLa. **e)** Elongated HeLa cells show a mean aspect ratio above 2 while the round shape of THP-1 is reflected by an aspect ratio ~ 1. Data are shown as mean ± standard error of mean (sem). **** indicates $p < 0.0001$ (t-test). For HeLa, 129 cells in n = 8 images from two pooled experiments were analyzed; for THP-1, 135 cells in n = 13 images from two pooled experiments were analyzed. Scale bar is 100 µm, applicable to both images.

To quantify the different shape characteristics, we measured the projected cell area, cell aspect ratio, and circularity. Briefly, the aspect ratio is defined as the ratio of the major to the minor axis of a fitted ellipse; circularity is defined as $4*(\text{area}/\text{perimeter}^2)$. For example, objects having the shape of a perfect circle, have circularities and aspect ratios equal to 1. Higher aspect ratios are associated with elongation; lower circularity values are associated with cellular protrusions. Detailed information on these parameters is given in the Supplemental Information (**Figure S1**).

We found that HeLa cells show a projected cell area of ~ 2600 µm², a mean circularity of 0.58 and a mean aspect ratio of 2.2. In contrast, differentiated THP-1 showed a cell area of ~ 1650 µm² and were almost perfectly round with a mean circularity of 0.82 and a mean aspect ratio of 1.27 (**Figure 29c - e**). These findings are consistent with the elongated form of HeLa and the smaller round shape of differentiated THP-1 seen in the images of **Figure 29a and b**, respectively.

Cell shape changes during THP-1 differentiation

Previous work has shown that THP-1 cells change their phenotype dramatically during differentiation, as they undergo a transition from suspension to adherent cells during differentiation into macrophage-like cells[102,103]. Therefore, we analyzed cell morphology changes by monitoring cell area, circularity, and aspect ratio from dozens of confocal stacks that contained more than 90 (per day) THP-1 cells over a six-day differentiation and culture period.

Incubating THP-1 with PMA in the culture medium for 48 hours (to initiate differentiation) and subsequently changing to normal medium without PMA resulted in the spreading phenotype shown in **Figure 30a**. Cell area increased sharply within the first 48 hours, subsequently entering a plateau phase without further growth for the next 48 hours before the cells entered another growth phase after day 4 (**Figure 30b**). Interestingly, this second growth phase appears to be accompanied by further shape changes, as both circularity and aspect ratio show statistically significant changes only after day 4. The decreased circularity along with the increased aspect ratio indicates cellular elongation and less smooth, round shapes (**Figure 30b and c**), consistent with the shapes seen in **Figure 30a**.

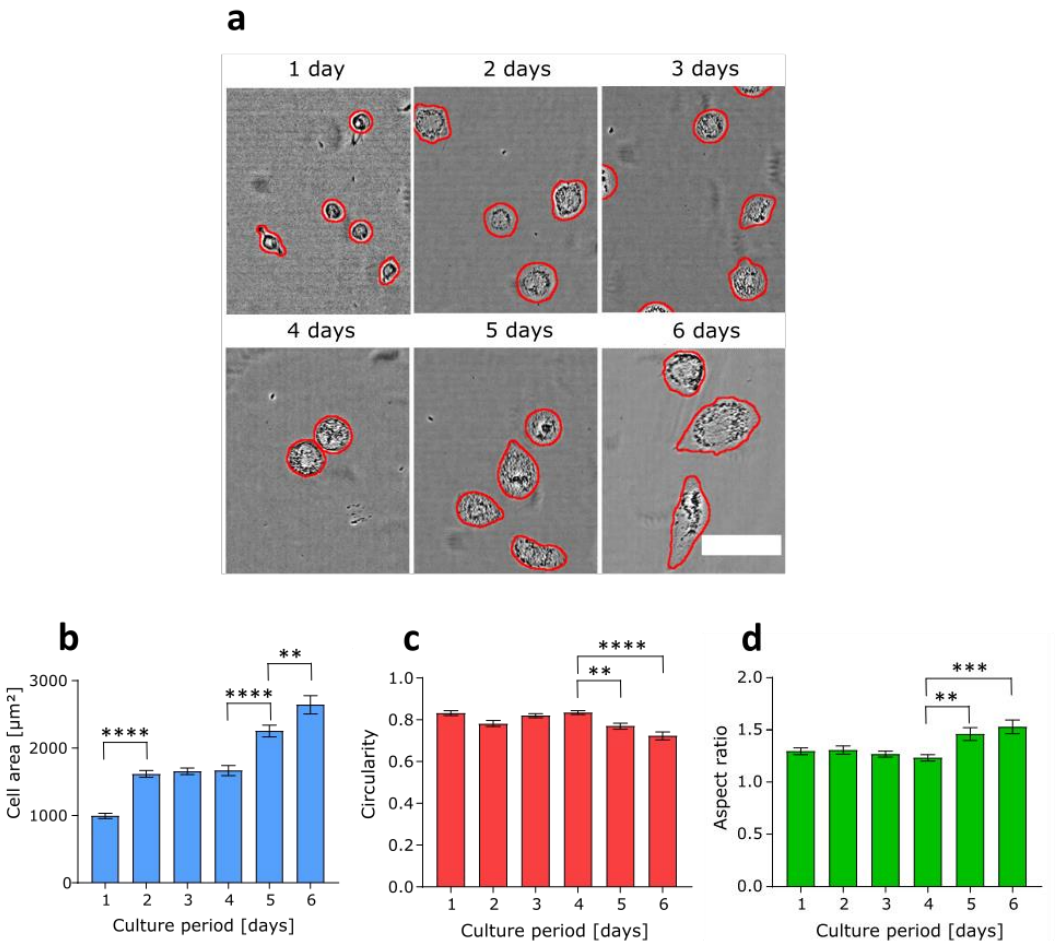

Figure 30 Change in cell area, circularity and aspect ratio during THP-1 differentiation.
a) Exemplary brightfield (transmitted laser light) images of THP-1 cells during the 6 day monitoring phase with segmentation lines (red) produced by our algorithm. **b)** Projected cell area increases during differentiation. After an initial growth phase, cells enter a plateau phase and then show a second period of growth after day 4. **c)** Circularity values stay constant until day 4 before decreasing on day 5 and 6. **d)** Increasing aspect ratio on day 5 and day 6 indicates cellular elongation. These data together highlight the shape change toward a more elongated phenotype at longer times after differentiation. Data are shown as mean ± sem. **,*** and **** indicate p < 0.01, 0.001 and 0.0001, respectively (ANOVA with post-hoc Tukey test). At least 90 cells in n >= 10 images were analyzed from two pooled experiments per day, respectively. Scale bar is 100 µm.

Reduced temperature culture of CHO-cells causes cell shrinkage

As a second application of our cell segmentation algorithm, we analyzed the impact of temperature on projected cell area of CHO cells. Numerous studies have demonstrated how reduced temperature affects cellular growth (via arrest) and increases protein production in CHO cells[104,105]. Higher rates of recombinant protein expression, coupled with extended production phases make temperature an interesting and easily tunable parameter in industrial biotechnological upstream processing.

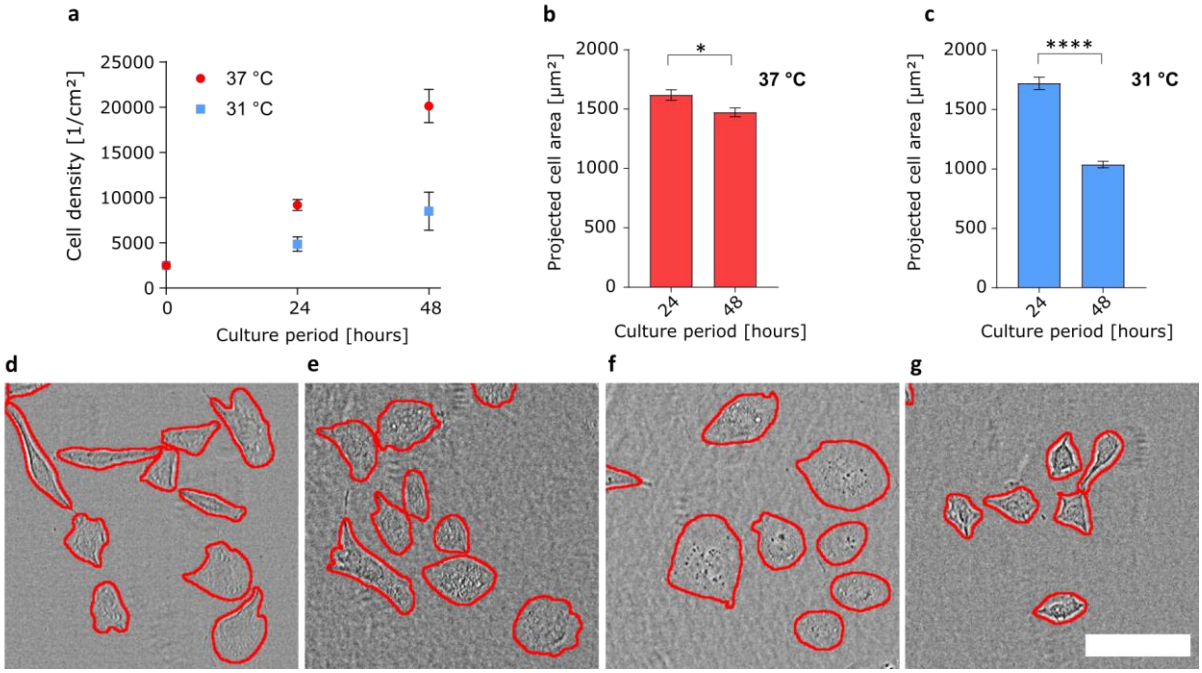

Figure 31 Cell area changes during low-temperature culture of CHO cells.
a) Cell surface density and growth is reduced by 48 hours of CHO culture at 31 °C compared to 37 °C. n = 3 experiments per temperature and day. **b,c)** Projected cell area of CHO cells cultured at 37 °C and 31 °C, respectively, shows that culture at 31°C culture results in a sharp decrease in cell area after 48 hours. For **b)** n = 218 cells at 24 h and n = 494 cells at 48 h in 10 images from 2 pooled experiments, respectively. For **c)** n = 217 cells at 24 h and n = 461 cells at 48 h in 10 images from 2 pooled experiments, respectively. **d – g)** Exemplary brightfield (transmitted laser light) images of CHO cells with segmentation lines (red) produced by our algorithm cultured at 37 °C for 24 hours (**d**), 37 °C for 48 hours (**e**)**,** 31 °C for 24 hours (**f**), 31 °C for 48 hours (**g**)**.** All graphical data are shown as mean ± sem. * and **** indicate $p < 0.05$ and 0.0001, respectively (t-test). Scale bar is 100 µm.

Quantifying cell densities per cm² we found, similarly to prior studies, that CHO cells cultured after a temperature reduction to 31 °C show decreased cell growth[106]. We detected half the growth rate seen for culture at 31 °C compared to control conditions (37 °C) (**Figure 31a**). To evaluate whether this temperature jump had an impact on cell shape, we analyzed the projected cell area of adherent CHO cells cultured at either 31 °C or 37 °C temperature over 48 hours. As shown in **Figure 31b**, cell spreading decreased by less than 10 % after 48 hours of culture at 37 °C (that is, with no temperature perturbation). On the other hand, for CHO cells cultured at 31 °C, we observed values comparable to control conditions after 24 hours of culture, but a steep drop of 40 % in projected cell area after 48 hours (**Figure 31c**). This area reduction can also be seen in the exemplary images in **Figure 31d – g**.

3.4 Discussion

In this study, we showed that it is possible to produce robust and accurate cell segmentation algorithms in FIJI with high accuracy and sensitivity using only a leaky signal from a nuclear stain. Because no additional cell body stain was necessary, this method frees a color for additional cell staining. Our algorithm produced better than 92 % accuracy, 94 % sensitivity,

and 86 % correctly segmented cells compared to human evaluation. This places our algorithm in similar segmentation performance as reported by Wählby *et al.* (above 89 % correct segmentations)[95] and Buggenthin *et al.* (accuracies above 82 % and sensitivities above 94 %)[99]. Additionally, we achieved an average IoU score of 0.83 when comparing our segmentation results to manual segmentation masks. This matches IoU scores of modern computer vision applications reported by Ronneberger *et al.* (0.77 – 0.92)[96].

We suspect that characteristics leading to incorrect counting from our algorithm include substantial cell clumping and a significant contribution from 3D cell growth. In these cases, several nuclei overlay, which ultimately hinders the watershedding process. For optimal quantitative analysis with our method, cells should not exhibit excessive clumping and should be preferably maintained in 2D culture. Additionally, fully confluent cell layers can be a hindrance, as they amplify the values in the subtraction mask and thereby lead to a reduction of "leaky" cytosolic signal in step III of the algorithm.

Compared to other algorithms that perform similar functions – automated segmentation and cell quantification, our algorithm offers both functions while using only a single nuclear dye that can also be used for binary cell counting, is conceptually straightforward, and built on an open-source (FIJI) platform. The comparison in terms of accuracy is on par with other approaches[107,108] in terms of the specificity and error rate. Moreover, the general approach of thresholding combined with edge-detection to outline full cell bodies is in line with classical methods used for microscopy image segmentation[90]. Similar methods have recently been used to evaluate bacterial segmentation[109–111] in the processing suites called MicrobeTracker, CellShape, and SuperSegger, respectively. Of these, MicrobeTracker was recently translated into a FIJI plugin called MicrobeJ[112].

The projected area of HeLa and differentiated THP-1 cells

Determination of cell area of HeLa cells using our algorithm resulted in larger cell areas than reported in literature. However, this can be traced back to different cell culture conditions: Puck *et al*. measured the cell area (1600 µm²) in 1956 using a self-made medium, and it is unclear if this contains similar supplements and additives as is common in today's RPMI-based medium[113]. Missirlis reported a cell area of 1400 µm² for HeLas cultured on a "stiff" substrate, which was a hydrogel of ~85 kPa[114]. As we examined cell area on glass with a Young's modulus of order of GPa and because adherent cells tend to increase area with increasing stiffness[115], a bigger cell area in our experiments is not surprising. Lastly, Frank *et al*.[116] reported a majority of HeLa cells analyzed show areas below 1100 µm². However, these measurements were performed only one hour after cell plating, which may still be during the initial spreading phase and is not comparable to our 24 h culture period. Taken together, and considering the accuracy of the cell outlines shown in our segmentation method, we surmise that our experiments give an accurate quantification of HeLa cell area under standard laboratory conditions after 2 days of seeding on glass bottom dishes.

Cell shape changes during THP-1 differentiation

Our results showed two growth periods of THP-1 from day 1 to 2 and from day 4 onwards, divided by a plateau phase with only minimal growth from day 2 to 4. Simultaneously, after day 4, we observed a trend to less circular, more elongated cell shape. This indicates the tendency to more pronounced cell spreading after a recovery phase of two days following PMA withdrawal. Our findings also potentially raise the question for several studies performed with THP-1 as to whether cell area was taken into consideration, as the increased membrane surface can influence cellular uptake of nutrients and the total number of membrane receptors. Many parameters such as cytokine expression, volume, and lysosomal numbers in THP-1 have been analyzed in detail[103]; however, to the best of our knowledge projected cell area during differentiation has not been correlated to these properties. It might be of further interest to analyze, e.g. cytokine excretion or lipid uptake – processes critical in immunology and pathogenesis – as a function of cell area to see how these parameters are linked to cell shape.

Changes in projected cell area with low-temperature culture

We found a 1.7-fold decreased projected area of CHO cells after 48 hours of culture at 31 °C. Interestingly, Kaufmann *et al.* reported a 1.7-fold increased specific protein productivity in CHO after lowering the culture temperature from 37 °C to 30 °C[106]. These higher production rates may be attributed to CHO cells adopting a quiescent reproduction phenotype, with fewer cell divisions and an accompanying smaller cell area. This could potentially free metabolic resources that could be directed toward protein production; however, this question certainly requires further exploration.

3.5 Conclusions

In this work, we demonstrated an automated process for mammalian cell image segmentation within the open-source scientific image analysis platform FIJI. Our method was developed to segment and identify cells from Z-projected images of the DRAQ5 nuclear dye and produced accuracy levels above 0.92, sensitivity levels of 0.94, and 86 % correctly segmented cells when compared to human evaluation. Using the precise IoU metric, our segmentation gave an IoU score of 0.83; all metrics which are very close to other published algorithms. Applying our algorithm, we measured cell spreading and elongation during THP-1 differentiation to macrophages and cell area reduction of CHO cells that arises in low-temperature cultures often used for protein production. At present, the majority of cell segmentation algorithms, including ours, are based on hard-coded detection of fluorescently-labeled image species. However, with emerging algorithms, especially in the field of computer vision and deep learning, future cell segmentation and analysis could transition to label-free (e.g. brightfield) imaging that enables unperturbed, label-free, and robust monitoring of cell shape as has already been demonstrated for phase contrast and differential interference contrast imaging[96,117,118].

3.6 Methods

Cell culture and staining

Unless stated otherwise, all cell culture experiments were performed at 37 °C and 90% relative humidity, with 10 % fetal calf serum (Gibco) and 10 U/mL Penicillin/Streptomycin (Gibco) added to the respective medium, and with glass bottom culture vessels (MatTek).

HeLa cells (DSMZ no: ACC 57) were cultured in DMEM (Gibco) and THP-1 cells (DSMZ no: ACC 16) in RPMI 1640 medium (Sigma). To initiate differentiation, THP-1 culture medium was supplemented with 100 ng/mL phorbol 12-myristate-13 acetate (PMA) for 48 hours as previously described[72]. This procedure led to the adhesion of almost all cells within 24 hours, which signals the onset of differentiation from monocytes to macrophages [14]. For analysis of temporal changes in cell area during differentiation, THP-1 cells were incubated for an additional 96 hours in full medium without PMA.

Chinese hamster ovary (CHO) cells (CHO-K1, DSMZ: ACC110) were cultured in Ham's F12 medium. For cell density determination, CHOs were cultured in 6-well-plates (Greiner Bio-One) and counted in triplicate using a hemocytometer. For cell area determination, CHO cells were cultured in glass bottom µ-dishes (Ibidi).

After the indicated incubation times, all cells were fixed with 4 % para-formaldehyde in PBS for 10 minutes. Cells were stained with 5 µM DRAQ5 (ThermoFisher) in phosphate-buffered saline (PBS) for 40 min at 37 °C and washed with PBS three times prior to microscopic analysis. Microscope measurements were performed within 24 hours for all experiments.

Image acquisition

Confocal microscopy (Leica TCS SP5 II, Leica) of cells was used to acquire axial cell volumes. More than 100 individual cells of each cell line were imaged using a 25X, 0.95 NA water immersion objective (Leica) with a 632.8 nm HeNe laser excitation. Emission was detected from 680 – 730 nm. Detector gain was set to minimize saturation within the nucleus, and the slice thickness within the Z-stack was set to 1.51 µm. The X-Y spacing was set to 0.6 µm per pixel, and the scanner speed was 400 Hz.

Algorithm evaluation

Three individuals, each having more than three years of cell culture experience, manually evaluated the segmentation results on a test image set. The following paragraph summarizes the measured observables, similarly defined by Buggenthin *et al.*[99].

"Manually counted cells" denotes all cells that are completely contained in the image. Cells found by the algorithm that have more than 90 % of their area within the detected cell frame were counted in the category "correctly segmented cells". "Missed cells" are cells in the image that were not detected by the algorithm. To account for segmentation quality, the two categories "under-segmented cells" and "over-segmented cells" were included. "Under-segmented cells" are multiple cells that are detected as a single instance such that the

detected frame contains more than one cell or single cells that are detected by the algorithm where the frame is much larger than the actual cell. “Over-segmented cells” are instances where only a small section of the cell is detected, or one cell is split into multiple parts. Large cell debris in the image that could potentially be mistaken as a cell by a segmentation algorithm were counted in the “debris” category. For calculation of “accuracy” and “sensitivity”, detected instances were categorized as “true positives” (cells correctly identified by the algorithm, no information about segmentation), “false positives” (cell debris or any other objects that were falsely detected by the algorithm), and “false negatives” (any cells that were not detected by the algorithm in addition to those that were not counted in under-segmented instances). Accuracy was calculated as (true positives) / (true positives + false positives + false negatives) and sensitivity as (true positives) / (true positives + false negatives). “Percent correctly segmented” was calculated as 100*(correctly segmented cells) / (manually counted cells).

Additionally, to quantify the segmentation success, binary ground truth masks of cells in all test images were produced manually, and the intersection over union (IoU) score was calculated for the algorithm segmentation results using the FIJI plugin MorphoLibJ[119].

Statistical analysis

Statistical evaluation was performed using GraphPad Prism 7.0 (GraphPad Software). To test the statistical significance of differences in the cell area, circularity, and aspect ratio of THP-1 and HeLa cells, as well as cell area differences of CHO cells cultured at different temperatures, a two-tailed t-test with Welch’s correction, was applied. For time-dependent changes in cell area, circularity, and aspect ratio during THP-1 differentiation, data were evaluated using analysis of variance (ANOVA) with post-hoc analysis based on the Tukey test. Statistical significance was expressed as *, **,*** and ****, indicating p-values < 0.05, 0.01, 0.001 and 0.0001, respectively.

Availability of data and material

The FIJI macro and the datasets analyzed during the current study are available in the Edmonds repository, https://edmond.mpdl.mpg.de/imeji/collection/quuxweXFiBEQnctM?q=

Competing interests

The authors declare that they have no competing interests.

Funding

M.S. acknowledges generous support by a PhD Fellowship from the Max Planck Graduate Center. S.H.P. acknowledges funding from the DFG #PA 252611-1.

Authors’ contributions

M.S. carried out the cell experiments, microscopic image acquisition, and code generation. R.E.U. and M.B. supervised the project. S.H.P. designed the study, conceived the algorithm with M.S., and supervised the project. M.S. and S.H.P. wrote the manuscript, and all authors edited the manuscript.

Acknowledgements

We gratefully acknowledge Sachin Kumar B, Ravi Dhiman, and Sabine Pütz for manual evaluation of HeLa cells, Frederik F. Fleissner for scientific discussions, Anika Keswani, Alexandra Paul and Hari Shroff for critical reading of the manuscript, and Anke Kaltbeitzel for the use of the laser scanning confocal microscope.

3.7 Supplemental Information

Automated cell segmentation in FIJI® using a single nuclear dye (DRAQ5)

Mischa Schwendy[1,*], Ronald E. Unger[2], Mischa Bonn[1], Sapun H. Parekh[1,*]

[1] Max Planck Institute for Polymer Research, Ackermannweg 10, 55128 Mainz, Germany

[2] Institute of Pathology, Universitätsmedizin-Mainz, Langenbeckstraße 1, 55131 Mainz, Germany

[*] corresponding authors: schwendym@mpip-mainz.mpg.de, parekh@mpip-mainz.mpg.de

Geometric features

Circularity – a measure of small cell protrusions

The circularity parameter relates the area of a detected object to its perimeter.

$$Circ = 4 \cdot \frac{Area}{(Perimeter)^2}$$

If the object has a perfectly circular shape, i.e., possesses the largest possible ratio of area to perimeter, the circularity parameter equals 1. From that state, it is possible to create an object with an increased perimeter while its area stays constant, but not vice versa. Thus, it follows that circularity will approach 0 with increasing perimeter in the denominator.

A cell will have lower circularity values when its silhouette is more variegated (see **Figure S1**). Lower circularity can be observed with several phenotypes including one-dimensional elongation, the formation of pseudopodia or with the apparent surface roughness formed by lamellipodiae. Therefore, one should not rely on circularity as a single descriptor.

Aspect ratio – a measure for cell elongation

If the goal in an experiment is to probe the elongation of cells, the best marker is the aspect ratio as it relates the length of the major axis to the length of the minor axis of an ellipse that is fitted to the object. High values in this parameter are directly linked to a high degree of elongation.

$$AR = \frac{\text{major axis}}{\text{minor axis}}$$

Unfortunately, pitfalls arise for curved cells or cells with multiple protrusions.

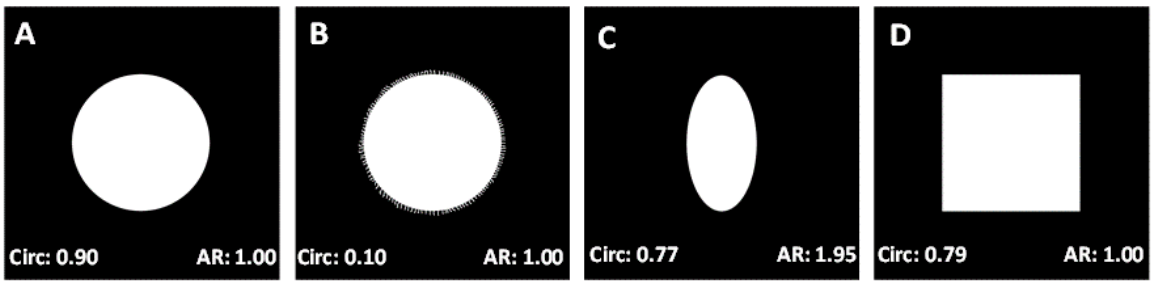

Figure S1. Circularity (Circ) and aspect ratio (AR) of different geometric objects.

a) perfect circle with a circularity of 0.90 (in theory 1.00, but decreased because pixelation creates a finite amount of surface roughness around a curve) and aspect ratio of 1.00. **b)** circle with high surface roughness, and an extended perimeter leading to a circularity of 0.10, but leaving AR unchanged. **c)** Elongated ellipse, with circularity of 0.77 and an aspect ratio of 1.95. **d)** A square object with circularity of 0.79 and aspect ratio of 1, because the ellipse fit leads to the assumption of a circle.

Taken together, along with the projected cell area and perimeter, these quantities provide a basic toolbox for quantitative cell shape description.

Image processing steps applied in the published algorithm

Our cell detection algorithm makes use of several built-in FIJI processing functions that are briefly explained in the following list.

Rolling ball background subtraction is a process to reduce background signals in an image. It assumes that a grayscale image is a 3D surface with the intensity values corresponding to the topography. A ball "rolls" over this landscape, averaging the values within its radius and subtracting the average value from the raw value of the central pixel in the ball in original image.

Gaussian blurring is a method to smooth an image. A user defines the size of a zone over which a Gaussian function is convolved with the image intensities. From this, one obtains a spatially smoothed image with Gaussian weighted averaging from neighboring pixels in the original image over a size scale given by the standard deviation.

Intensity coercion via a constrained maximum serves to put a ceiling on the maximum value for intensities in an image.

The watershed algorithm contained in the "Find maxima…" function with output "Segmented Particles" is a tool to separate touching objects. It functions by considering the intensities as topography where valleys (or basins) are flooded with water to detect "watershed" lines between the hills. These lines correspond to the regions where two objects are touching, thereby offering the possibility to split them into individual objects. Importantly, the noise value must be chosen appropriately, in this case below the values for local maxima, to avoid over-segmentation as explained previously by Meyer and Beucher[90]. The watershedding used here is applied to grayscale images.

Macro code

```
//settings
//This code works best with Leica image files (.lif); adjust code for other file formats
f = "[Cell_summaries]"; //title of the produced
x = 1; //nucleus channel
y = 2; //brightfield channel
input = "C:\\path\\to\\input\\file.lif"; //input file
output = "C:\\path\\to\\output\\directory\\"; // output directory
cellradius = 100; //maximum expected cell radius in µm
seriesnum = 13; //Number of series in the leica image file
```

```
//Start of procedure
for (j = 1; j <= seriesnum; j++){
	run("Close All"); //previously opened images are closed to avoid mislead processing of old images with same names

	//Create table to save results
	run("New... ", "name="+f+" type=Table");
	print(f,"\\Headings:Cell\tarea\tCirc\tAR\tRoundness\tMaximum");

	//Importing images using Bio-Formats Importer
	run("Bio-Formats Importer", "open="+input+" autoscale color_mode=Default split_channels view=[Standard ImageJ] stack_order=Default series_"+j+"");
	name = getTitle();
	prefix = substring (name, 0, lastIndexOf(name," "));
	run("Clear Results");

	//producing duplicates
	selectWindow(""+prefix+" C="+x+"");//Nucleus channel
		run("Z Project...", "projection=[Standard Deviation]");//picture for frame detection
		run("8-bit");
		run("Duplicate...", "title=IMAGE");//frame
		run("Duplicate...", "title=SUBTRACT");//Background subtraction mask (for frame and watershed)
		getPixelSize(unit, pixelWidth, pixelHeight);

	//create subtraction mask, applying constraining maximum (step I)
	selectWindow("SUBTRACT");
		getVoxelSize(w, h, d, unit);
		getStatistics(area, mean, min, max, std);
    row = nResults;
		setResult("Max ", row, max);
		u=floor(mean*3);
		run("Max...","value=u"); //constraining maximum of 3-fold mean to reduce effect of extreme values during subtraction
```

```
		//gaussian blurring (step II)
		run("Gaussian Blur...", "sigma=100 scaled"); //blurring for subtraction mask


	//subtract subtraction mask from image (step III)
	selectWindow("IMAGE");
		pxrollrad = cellradius/pixelWidth; //rolling ball radius in pixels needed (= predefined cell radius[µm]/pixelsize[µm/px])
		run("Subtract Background...", "rolling="+pxrollrad+"");
		run("Gaussian Blur...", "sigma=2.5 scaled");//reduces punctate character of grayscale image
		imageCalculator("SUBTRACT create", "IMAGE","SUBTRACT");
	selectWindow("Result of IMAGE");
		run("Duplicate...", "title=AND");//watershed
		run("Duplicate...", "title=CHECK");//for checking if maxima exist within selection later


	//Apply threshold to get binary image of cell borders (step IV)
	selectWindow("Result of IMAGE");
		run("Threshold...");
		setThreshold(1,256);
		setOption("BlackBackground", true);
		run("Convert to Mask", "method=Default background=Dark only black");
		run("Fill Holes");


	//Create watershed line image (step V)
	selectWindow("AND");
		run("Gaussian Blur...", "sigma=2 scaled");
		getVoxelSize(w, h, d, unit);
		getStatistics(area, mean, min, max, std);
  row = nResults;
		setResult("Max ", row, max);
		nBins = 256;
		getHistogram(values, count, nBins);
```

```
		//mean gray value of pixels belonging to cells needed (i.e. mean of ONLY non-zero pixel)
		Sum = 0;//all counts
		CV = 0; //weighed counts (= counts * intensity)
		for (i = 1; i<count.length; i++){ //starting with 1 instead of 0. -> 0 intensity values are not considered.
		  Sum += count[i];
		  CV += count[i]*i;
		}
		m = (CV/Sum);
		floor(m);
		l = floor(2*m); //Maxima need to be at least twice the intensity of cellular mean intensity
		run("Find Maxima...", "noise=l output=[Segmented Particles] exclude");//watershedding

	//Combine watershed lines and cell frame (step VI)
	selectWindow("Result of IMAGE");
		imageCalculator("AND create", "Result of IMAGE","AND Segmented");

	//select single cells with a spread area > 200 µm (step VII)
		run("Analyze Particles...", "size=200.00-Infinity circularity=0.1-1.00 add exclude"); //Cell bodies detected

	//Closing windows
	selectWindow("AND");
		run("Close");
	selectWindow("IMAGE");
		run("Close");
	selectWindow("Result of IMAGE");
		run("Close");
	selectWindow("AND Segmented");
		run("Close");
	selectWindow("SUBTRACT");
		run("Close");
```

```
selectWindow("Result of Result of IMAGE");
        run("Close");


//OPTIONAL: Check for nuclei within detected cell borders.
//1/5 of global maximum intensity (corresponding to most intensively stained nucleus) is taken as minimum value to be present in each detected cell frame.
selectWindow("CHECK");
        getVoxelSize(w, h, d, unit);
        getStatistics(area, mean, min, max, std);
  row = nResults;
        setResult("Max ", row, max);
        maxicheck = floor(max/5); //change for different minimum value
        maxtrack = 0; //tracks occasions of cell frames without minimum intensity. Necessary to delete the right frames
        roiManager("Multi Measure");
ROInumber = roiManager("count");
for(i = 1; i < ROInumber+1; i++){
        cellarea = 0;
        cellIntDen = 0;
        circularity = 0;
        Aratio = 0;
        Roundness = 0;
        for (a=0; a<nResults(); a++) {
        cellarea = getResult("Area"+i+"",a);
        circularity = getResult("Circ."+i+"",a);
        Aratio = getResult("AR"+i+"",a);
        Roundness = getResult("Round"+i+"",a);
        Maxvalue = getResult("Max"+i+"",a);
        }

        if(Maxvalue > maxicheck){
                selectWindow("Cell_summaries");

print(f,i+"\t"+cellarea+"\t"+circularity+"\t"+Aratio+"\t"+Roundness+"\t"+Maxvalue);
```

```
		}
		else if (Maxvalue < maxicheck){
			maxtrack = maxtrack+1;
			roiManager("select", i-maxtrack); //selects the roi without maximum
			roiManager("Delete"); //deletes the roi without maximum
		}
	}


	//save results and images (raw brightfield and cellframe overlays)
	selectWindow("Cell_summaries");
	saveAs("Text", ""+output+"\\"+prefix+".xls");
	selectWindow(""+prefix+" C="+y+"");
	run("Z Project...", "projection=[Sum Slices]");
	roiManager("Show All without labels");
	roiManager("Set Color", "red");
	roiManager("Set Line Width", 4);
	saveAs("Tiff", ""+output+"\\"+prefix+"_OV.tif");
	roiManager("Show None");
	saveAs("Tiff", ""+output+"\\"+prefix+".tif");
	run("Close All");
	selectWindow("Cell_summaries");
	run("Close");
	run("Clear Results");
	ROInumber = roiManager("count");
	if(ROInumber>0){
	roiManager("Delete");
	}
}
```

4 Intracellular lipid accumulation in THP-1 derived macrophages is substrate stiffness dependent

In preparation.

Mischa Schwendy[1,*], Ravi Dhiman, Ronald E. Unger[2], Mischa Bonn[1], Sapun H. Parekh[1,*]

[1] Max Planck Institute for Polymer Research, Ackermannweg 10, 55128 Mainz, Germany

[2] Institute of Pathology, Universitätsmedizin-Mainz, Langenbeckstraße 1, 55131 Mainz, Germany

[*] corresponding authors: schwendym@mpip-mainz.mpg.de, parekh@mpip-mainz.mpg.de

4.1 Abstract

During atherosclerotic plaque formation, the arterial wall is subject to remodeling processes that lead to a modification of the local microenvironment, including the extracellular matrix composition and mechanics. Mechanical properties such as stiffness of the surrounding environment can influence cellular phenotypes via mechanotransduction, leading to altered cell behavior depending on the cell's physical environment. Using quantitative confocal microscopy, we identify substrate stiffness as a key player in regulating aggregated low-density lipoprotein (agLDL) accumulation by macrophages. As an indication of foam cell formation, we quantify intracellular lipid volumes of THP-1 derived macrophages. To analyze effects of substrate stiffness on the foam cell subpopulation, we culture cells on polyacrylamide hydrogels and glass. Young's moduli of hydrogel substrates range from 4 to 50 kPa, and glass with a Young's modulus in the GPa range serves as unnaturally stiff substrate. Cellular lipid volumes increased more than 50 % with increasing stiffness and the percentage of foam cells increased over 3-fold. Inhibition of actin polymerization with latrunculin A resulted in a disappearance of the stiffness-dependence while inhibition of microtubule polymerization did not affect the stiffness-mediated trend. We observe, with increasing stiffness, a correlation between substrate-dependent increased lipid accumulation, and the increased expression of two receptors for agLDL. Consistent with substrate-dependent increased lipid accumulation, two receptors for agLDL also showed increased expression with increasing stiffness. Therefore, it appears that the stiffness-dependent agLDL uptake is mediated by actin polymerization and agLDL receptor expression.

4.2 Introduction

Macrophages are one of the key components in atherosclerotic plaque development, the underlying reason for ischemic heart disease. Attracted by retained low-density lipoprotein (LDL) that is rendered proinflammatory in the arterial wall, monocytes in the blood stream adhere to the endothelium and migrate into the tunica intima where they differentiate into macrophages and start clearing the tissue of LDL[28,34,120]. The ingestion of lipid rich particles leads to the formation of foam cells, macrophages with lipid droplet-filled cytosols[28,34,120]. Over the course of decades an atherosclerotic plaque consisting of lipids, necrotic and living cells, as well as a remodeled extracellular matrix is formed[32,121]. Numerous studies have analyzed lipid uptake and efflux in macrophages[122–124], as this happens during the early stage of atherosclerosis and understanding how to prevent lipid uptake could alleviate downstream pathogenic effects.

Concurrent with the long-term development of atherosclerosis, the arterial wall, particularly the *tunica intima*, has been shown to exhibit changes in mechanical properties[32,121,125,126]. Notably, Tracqui *et al*.[32] measured elastic moduli in various regions of atherosclerotic plaques via atomic force microscopy, reporting values ranging from 5.5 kPa in lipid-rich regions to almost 60 kPa in fibrous caps. Such strong mechanical variances can impact cellular behavior drastically, as substrate stiffness has been shown to guide cellular shape, migration behavior, as well as differentiation[19,77,127–130]. The sensitivity of macrophages to the extracellular matrix has been seen previously with reports showing preferred adhesion to stiffer substrates[131] and polarizability using micropatterning[20]. However, to the best of our knowledge, the effect of tissue stiffness on cytosolic lipid volumes in macrophages has not been previously investigated, despite its relevance for atherosclerosis.

Here, we analyze the lipid accumulation behavior of THP-1 derived macrophages *in vitro* on hydrogel substrates simulating native stiffness regimes between 4 kPa and 50 kPa by incubation with aggregated LDL (agLDL). Using quantitative fluorescent microscopic imaging, we quantified intracellular lipid volumes on a single-cell basis and defined an intracellular lipid volume threshold to characterize foam cell subpopulations within our measurements. We found an increasing foam cell fraction with increasing substrate stiffness. Suppression of microtubule assembly did not affect lipid uptake in the native stiffness regime (4-50 kPa) though it caused a reduction in lipid uptake on glass substrates. In contrast, lipid uptake was drastically reduced, and no longer stiffness-dependent, upon preventing actin polymerization. Flow cytometry analysis of LDL receptors scavenger receptor A (SR-A) and CD36 showed up-regulation on stiffer substrates, suggesting a possible mechanism underlying the increased macrophage lipid uptake on stiffer substrates.

4.3 Methods

LDL aggregation

Human LDL (LeeBio) was aggregated (agLDL) by vortexing. In this approach, 1 mg/mL LDL in phosphate buffered saline (PBS) was vortexed at maximum speed for 30 seconds at room temperature using a vortex mixer (Bender & Hobein AG, model K-550-GE) as done previously[74]. The resulting turbid solution was diluted in medium to 100 µg/mL and used for experiments. The LDL stock solution was kept at -80 °C, a single batch was used throughout the study.

Cell culture

THP-1 (DSMZ no: ACC 16) cells were differentiated and cultured at a density of 3×10^4 cells/cm^2 in RPMI 1640 medium (Sigma) supplemented with 10 % fetal calf serum (FCS)(Gibco) and 10 U/mL Penicillin/Streptomycin (Gibco) at 37 °C and 90 % relative humidity. For differentiation, 100 ng/mL phorbol-12-myristate-13 acetate (PMA)(Sigma) was added to the culture medium for 48 hours, as done previously[72]. Cells were kept in a recovery phase in culture medium with 1 % FCS (low-serum state) for 24 hours after initiation of differentiation. Reduced FCS in the recovery phase was to minimize lipid content in the culture medium prior to agLDL addition. To assess cellular lipid uptake, cells were cultured in a low-serum state medium supplemented with 100 µg/mL agLDL with the medium being refreshed every three days.

For analysis of substrate stiffness-mediated effects on cellular lipid accumulation, THP-1 cells were differentiated and cultured on collagen-coated polyacrylamide hydrogels in 96 well plates or Petri dishes (Softwell & PetriSoft dishes, Matrigen). Hydrogels exhibited varying stiffness ranging from 4 to 50 kPa and a glass substrate well in the several GPa range (an approximated value of 50 GPa is used throughout this publication; higher values have been reported[132]). To inhibit different parts of the cytoskeleton, different small molecule inhibitors were added into the agLDL-supplemented medium. For microtubule polymerization, colchicine (Sigma) was added to the culture medium at 10 mM. Disruption of filamentous actin was achieved by adding 1 mM of latrunculin A (Sigma) to the culture medium.

Cell staining

Prior to staining, cells were fixed with 4 % para-formaldehyde in PBS for 10 min and then washed three times with PBS. Nuclei and lipid droplets were stained by incubation with 5 µM DRAQ5 (Thermo Fisher Scientific) and 1 µg/mL BODIPY 493/503 (Thermo Fisher Scientific) in

PBS for 40 mins, respectively. Unbound stains were washed by rinsing samples three times with PBS. Samples were kept hydrated by PBS during imaging.

Image acquisition

Confocal imaging was performed on a laser scanning TCS SP5 II microscope (Leica Microsystems) equipped with HeNe and Argon lasers. The excitation wavelengths were 632.8 nm and 488.0 nm for DRAQ5 and BODIPY, respectively. Images were collected, using a 25X, 0.95 NA water immersion objective (Leica), with emission detection from 506 – 534 nm for BODIPY fluorescence and 685 – 751 nm for DRAQ5 fluorescence. Detector gains were adjusted to minimize signal saturation within nuclei (DRAQ5) and lipid droplets (BODIPY) for cells cultured on glass substrates and settings were kept constant throughout measurements of cells on hydrogels (acquiring images through hydrogels). Volumetric stacks were acquired with Z-steps of 1.51 µm and X-Y spacing of 0.6 µm per pixel. Scanner speed was set to 400 Hz.

Image processing

Images were processed in FIJI (is just ImageJ) using an algorithm described in Chapter 3 to segment and quantify cell geometry. Briefly, collected DRAQ5 image planes were projected into one image according to pixel wise standard deviation in Z-direction and a blurred copy was subtracted to reduce background signals. Cellular outlines were detected via thresholding, touching cells split by watershedding. Lipid signals were binarized in a two-step process: First, for background removal, a maximum Z-projection of the full Z-stack was blurred with a gaussian filter (sigma = 3 µm) and subtracted from each individual slice in the Z-stack. Secondly, a threshold (value = 1) was used to produce a binary mask of the residual lipid signals in each slice. Cell frames generated from the DRAQ5 signals were cast onto the thresholded version of the lipid signal Z-stack and signal area per cell detected in 3D by scanning each image slice in the stack. Volumetric lipid values were computed by multiplying the detected lipid signal areas (from each image in the stack) with the step size used during image acquisition (step size was selected sufficiently large to prevent signal overlap in Z-direction).

Flow Cytometry

For flow cytometry analyses, differentiated THP-1 cells were cultured in 35 mm glass bottom dishes (MatTek) and collagen-coated PetriSoft dishes (Matrigen) of varying stiffness (4, 25, and 50 kPa) following the same protocol outlined above. At the end of the incubation period, cells were harvested by adding 1 mM EDTA at 37°C for 15-20 min, followed by gentle scraping with a cell scraper. 3 x 10^5 harvested cells were washed twice with PBS and incubated with two monoclonal antibodies (mAb) directed against class A macrophage scavenger receptor (SR-A) with a fused AlexaFluor-647 fluorophore (sc-166184, mouse anti-human, Santa Cruz Biotechnology), and against CD36 with a fused phycoerythrin fluorophore (1P-451-T025, Mouse anti-human, Exbio). Anti-SRA antibodies were applied at a concentration of 0.3 µg/100 µL cell suspension, and 6 µL of anti-CD36 antibody solution was added (accounting for 3 x 10^5 cells) with a subsequent incubation for 30 min at 4°C. Following incubation, cells were washed twice with PBS and resuspended in 500 µl ice-cold PBS. The SR-A expression was measured using the AttuneTM NxT acoustic focusing cytometer (Thermofisher Scientific). At least 10,000 cells were analyzed for each sample. Unstained cells were used as negative control. Data analysis was performed using the FCS Express v6 software (DeNovo software, USA). During analysis, a gate was applied on a forward/side scatter dot plot to exclude debris and cell clumps. The same gate setting was used throughout the experiment. Cells selected with this

gating strategy were analyzed for peak fluorescence and compiled in a histogram, which was used to determine median fluorescence intensity (MFI).

Statistical Analysis

Statistical significance of differences in cellular lipid uptake and cell spreading area of THP-1 derived macrophages was evaluated using analysis of variance (ANOVA) with post-hoc analysis based on Tukey's test using the software GraphPad Prism 8.0 (GraphPad Software). Statistical significance was expressed as *, **,*** and ****, indicating p-values < 0.05, 0.01, 0.001 and 0.0001, respectively.

4.4 Results

Intracellular lipid accumulation is substrate stiffness dependent

We analyzed cytosolic lipid volumes in THP-1 derived macrophages *in vitro* after incubation with agLDL by acquiring volumetric confocal image stacks with fluorescently stained lipids and nuclei. Using our algorithm for cell segmentation and lipid signal thresholding (as described in the Methods), we determined cytosolic lipid volumes and cell spreading area for individual cells cultured on substrates with increasing stiffness. While lipid accumulation after three days of agLDL incubation did not show a substrate stiffness-mediated effect, cellular lipid volumes increased with stiffness after five days. As shown in Figure 32, cellular lipid volumes after three days vary between 1100 and 1300 fL without exhibiting a trend over the scanned stiffness range (4 kPa – 50,000 kPa). However, cells incubated with agLDL for five days exhibited stiffness-mediated lipid accumulation with cellular lipid volumes increasing more than 50 % from the softest condition to the glass substrate (**Figure 32a and b**).

In addition to lipid accumulation, we quantified projected cell area after both three and five days. Similar to cytosolic lipid volumes, after three days of incubation with agLDL, projected cell area was not substrate stiffness dependent. Again, similar to lipid uptake, projected cell area after five days of incubation with agLDL increased with substrate stiffness although in a less prominent way (see **Figure 32c**). To estimate the effect of substrate stiffness on lipid accumulation in a cell area independent manner, we analyzed the lipid volume to cell area ratio after five days of agLDL incubation and observed a more than 22 % increase from 4 kPa to glass (see **Figure 32d**). This suggested that increased intracellular lipid volumes on stiffer substrates was not solely mediated by increased cell spreading.

Defining and monitoring a foam cell phenotype during hydrogel culture

While averaged lipid volume per cell (**Figure 32a**) is one quantification of how substrate stiffness affects cytosolic lipid volumes in macrophages, a perhaps more relevant metric is to analyze the distribution of lipid volume in terms of cell sub-populations (**Figure 33a**). To the best of our knowledge, no quantitative measure for a foam cell phenotype has been proposed based on cellular lipid volumes. To define a cellular lipid volume that is characteristic for foam cells, we chose the 90th percentile value of cellular lipid volumes observed in THP-1 derived macrophages incubated with agLDL for five days on 4 kPa hydrogels. This stiffness value was regarded as closely resembling native mechanical regimes, since it was the closest to 5.5 kPa reported for lipid-rich regions in atherosclerotic plaques[32]. With these criteria, a value of 2463 fL was chosen as the threshold to characterize lipid-laden cells as "foam cells". The scatter plot shown in **Figure 33a** shows cells containing lipid volumes below the threshold as black points and above the threshold (i.e. foam cells) as red points. Our results showed that the foam cell

subpopulation steadily grew in proportion to the total cell population with increasing substrate stiffness after five days of agLDL incubation while it stayed almost constant after three days of agLDL incubation (data not shown). As shown in **Figure 33a**, the fraction of foam cells increases more than three-fold, comparing cells cultured on glass to cells cultured on 4 kPa after five days of agLDL incubation.

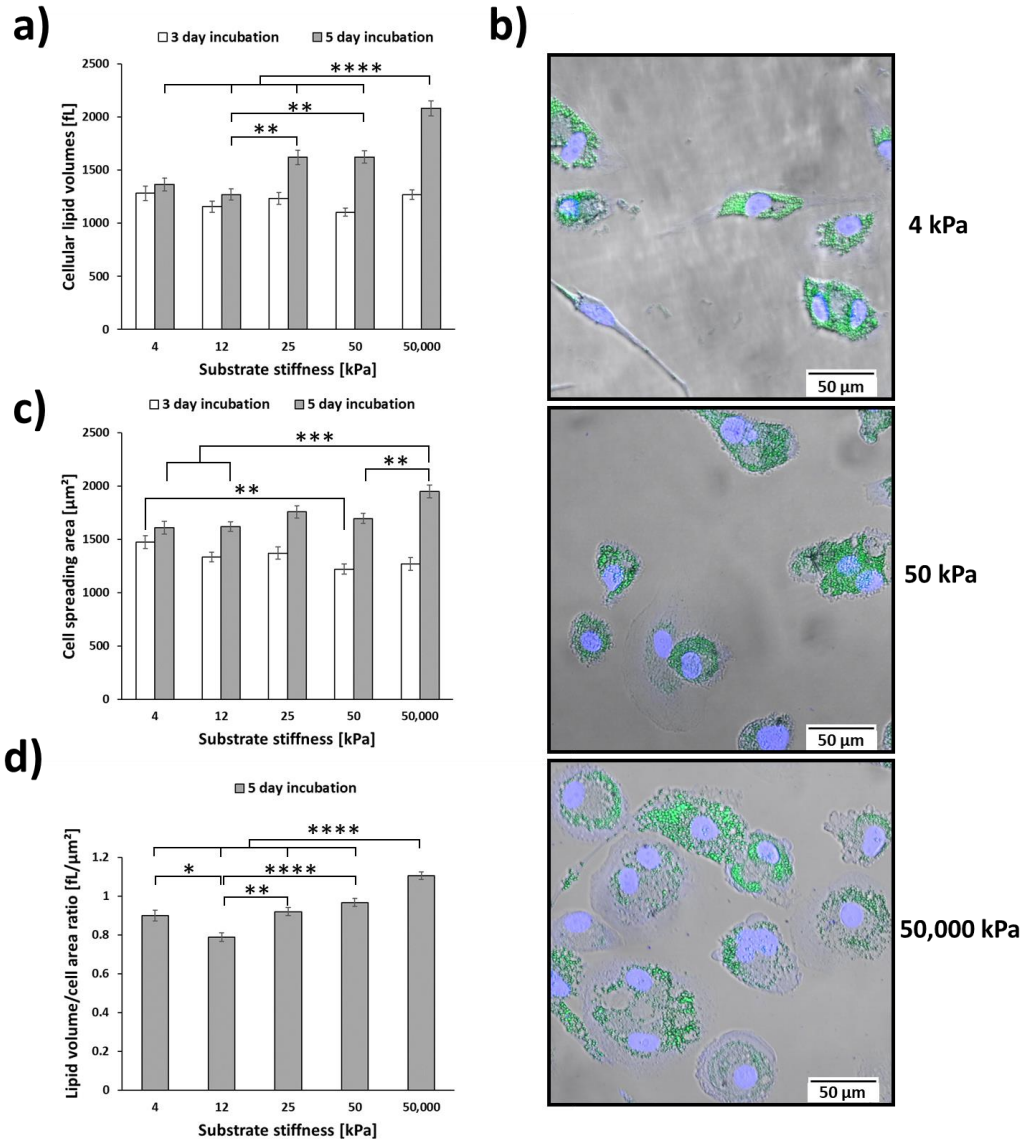

Figure 32 Intracellular lipid accumulation by THP-1 derived macrophages incubated with 100 µg/mL aggregated LDL is substrate stiffness dependent.

(a) Cellular lipid volumes remain independent of substrate stiffness after three days of incubation with aggregated LDL (white bars), but show increased lipid accumulation with increasing substrate elastic modulus after five days of agLDL incubation (gray bars). At least 240 cells per culture condition were analyzed in n > 3 experiments. (b) Exemplary images of cytosolic lipid droplet formation in cells cultured on substrates of varying stiffness (elastic modulus indicated) after five days of agLDL incubation (Z-projected confocal images: green = BODIPY stained lipids; blue = DRAQ5 stained nuclei; gray = transmitted laser light). (c) Cell spreading area decreases with increasing substrate stiffness after three days of agLDL incubation, but increases with increasing substrate stiffness after 5 days. (d) Lipid volume to cell area ratio after five days of agLDL incubation. The ratio increases by 22.8 % from the softest culture substrate to glass. Data compiled from at least 240 cells per culture condition in n ≥ 3 independent experiments. Where applied, error bars indicate standard error of mean. Analysis of variance with post-hoc Tukey's test was applied to determine significance. **, ***, and **** indicating P-values ≤ 0.01, 0.001, and 0.0001, respectively.

Lipid uptake depends on actin- and microtubule-polymerization

The intracellular lipid volume increases more rapidly with the substrate stiffness than does the cell spreading area. This raises the question regarding the pathway underlying the stiffness-dependent lipid uptake process, since cell area seems to play a minor role. As mechanical stimuli are mainly transduced by the cytoskeleton[130], we tested the roles of different cytoskeletal components in substrate stiffness dependent lipid uptake.

Polymerization of actin and microtubules was inhibited using latrunculin A and colchicine, respectively. According to our previous analysis of lipid accumulation, where a stiffness-dependent trend was seen only after five days (without cytoskeletal inhibition), we quantified cellular lipid volumes after five days of agLDL incubation with inhibitors in the medium and monitored the fraction of foam cells. Inhibiting actin polymerization resulted in a stark decrease of the foam cell subpopulation and an abrogated stiffness-mediated lipid uptake (see **Figure 33b**). Interestingly, inhibiting microtubule polymerization still resulted in increasing foam cell subpopulations with increasing substrate stiffness, but the fraction of foam cells appeared to plateau at 50 kPa as the foam cell population only marginally increased when cells were cultured on collagen-coated glass substrates.

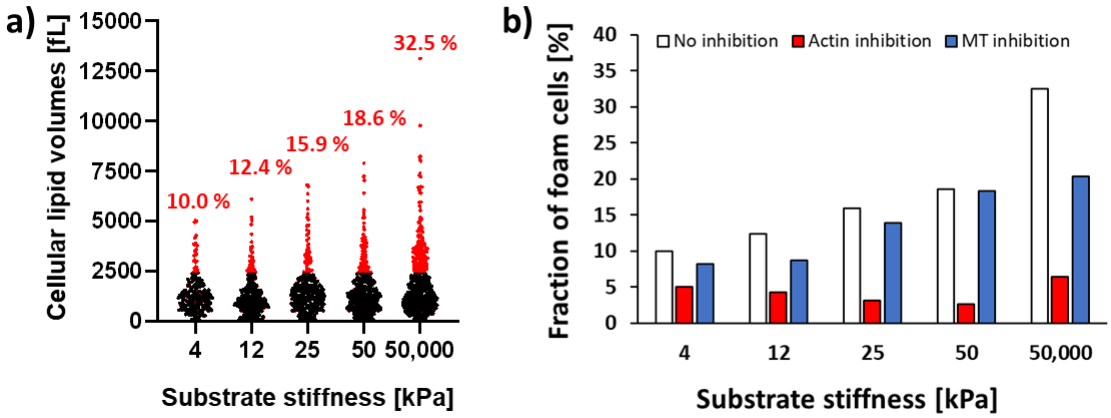

Figure 33 Foam cell subpopulations

a) Scatter plot of cellular lipid volumes with black datapoints corresponding to cells with lipid volumes below the defined foam cell threshold and red datapoints corresponding to cells with lipid volumes exceeding the threshold. The foam cell subpopulation increases more than threefold from 4 kPa to 50 GPa. b) Effect of cytoskeletal inhibition on foam cell formation. Inhibition of microtubule (MT) assembly (blue) does not change the substrate stiffness dependent trend of foam cell formation from 4 to 50 kPa, but rather reduces the foam cell subpopulation of macrophages cultured on glass by more than 35 %. Inhibition of actin polymerization (red) decreases the foam cell subpopulation below 7 %, independent of substrate stiffness. No error bar calculation possible, as *all* experiments per culture condition were pooled and the foam cell subpopulation calculated within all measured cells.

The decreased tendency to form foam cells during cytoskeletal inhibition indicates a role of mechanotransduction in cellular lipid uptake. To further assess entry mechanisms affected by the hydrogel culture, we analyzed changes in the expression of two common LDL-receptors.

Flow cytometry reveals SR-A as driving receptor of stiffness mediated lipid uptake

As agLDL is endocytosed mainly via CD36 and SR-A[33,44], we used flow cytometry to assess if the expression level of either receptor exhibited a stiffness dependent regulation. For these

experiments, THP-1 derived macrophages were cultured on variable-stiffness hydrogel-coated Petri dishes with 100 µg/mL agLDL for three days. We chose to use three days of culture for this experiment to maximize the number of cells for flow cytometry analysis.

To quantify CD36 and SR-A expression, antibody staining and flow cytometry was performed as outlined in the Methods section. For internal standardization, the median fluorescence intensity (MFI) values of the stained samples obtained were divided by the MFI value obtained from an unstained sample. As shown in **Figure 34**, we observed steadily increasing SR-A MFI with increasing substrate stiffness, which demonstrates that SR-A expression increased per cell with increasing stiffness. On the other hand, CD36 expression levels exhibited low MFI values at 4 kPa and increased immediately by 3 – 4-fold for substrate stiffness above 25 kPa. No clear trend was observed for CD36 expression with stiffness above 25kPa, unlike for SR-A.

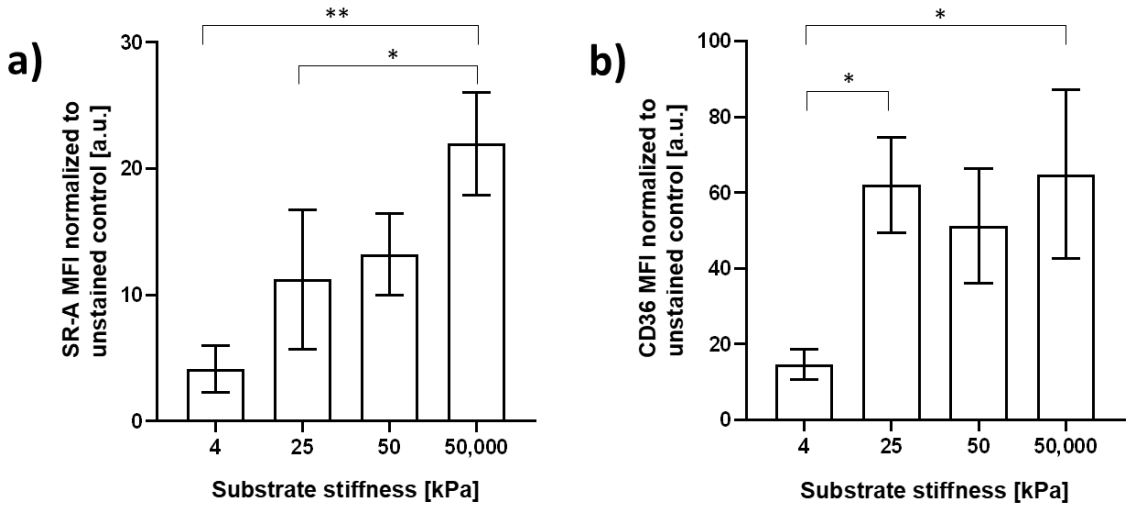

Figure 34 Expression of SR-A and CD36 on THP-1 derived macrophages cultured on substrates of varying elastic modulus and incubated with 100 µg/mL agLDL.
Median fluorescence intensity (MFI) of SR-A (a) increases steadily from 4 kPa to 50,000 kPa indicating a stiffness-dependent upregulation of the receptor. MFI of CD36 (b) shows low values during cultivation of cells on hydrogels of 4 kPa, and 3-4 fold higher values at 25 kPa and above, indicating lower expression only on very soft substrates and constant expression on stiffer substrates. Data retrieved from 3 independent experiments, with error bars indicating standard deviation. Analysis of variance with post-hoc Tukey's test was applied to determine significance. *,** indicating P-values ≤ 0.05 and 0.01, respectively.

4.5 Discussion

In this work, we provided evidence for a substrate stiffness-mediated influence on lipid accumulation in THP-1 derived macrophages. In our experiments, we incubated cells cultured on hydrogels of varying elastic modulus with 100 µg/mL aggregated LDL for three and five days. While we found constant cellular lipid volumes after three days, lipid uptake was augmented on stiffer substrates compared to softer substrates after five days.

The stiffness-dependent lipid accumulation was not solely due to extended membrane surfaces caused by increased cell spreading on stiffer substrates. Using the entire population of lipid-laden cells, we determined a criterion for foam cells based on the lipid volume and cell area, which could be applied to evaluate the effect of cytoskeletal inhibition on lipid accumulation. Foam cell formation on hydrogels during cytoskeleton inhibition (by latrunculin A) revealed a dependency of the stiffness-mediated lipid uptake on intact actin filaments. This result is in good accordance with the prominent role of actin in agLDL uptake reported

previously [42,44,133]. Active actin polymerization seems to be of foremost importance in lipid uptake mechanisms[44], thereby its inhibition generally blocks entry routes for cholesterol and prevents macrophages from becoming foam cells. Additionally, we observed a stark decrease in foam cell formation of THP-1 derived macrophages cultured on glass substrates under microtubule inhibiting conditions. A decreased intracellular cholesterol accumulation due to inhibition of microtubule-dependent macropinocytosis has been previously observed[134]. Importantly, inhibiting microtubule polymerization did not change the stiffness-mediated lipid accumulation, but rather only reduced foam cell formation on glass, an unnaturally stiff substrate. Thus, foam cell formation is partially dependent on microtubule assembly when the cells are cultured on excessively stiff substrates (which might be relevant in the calcification processes happening during atherosclerosis[135]), but not on substrates that mimic the native tissue mechanics. This finding suggests that microtubules do not play an active role in regulating lipid accumulation in macrophages under native conditions. To investigate a possible mechanism for increased foam cell formation, we quantified the two prominent LDL uptake receptors, scavenger receptor A (SR-A) and CD36, after three days of agLDL incubation. Receptor expression and lipid accumulation is schematically summarized in **Figure 35:** While we found a steadily increasing expression of SR-A with increasing substrate stiffness, we observed low expression of CD36 in cells cultured on 4 kPa substrates that jumped to a higher expression level with almost constant values on substrates stiffer than 25 kPa. The tendency of macrophages to produce additional lipid uptake receptors on stiffer substrates is consistent with increased foam cell formation on substrates with increasing elastic modulus. A more comprehensive analysis of all LDL receptor expression would help disentangle different lipid uptake mechanisms affected by substrate stiffness versus those that are not.

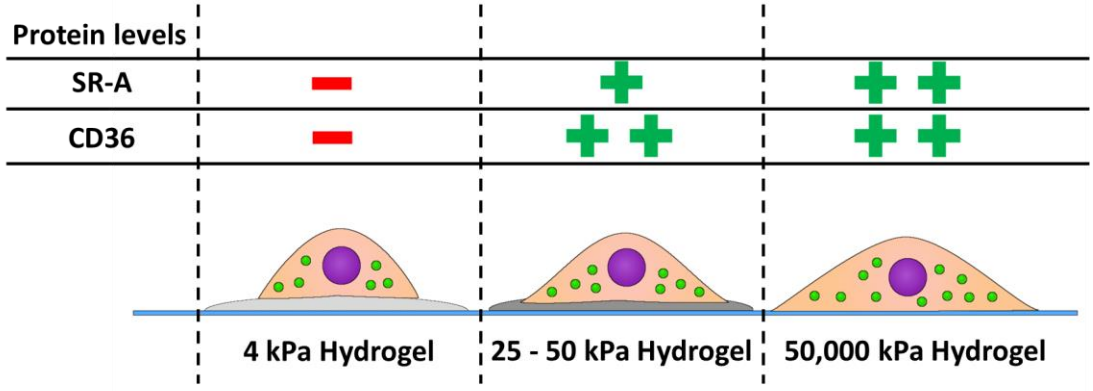

Figure 35 Effects of substrate stiffness on foam cell formation after five days of agLDL incubation.

Intracellularly stored lipids lead to excessive lipid droplet (green vesicles) formation with increasing substrate stiffness. Increased cell spreading was observed on stiffer substrates. Protein expression levels indicated for SR-A and CD36 show a stiffness dependent expression rate of the two LDL receptors.

4.6 Conclusion

In this work, we showed that macrophages are sensitive to their mechanical environment in that they show a substrate stiffness-sensitive lipid accumulation. This trend could have a strong influence on atherosclerotic plaque progression, as matrix remodeling to prevent plaque rupture could, in turn, lead to amplified cellular lipid uptake. We showed that the

cytoskeletal filamentous actin and microtubules both affect cellular lipid volumes with filamentous actin being critical for stiffness-dependent foam cell formation. Additionally, we report a substrate stiffness-mediated increase in expression of the two LDL receptors SR-A and CD36. Overall, we suggest that the stiffness dependence results from the roles of actin-dependent, receptor-mediated lipid uptake and microtubule-dependent macropinocytosis. Further studies with other relevant forms of LDL (e.g. native and oxidized LDL) will be very useful to investigate if all relevant LDL species show similar stiffness-dependent increased uptake.

5 EVICAN – Expert visual cell annotation

In preparation.

Mischa Schwendy[1,*], Ronald E. Unger[2], Mischa Bonn[1], Sapun H. Parekh[1,*]

[1] Max Planck Institute for Polymer Research, Ackermannweg 10, 55128 Mainz, Germany

[2] Institute of Pathology, Universitätsmedizin-Mainz, Langenbeckstraße 1, 55131 Mainz, Germany

[*] corresponding authors: schwendym@mpip-mainz.mpg.de, parekh@mpip-mainz.mpg.de

5.1 Abstract

In this contribution we present a new dataset, comprising partially annotated images from more than 30 cell lines, multiple microscopes, various contrast mechanisms, and magnifications that is readily usable as training data in computer vision algorithms for potential applications in cell biology. Image heterogeneity was achieved by acquiring images on four separate microscopes and 9 different objectives. Image annotations, segmenting 30 different cell lines and their nuclei, were performed by cell culture experts using counter-stained fluorescent images. Our annotation format matches the popular COCO-format, making the dataset easily applicable to machine learning algorithms currently under development. With 4600 images and ~53,000 segmented instances, the breadth of this dataset is more than 6-fold larger than any publicly available comparable dataset. We provide two editions of the dataset: Expert visual cell annotation (EVICAN) 2 with a "nucleus" and "cell" class pooled across all cell lines and EVICAN 60 with nuclei and cells categorized for respective cell lines individually. Using a Mask-RCNN implementation to train a machine-learning assisted classification and segmentation algorithm with our EVICAN2 dataset, we showed a mean average precision of 58.3 % at intersection over union scores above 0.5. This precision value is comparable to current state-of-the-art every-day scene classification and segmentation algorithms. The dataset that we describe (and freely provide) is a great starting point to train future machine learning algorithms for cell biology applications.

5.2 Introduction

In recent years, microscopy has seen major advancements from the perspective of both automated acquisition and boosting optical performance in terms of spatial and temporal resolution. With the rise of automation in the industry: both in acquisition and analysis, turning microscopes into powerful high-content screening systems, researchers are now in need of rapid, accurate analysis algorithms to infer quantitative measures from the ever-increasing amount of imaging data. In the specific case of cell biology, image segmentation and classification is essential as it is the first step in any analysis for relating measured quantities such as cell shape or intensity of a fluorescent molecule within cells to specific treatments, thereby enabling single cell analysis.

Traditionally, these algorithms have been based on fluorescent staining of cells, where image contrast highlights specific compartments or molecules that can be visualized and processed in a straight-forward manner compared to the highly irregular appearance and non-specific contrast from cells in a brightfield (or phase contrast) image. While fluorescence staining is immensely powerful and convenient for cellular analysis and identification, it is nevertheless often associated with serious requirements such as the need for cell fixation and permeabilization, rendering it impossible to observe processes in live-cell experiments. Even if a dye does not require a sample preparation that comes along with cell death, it can introduce perturbations into the system that alter the experimental outcome.[136,137] Approaches to alleviate the need for cell staining utilized the bright halo forming around cells in defocused brightfield microscopy [99]. While at the time beneficial, the extra time needed for focusing (and defocusing), combined with the larger data space needed for saving additional images, makes the technique impractical for large-scale experiments. Additionally, the procedure requires technical adjustments during image acquisition (precise focusing/defocusing). While these technical adjustments can be programmed in high-

throughput experiments, it is an added challenge in manual image acquisition. The question of how to analyze: identify and segment unstained, in-focus, brightfield images of cells still remains unsolved.

A promising potential solution lies in using "big data" in conjunction with deep learning analyses. After breakthrough work by Krizhevsky *et al.* [60], who trained a deep convolutional neural network (CNN) to classify image content into 1000 different classes (e.g. "person", "car", or "dog"), CNNs have gained considerable attention for image analysis. Moreover, in recent years, CNNs have advanced beyond classifying image content to also localizing[61–63], and finally segmenting, objects within an image[64]. The new possibilities provided by CNNs have influenced a broad range of engineering and scientific fields, such as autonomous driving[138], face recognition[139], and cancer detection[140].

A major drawback of CNNs, however, is their need for massive amounts of annotated data. Krizhevsky trained his network on ~1.2 million class-labeled images from the ImageNet database[67]. The Common objects in context (COCO) dataset[68], a popular collection of images for training of segmentation algorithms, contains more than 330,000 images with more than 2.5 million labeled instances of 91 different classes. As extensive annotation is needed, these large datasets consisting of hundreds of thousands of images with even more instance segmentations are often a result of crowd-sourced work. While unproblematic for image annotations for objects known from everyday life, crowd sourcing is much less feasible for annotating datasets that require expert knowledge, as is the case in cell biology and medicine. To overcome this bottleneck in brightfield and phase contrast imaging, we assembled a collection of more than 4600 images of 30 cell lines, acquired on four separate microscopy setups in three different laboratories with nine different objectives having magnifications ranging from 10X – 40X. Cellular outlines and nuclei in our dataset were segmented manually by cell culture experts against fluorescently stained images. To our knowledge, we are the first group to offer a freely available, large-scale segmented dataset with several classes in the cell culture sector. With this new dataset, we hope to close a gap between cell biologists and computer scientists, as it provides access to biological data specifically prepared for training of computer vision algorithms. As a proof of principle, we also trained a segmentation and classification algorithm on our dataset and achieved an average precision of 58.3 % for intersection over union scores above 0.5.

5.3 Online methods

Cell culture

All cells were maintained at 37 °C, 95% relative humidity, and 10 U/mL Penicillin/Streptomycin (Gibco) added to the respective medium. A complete list of used cell lines together with media and indicated culture supplements fetal calf serum (FCS) and non-essential amino acids (NEAA) is given in **Table 7**. 24 hours before imaging, cells were seeded into 96 well plates (Cellstar, Gibco) at 30 %, 50 %, and 100 % confluency. After incubation, cells were fixed with 4 % para-formaldehyde in PBS for 10 minutes. Prior to imaging, cell membranes were stained with 0.01 % CellMask orange (Thermo Fisher Scientific) in PBS, nuclei were stained with 1 µg/mL DAPI (Thermo Fisher Scientific) in PBS for 20 min at 37 °C. Cells were subsequently washed with PBS three times.

Image acquisition

Image acquisition was performed on 4 different setups: Opera Phenix (Perkin Elmer), AF7000 (Leica), IX81 (Olympus) and Biorevo BZ-9000 (Keyence).

Table 5 summarizes the microscopy platforms as well as objectives used in this work.

Table 5 Microscopes and Objectives used for image acquisition

Microscope	Objective	Contrast mode
Opera Phenix (Perkin Elmer)	10X/0.3 (Air)	Brightfield
	20X/0.4 (Air)	
	40X/1.1 (Water)	
IX81 (Olympus)	10X/0.3 (Air)	Phase contrast
	20X/0.4 (Air)	
AF 7000 (Leica)	10X/0.3 (Air)	Phase contrast
	20X/0.4 (Air)	
Biorevo BZ-9000 (Keyence)	10X/0.3 (Air)	Phase contrast
	20X/0.45 (Air)	

Image annotation & dataset assembly

Brightfield or phase contrast microscopy images were merged with color-coded fluorescence images of the nucleus and membrane to facilitate recognition of nuclei and cell borders using FIJI®[93]. Cell culture experts and supervised personnel annotated 3 – 10 cells and nuclei within each image, and in total 52959 instances were segmented in the 4640 images. All annotations were exported as JavaScript Object Notation (JSON) document with IDs referring to the brightfield or phase contrast version of the original image, segmentations as x,y-polygons, and category-IDs indicating cellular entity or nucleus. Export format was chosen to fit COCO annotation style to ensure maximal applicability for modern machine learning training.

Computer Vision classifier training

Training our detection and segmentation algorithm was performed on a Mask-RCNN implementation, previously released under an MIT license by Matterport Inc.[88] In this implementation, the Mask-RCNN approach is executed using the open-source Tensorflow and Keras libraries. We used a modification of the training scheme published before by Johnson[141]. Briefly, a Resnet-101 feature pyramid network model with 101 layers organized in 5 stages was employed as the backbone; weights were initialized with pretrained weights on the COCO dataset; training was performed for 52 epochs (40x heads, 8x 4+ layers, 4x all layers). The learning rate for weight adjustment during training was set to an initial value of 0.001 at the start of heads, as well as 4+ layer training; This value was decreased by 50 % after 20 epochs for heads training and after 4 epochs for 4+ layer training, respectively. For end-to-end training

after epoch 48, we decreased the learning rate to 10 % the original value and after additional 2 epochs, decreased it to 5 % the original value.

All training steps were carried out on a desktop PC with an Intel Core i7-6700 CPU with four 3.4 GHz processors and 50 GB RAM for a full process duration of 31 days.

Classifier evaluation

Evaluation was performed on 100 fully annotated brightfield and phase contrast images that were kept separate from the training data. According to the image quality characteristics summarized in **Table 6**, we categorized each evaluation image into one of three difficulty classes.

Table 6 Quality characteristics of evaluation datasets

Evaluation dataset	**Cellular appearance (in phase contrast or brightfield)**	**Image quality, contrast mechanism**
Difficulty 1	2D cell growth, few cell-cell contacts, clear cell outlines, most nuclei visible	All cells in focus, most often phase contrast
Difficulty 2	2D cell growth, several cell-cell contacts, most cell outlines visible, few nuclei visible	Cells minimally defocused, mixed brightfield and phase contrast
Difficulty 3	Occasional 3D growth, many cell-cell contacts/colony formations, nuclei often invisible without staining	Frequently defocused, mainly brightfield images

The three resulting evaluation datasets are intended to assess the capabilities of trained classification-segmentation algorithms under varying imaging conditions. To guarantee accuracy of the ground truth masks, all annotations for quantitative comparison were generated on stained image versions.

Classification performance was evaluated according to precision:

$$\boldsymbol{Precision} = \frac{\boldsymbol{True\ Positives}}{\boldsymbol{True\ Positives} + \boldsymbol{False\ Positives}}$$

Predicted instances colocalized with corresponding ground truth instances were counted as true positives when exhibiting intersection over union (IoU) scores above a certain threshold. We monitored average precision at IoU thresholds above 0.5 ($AP_{0.5}$) and 0.75 ($AP_{0.75}$). Additionally, a cumulated average precision (AP) was computed, where the IoU threshold was incrementally increased from 50 – 95% in 5% steps and the precision per image averaged over each step.

Table 7 Cell lines represented in EVICAN dataset

No	Cell line	Species	Tissue	Type	Medium	FCS [% in medium]	NEAA added	Code
1	**Colo 320**	Human	Colon	Colon adenocarcinoma	RPMI	10	x	ACC 144 (DSMZ)
2	**SW-480**	Human	Colon	Colorectal adenocarcinoma	RPMI	10	x	CCL-228 (ATCC)
3	**HT-29**	Human	Colon	Colorectal adenocarcinoma	RPMI	10	x	HTB-38 (ATCC)
4	**Caco-2**	Human	Colon	Colorectal adenocarcinoma	EMEM	20	✔	HTB-37 (ATCC)
5	**DLD-1**	Human	Colon	Colorectal adenocarcinoma	RPMI	10	x	CCL-21 (ATCC)
6	**HCT116**	Human	Colon	Colorectal carcinoma	RPMI	10	x	CRL-247 (ATCC)
7	**RKO**	Human	Colon	Colon carcinoma	EMEM	20	✔	CRL-2577 (ATCC)
8	**T47D**	Human	Mammary gland	Ductal carcinoma	RPMI	10	x	HTB-133 (ATCC)
9	**SK-BR-3**	Human	Mammary gland (derived from pleural effusion)	Adenocarcinoma	RPMI	10	x	HTB-30 (ATCC)
10	**MDA-MB-231**	Human	Mammary gland (derived from pleural effusion)	Adenocarcinoma	RPMI	10	x	HTB-26 (ATCC)
11	**MCF-7**	Human	Mammary gland	Adenosarcoma	RPMI	10	x	HTB-22 (ATCC)
12	**786-O**	Human	Kidney	Renal cell adenocarcinoma	RPMI	10	x	CRL-1932 (ATCC)
13	**769p**	Human	Kidney	Renal cell adenocarcinoma	RPMI	10	x	CRL-1933 (ATCC)
14	**ACHN**	Human	Kidney	Renal cell adenocarcinoma	EMEM	20	✔	CRL-1611 (ATCC)
15	**CAKI-2**	Human	Kidney	Clear cell carcinoma	RPMI	10	x	HTB-47 (ATCC)
16	**PC-3**	Human	Prostate	Adenocarcinoma	50/50 RPMI/F12	10	x	CRL-1435(ATCC)
17	**LNCaP**	Human	Prostate	Carcinoma	RPMI	10	x	ACC 256 (DSMZ)
18	**DU-145**	Human	Prostate (derived from metastatic site in brain)	Carcinoma	RPMI	10	x	HTB-81 (ATCC)
19	**SH-SY5Y**	Human	Bone marrow neuroblastoma	Neuroblastoma	DMEM	20	x	CRL-2266 (ATCC)
20	**MG-63**	Human	Bone	Osteosarcoma	EMEM	20	✔	CRL-1427 (ATCC)
21	**HeLa**	Human	Cervix	Adenocarcinoma	DMEM	10	x	CCL-2 (ATCC)
22	**HT-1080**	Human	Connective tissue	fibrosarcoma	DMEM	10	x	CCL-121 (ATCC)
23	**NIH/3T3**	Mouse	Embryo	Fibroblast	DMEM	10	x	CRL-1658(ATCC)
24	**RAW 264.7**	Mouse	Ascites (Abelson murine leukemia virus-induced tumor)	Macrophage	DMEM	10	x	TIB-71 (ATCC)
25	**HEL 299**	Human	Lung	Fibroblast	DMEM	10	x	CCL-137 (ATCC)
26	**FaDu**	Human	Pharynx	Squamous cell carcinoma	DMEM	10	x	HTB-43 (ATCC)
27	**MCC26**	Human	Skin	Merkel carcinoma from skin	DMEM	10	x	10092304 (Sigma Aldrich)
28	**C2C12**	Mouse	Muscle	Myoblast	RPMI	10	x	CRL-1772 (ATCC)
29	**CHO-K1**	Hamster	Ovary	Epithelium	F12	10	x	CCL-61 (ATCC)
30	**hMSC**	Human	Bone marrow	Mesenchymal stem cells	DMEM	10	x	PT-2501 (Lonza)

5.4 Results

Dataset

We assembled a dataset consisting of more than 4600 partially segmented brightfield and phase contrast microscopy images from several microscopy setups. Up to ten cellular and nuclear outlines were segmented per image, respectively, with a per image average of 11.4 total instances. As depicted in **Figure 36**, phase contrast and brightfield microscopy images (**Figure 36a**) were overlaid with fluorescent channels from membrane and/or nucleus staining (**Figure 36b**), to facilitate manual segmentation by human annotators (**Figure 36c**). Regarding the images in **Figure 36c**, the ratio of annotated instances to real instances within the image declined with lower magnification since more cells were included in the lower magnification images. Manual annotation was validated by experienced cell biologists, which – while being quite laborious - is the only way to guarantee human level accuracy even for low contrast cell lines such as hMSC (**Figure 36a**, second row image).

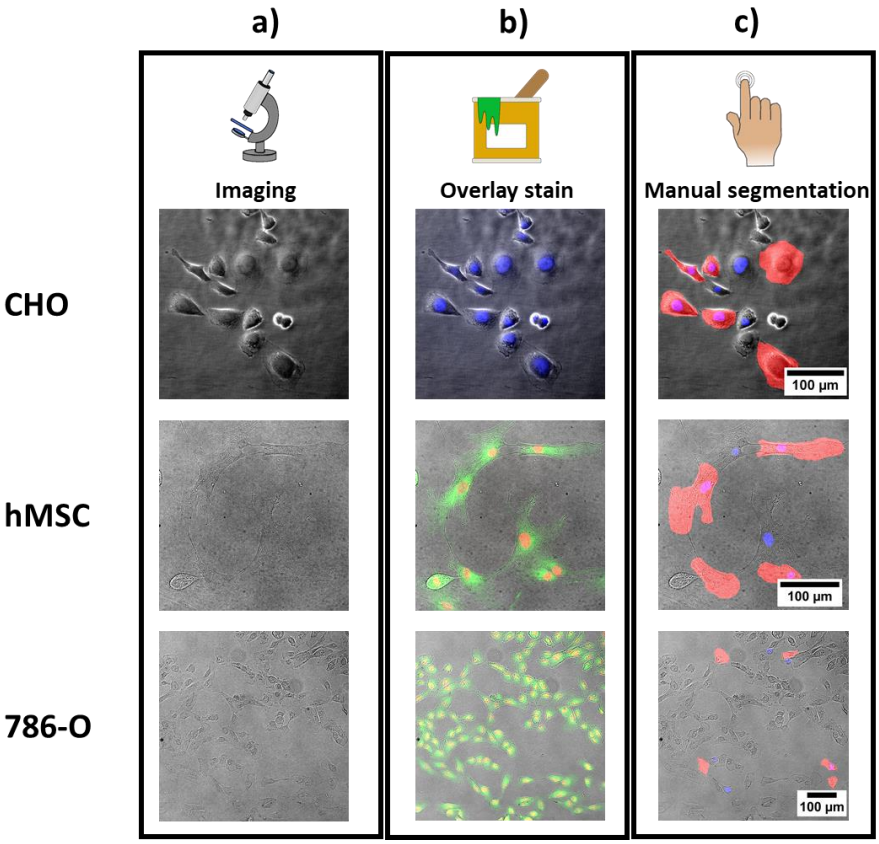

Figure 36 Dataset preparation pipeline

a) Acquisition of brightfield and phase contrast microscopy images from various microscopes at different magnifications. b) Overlay images of fluorescent nuclei and membrane, where available. c) Manual segmentation of cell bodies (red) and nuclei (blue) were saved as binary masks and transformed into COCO segmentation format.

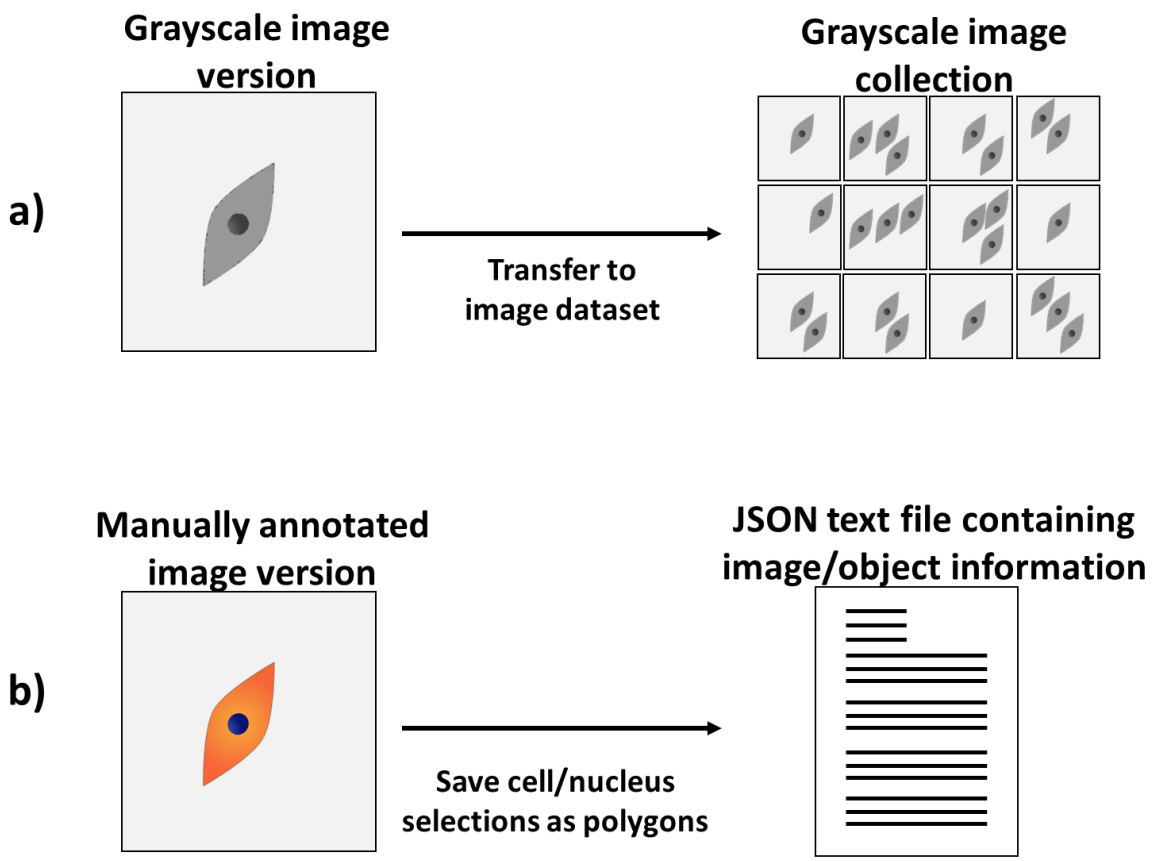

Figure 37 Dataset compilation

a) Grayscale (phase contrast and brightfield) image versions are collected in a large-scale image collection. b) Manual annotations (cell and nucleus segmentations) are transformed into polygons and saved in a JavaScript Object Notation file. The compiled text file includes information about images (ID, size, name) and objects (ID, class, polygon). All text information is referred to the grayscale image versions produced in (a).

Annotated images and corresponding grayscale versions (i.e. brightfield and phase contrast images) were compiled to a dataset consisting of a text file and an image collection in Joint Photographic Experts Group (JPEG)-format (see **Figure** 37**).** Manual annotations (i.e. segmentations) performed on stained image versions were transformed into polygons (i.e. "X1, Y1; X2, Y2;…; Xn, Yn") and saved, together with image and object information, in a JSON text file. While annotations were performed on stained images the information saved in the text file referred to the assembled grayscale image collection. Referring to grayscale images was necessary to ensure the usability of computer vision algorithms for phase contrast and brightfield images after training on this dataset.

Figure 38a shows the number of images for each cell line, with the majority containing >100 images. We provide two datasets in the COCO annotation format: the EVICAN2-version with two classes: "cell" and "nucleus", and the EVICAN60-version with nuclei and cells classified for each cell line, respectively, resulting in 60 class labels. As **Figure 38b** shows, we achieved a highly homogeneous distribution of nucleus and cell instances across all cell lines. For most classes in the EVICAN60-version we provide ~1000 instances, for the cell and nucleus class in EVICAN2 we exceeded 26,000 instances per class. **Figure 38c** shows the moderate underrepresentation of phase contrast images in our dataset, which as described later, contributes to less prominent feature observability due to reduced contrast in brightfield compared to phase contrast images. Additional to the COCO-format annotations, we provide

all masks as binary images with format “imageID_cellline.jpg” to offer freedom for developers and researcher not using COCO-like datasets.

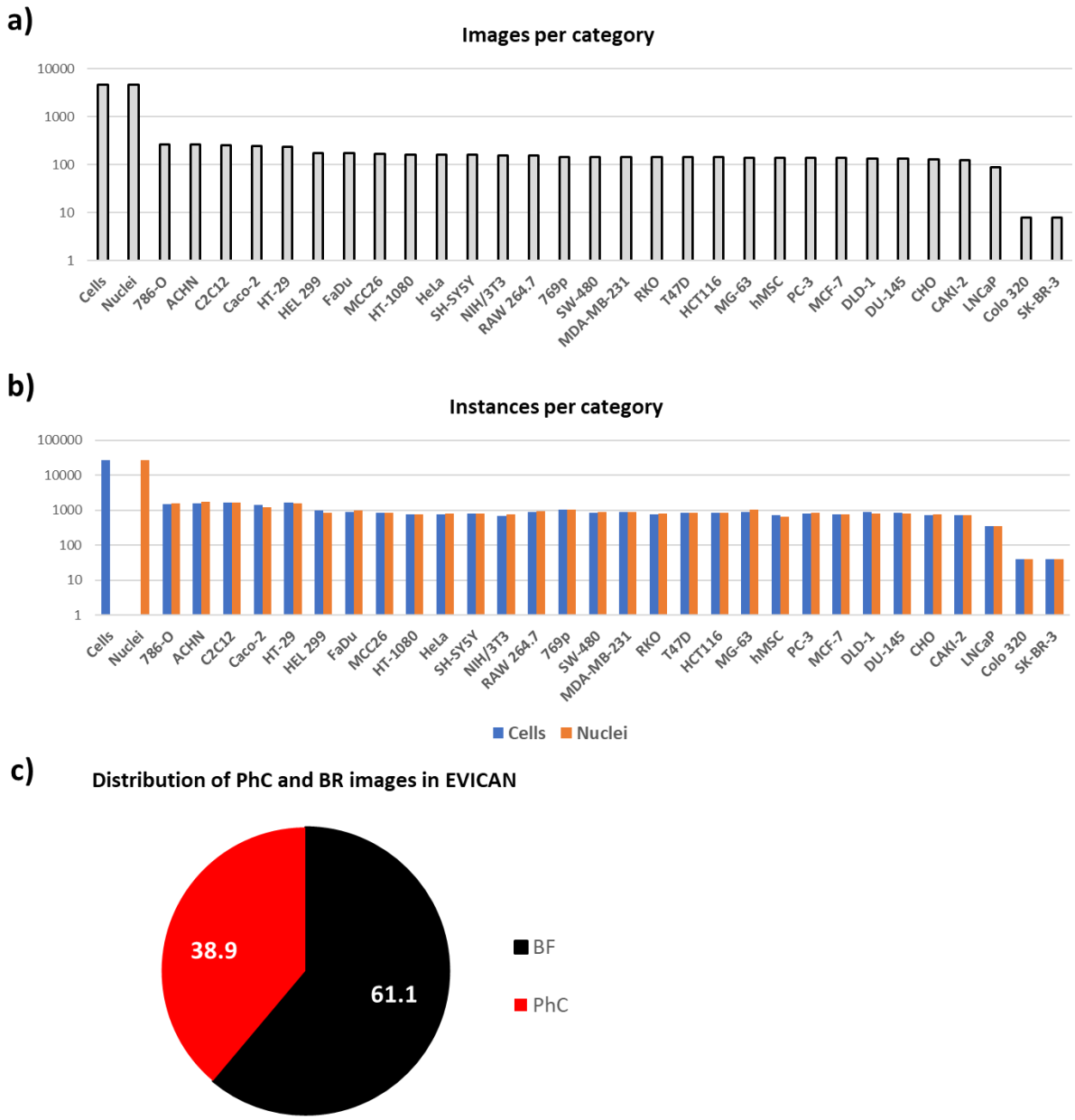

Figure 38. Overview of the EVICAN dataset

Number of images (a), numbers of instances (b) per category in the dataset, and c) Relative number of images for brightfield (BF) and phase contrast (PC) imaging in the dataset.

Comparison to other segmented datasets

We compared our dataset to four other commonly used datasets in cell biological segmentation:

- The 2018 Kaggle data science bowl dataset, containing 670 fully annotated (mostly stained) nuclei images from various sources with ~25,000 instances[142]. While providing a multitude of annotated instances, the dataset is limited
- The total number of phase contrast and DIC microscopy images of cell lines from the International Symposium on Biomedical Imaging (ISBI) cell tracking challenges from 2014 and 2015. This contained 4 videos of 115 frames each, with 52 annotated frames of 2 cell lines (i.e. 2 classes: HeLa and U373 cells) in total[96,143].
- Three combined datasets of phase contrast images by Gurari *et al.*[144] containing 151 partially segmented images of 3 cell lines.
- All DIC microscopy images of cell lines from the BBBC database[145], consisting of 65 fully segmented images for 2 classes: CHO and red blood cells.

Figure 39 shows the size of the EVICAN dataset - both editions - in comparison to the four datasets listed above. In both cases, the EVICAN datasets are larger by means of image number (number of images in the dataset correlates with point area) than any of the previously mentioned collections. With ~26,500 segmentation masks per category, EVICAN2 outperforms even the Kaggle nucleus dataset (25,000 segmentation masks for nuclei only), while providing double the number of classes with “cell” and “nucleus”. EVICAN60, in which all instances, cell and nucleus outlines are categorized by cell line, substantially outperforms all other datasets by means of category number (as well as image and instance number). Most datasets provide only a limited number of images and are often from one single experiment (e.g. the ISBI datasets are time-lapse image series monitoring the same microscopic field of view with the same microscope configuration over a longer period of time), reducing the heterogeneity within the dataset. The limited data and variation within the dataset will ultimately reduce the robustness of trained algorithms for general use outside of, e.g. the specific imaging system or specific cell lines used in training.

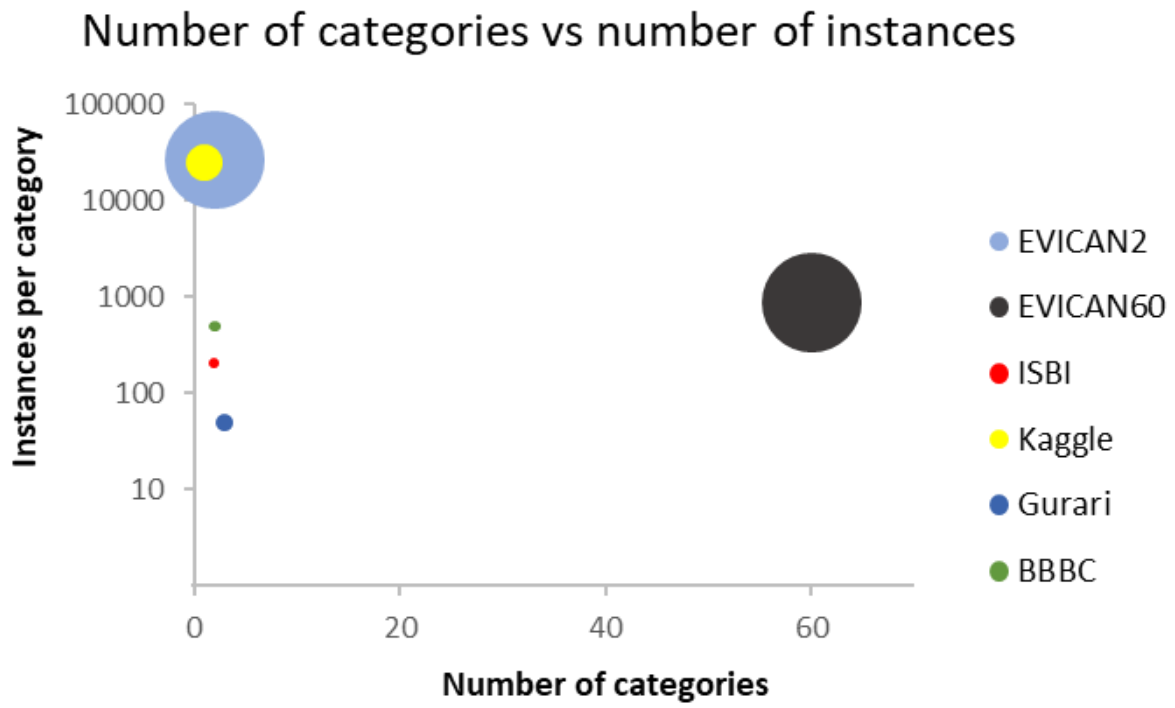

Figure 39 Comparison of the breadth and depth between EVCAN2 datasets and other large, annotated cell biology datasets

The EVICAN2, EVICAN 60, 2018 Kaggle Data Science Bowl DS, ISBI CT challenge DS, Gurari DS, and the BBBC light microscopy datasets are shown in the color indicated on the graph; each dataset is located by its number of categories and instances segmented. The size (area) of each symbol corresponds to the image number. Note the log scaling of the y-axis.

Classifier training

As a proof-of-principle demonstration of the usability of the EVICAN data for deep learning application computer vision applications, we used our EVICAN2 dataset to train a deep learning classifier using a modified version of Matterport inc's implementation of Mask R-CNN for image segmentation and object classification. To reduce the influence of unannotated cells on the background class, we prepared our dataset by Gaussian blurring (sigma = 30 pixel) everything except for the annotated instances plus an extra 10 pixel radius around their outlines. The Mask R-CNN algorithm was then trained on the background-reduced EVICAN2 dataset as described in the Methods section. The trained produced an algorithm for cellular and nuclear detection for both brightfield and phase contrast images.

We tested our trained algorithm on microscopy image evaluation datasets categorized in three classes of rising difficulty level. Average precision was computed at IoU thresholds above 0.5 ($AP_{0.5}$), above 0.75 ($AP_{0.75}$), and averaged over thresholds rising from 0.5 to 0.95 in 0.05 steps (AP). **Table 8** shows that with rising difficulty level of the evaluation data, average precision values indeed decreased, as expected.

Table 8 Comparison of Mask RCNN segmentation precision after training on EVICAN2 to segmentation precision after training on the COCO and Kaggle 2018 datasets.

	$AP_{0.5}$	$AP_{0.75}$	AP
EVICAN2			
Difficulty 1	58.3	9.6	21.3
Difficulty 2	27.2	3.6	9.3
Difficulty 3	12.2	0.06	3.8
COCO[64]	58.0	37.8	35.7
Kaggle 2018[141]	NA	NA	59.4

Assessing the lowest difficulty evaluation dataset, we achieved a slightly higher $AP_{0.5}$ score than reported for Mask R-CNN training on the everyday scene image dataset COCO[64]. The decreasing average precision with increasing IoU thresholds (i.e. scores of $AP_{0.75}$ and AP) indicates that a majority of positive detections in $AP_{0.5}$ is based on IoU values below 0.75. Algorithms trained on the COCO dataset (color images, 91 classes) and in the Kaggle data science bowl (mostly color images, one class) achieve higher AP scores, indicating better overlap of ground truth and detected instances.

With the combined annotation of cell bodies and nuclei in one dataset, we could also show the possibility to detect cells and subcellular features mutually in one step. For qualitative assessment, **Figure 40** shows exemplary input and output images for our algorithm.

It is apparent, that the algorithm produces better results on images with higher contrast (i.e. in phase contrast images, see **Figure 40** left and right column). Brightfield images, even with high magnification, often result in incorrect detections or missed cells/nuclei (see **Figure 40** middle column). Comparing the performance of our algorithm to other applications of the Mask RCNN approach, it is evident that algorithms trained on the COCO and Kaggle 2018 dataset reach higher average precision scores than training on EVICAN2. While COCO and the Kaggle 2018 dataset include colored or stained images, EVICAN relies solely on grayscale images, thereby limiting feature dimensionality.

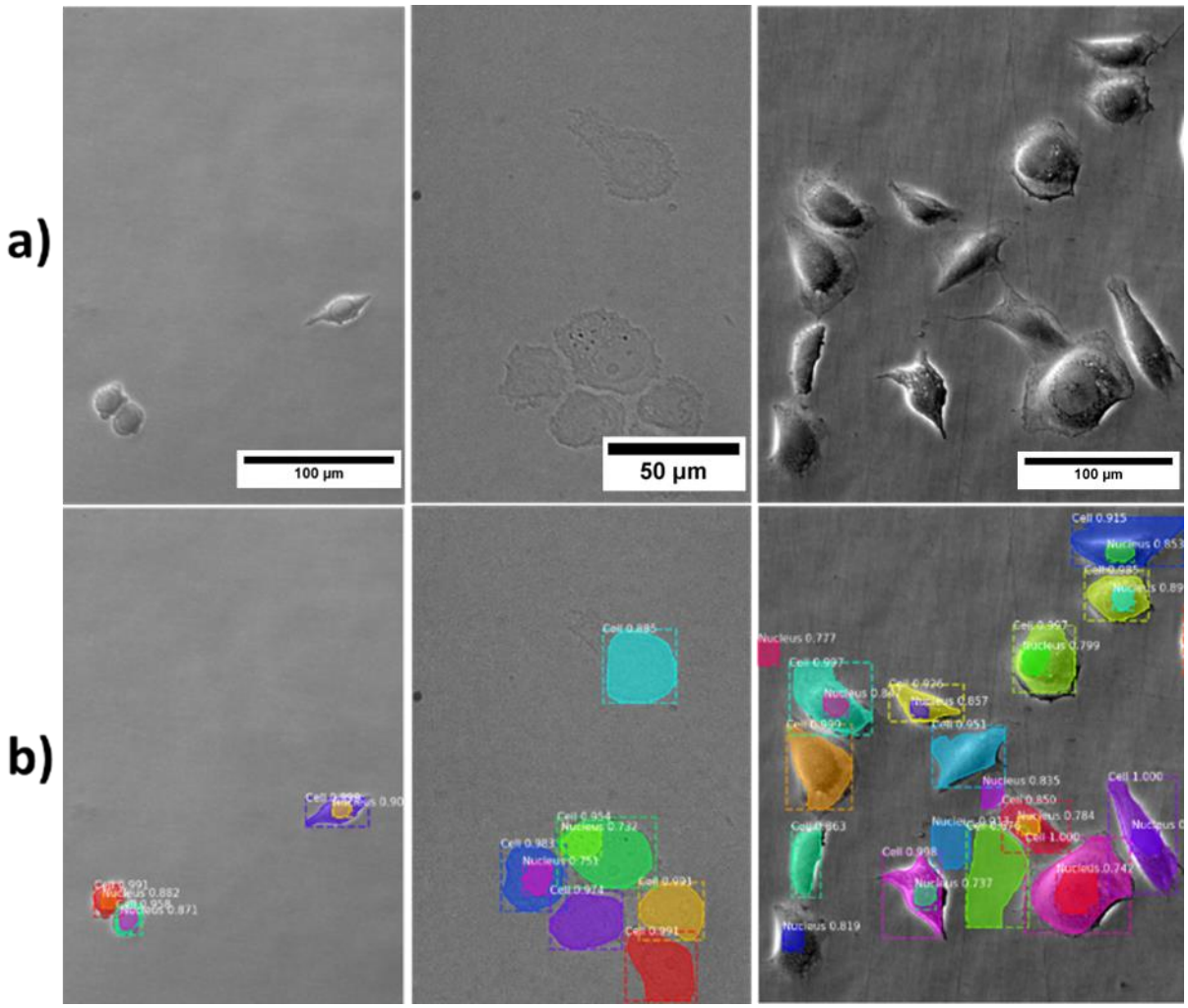

Figure 40 Exemplary input (a) and output (b) images for our algorithm
Varying colors indicate individual cell or nucleus segmentations, values (white) denote confidence of each detection (maximum = 1.0; all values above 0.7). Left: SW480 cells, imaged in phase contrast mode (20X objective), 100 % correctly detected cells; Middle: PC3 cells, imaged in brightfield mode (40X objective), Nuclei not or incorrectly detected; Right: CHO cells, imaged in phase contrast mode (20X objective), several false positive detections.

5.5 Discussion

The EVICAN dataset provides the first large-scale, multi-class annotated and segmented, mixed brightfield and phase contrast microscopy image collection covering a broad range of cell lines (30 adherent cell lines). Training computer vision algorithms on our dataset should enable computer scientists to produce faster and more accurate cell image segmentation and characterization tools using unstained images. This capability has the potential to strongly increase the ability of simple light microscopes to serve as quantitative instruments in cell biology labs. Although machine learning algorithms have been applied before to microscopy images, in part with remarkable success, image processing is still far behind the technology for image acquisition. Despite massive application of computer vision in other data intensive sectors like face recognition[139], progress in applying computer vision in cell microscopy is comparatively slow. We believe that this slow progress is due to two decoupled sectors: Computer scientists usually have no access to a biolab with adequate image acquisition machinery and most biologists lack the knowledge and skills to create or retrain computer

vision algorithms. We hope to overcome this gap between the sectors by providing computer scientists (and other algorithm developers) with our image collection. We provide two editions of our dataset: EVICAN2 with the classes “nucleus” and “cell” as well as EVICAN60 with 60 classes for 30 cell lines and their respective nuclei. Additionally, we provide three evaluation datasets accounting for varying image quality.

Using the EVICAN2 dataset version in a pilot machine learning application for cell and nucleus identification, we generated a classification and segmentation algorithm with an average precision up to 58.3 % at IoU scores above 0.5. Other groups have reported more robust results[64,141]. However, these algorithms rely on colored or stained images while EVICAN2 training yielded a detection algorithm for grayscale images. Feature availability is reduced in grayscale images, as one channel is used instead of three, which explains lower performance of resulting detection algorithms.

Performance of our algorithm was best for the lowest difficulty images in our evaluation dataset. This can be explained with a higher degree of feature presentation in images with few cell-cell contacts, strong contrast (e.g. from phase contrast), high resolution, and better focused image conditions. The COCO dataset was designed with object types recognizable by a 4-year old[68], while the EVICAN dataset includes cellular outlines and incorporated nuclei, that overlap, share a strong resemblance, and are often challenging to see without staining, even by a trained individual.

Better performance on high resolution and magnification images could arise from higher feature visibility that is lost in lower resolution. Phase contrast images provide a higher contrast; features appear more prominently, which facilitates feature detection in the convolutional process. Nevertheless, the limited dimensionality (as a consequence of the grayscale nature of the images) prevents the algorithm from searching for color-encoded features.

We believe with the right tools (e.g. multi-GPU support) and advanced image augmentation, the EVICAN60 version can lead to an even more revolutionary algorithm development. Such an algorithm would be capable of not only segmenting cells and nuclei within an image, but also discriminate between cell types in co-cultures. Such an algorithm would open the door to a whole new era of cell microscopy: All cells in a microscopic field could be adequately measured label-free (i.e. determination of cell spreading, elongation, circularity, etc.), cell migration in assays or under culture conditions could be monitored, and individual cellular contacts (especially in co-cultures) could be mapped and connected to morphology changes. We hope computer scientists and computational biologists use our dataset in efforts to achieve this goal.

5.6 Acknowledgements

We cordially thank our annotators Ravi Dhiman, Evelyn Schwendy, Kevin Kellner, and Mohamed Afhakama. Support by the IMB Microscopy Core Facility is gratefully acknowledged, especially from Maria Hanulova and Sandra Ritz who provided technical assistance and training on the Opera Phenix and AF7000 microscopes. We thank Frederik F. Fleissner who provided fruitful discussions.

6 Outlook

6.1 Future directions

In this thesis, I covered two broad topics: Cellular behavior in an atherosclerosis model and image processing technology and how these two topics were used together. Research in both areas is currently highly topical, with atherosclerosis still being the disease with the highest mortality rates and image processing undergoing exceptional transformations through machine-learning assisted computer vision. After studying both fields in great detail during my PhD project, I now want to give an outlook how my projects could be advanced and what can be expected within the next years.

6.2 Atherosclerotic research

We could show that the microenvironmental stiffness matters during lipid uptake of macrophages. While neglected to a large degree over the last decades, mechanical factors in atherosclerotic plaque development should now be considered in more detail. As a first study, the repetition of our approach using THP-1 with continuously expressed scavenger receptor A and CD36 would help to clarify its prominent role in stiffness mediated lipid uptake. Additionally, it might be advantageous to probe cellular lipid uptake in a 3D hydrogel model. This adds several obstacles such as quantification of LDL particle diffusion into the scaffold and limited light penetration through the gel (hindering microscopy). Preparing gel slices using a cryotome could solve the latter problem. A nonpoisonous hydrogel with tunable stiffness would be needed as substrate. Possible candidates could be agarose, (poly ethylene) glycol, or alginate-based hydrogels. As the 2D approach of seeding macrophages on hydrogels in this thesis neglected the third dimension, results in this model could differ from our observations and more appropriately mimic the natural conditions of the intimal space during atherosclerosis.

Another interesting study could be an implantation of two artery prostheses (i.e. an artificial piece of artery) into a mouse model prone to atherosclerosis development. Equipping the prostheses with hydrogels of 4 kPa and 50 kPa (Young's modulus) would mimic early and late-stage mechanical properties in plaque development. Explanting the two models after extended incubation, would allow studying lipid uptake in extravasated macrophages from both mechanical conditions from the same living sample. However, to achieve this, a cell penetrable, mechanically tunable hydrogel would be necessary.

Finally, I believe that genetic engineering might have an outstanding impact on atherosclerosis research. First results showed lowered cholesterol levels in mice after *in vivo* alteration of a single control gene[146]. Although debated ethically, this shows the power of gene-editing approaches. However, target proteins need to be identified before gene-editing is feasible, therefore more studies should be applied to reveal all roles of potential candidate proteins like scavenger receptor A or CD36.

6.3 Image processing for microscopy

While the DRAQ5-dependent cell segmentation algorithm presented in Chapter 3 is a ready-to-use solution for the popular scientific image processing suite FIJI/ImageJ, the computer vision algorithm presented in Chapter 5 is not embedded in any image processing software with graphical user interface. Application of the computer vision cell segmentation algorithm requires programming skills, which limits the applicability amongst potential users. I highly recommend the advancement of the algorithm to be included in a popular software for image processing (e.g. FIJI/ImageJ or CellProfiler). Until higher precision values are achieved by the algorithm, I would also suggest to implement a semi-automated version of the software, in which incorrect cell detection can be corrected manually (e.g. with a selection brush tool). While making the application more laborious, this would guarantee human level precision in cell image experiments.

Image processing is a fast-evolving field and the algorithms presented in this thesis might in fact even be outdated within a few years. I believe that machine-learning assisted algorithms will dominate the development in this field over the next decade. Starting with "simple" solutions such as enhanced autofocus in automated microscopes or unstained cell detections in real time during image acquisition. This would add unforeseen quantitative features to conventional microscopes present in almost every cell culture lab. In a next step "scene understanding" might play a prominent role (i.e. keyword or even linguistic representations of the image scene). While used to derive data in real life images[147], this approach could be highly efficient in cell microscopy. Individual cells could not only be tracked but also interactions (e.g. cell division or colony formation) mapped. Data could therefore be generated in another dimension by recording time-lapse videos and monitoring cellular interactions relative to cell fate (e.g. number of cell divisions before cell death of one individual cell).

Using cell image datasets such as the EVICAN 60 format from Chapter 5 could additionally enable classification of multiple various cell types (e.g. "HeLa", "CHO", "C2C12"). The ability to classify different cell types would not only allow scientists to follow potentially changed behavior of cells in a co-culture, but also monitor differentiation in real-time in a quantitative (e.g. spreading area, protrusion formation) and qualitative fashion (e.g. the transition from class "mesenchymal stem cell" to class "osteoblast" or class "adipocyte"). Assuming a sufficient precision of a classification/segmentation-algorithm, high-level and currently cost-intensive experiments could be performed without staining and using conventional laboratory equipment.

6.4 Unsupervised learning

In addition to the supervised learning approach of computer vision, which is covered in this thesis, another system may take a more prominent role in the next generation of image processing software: Unsupervised learning. In unsupervised learning, computer vision algorithms learn features from unlabeled images according to a predetermined number of classes. E.g. an unsupervised algorithm would learn to segment the object classes "person" and "background" from images of persons in front of a white background and the information that it should find two classes. Unsupervised algorithms have already shown powerful potential in everyday scene segmentation[148] and even in microscopy image segmentation of pathologic tissues[149]. As image generation in microscopy is no bottleneck (due to automated

setups) and unsupervised learning eliminates the burden of image annotation, the method would be perfectly suited for the field of cell microscopy. While supervised software adopts human biases like individual differences in segmentation accuracy or annotation mistakes (e.g. labeling a nucleus as “cell”), unsupervised software shows no, or limited biases (e.g. depending on provided class number).

Eventually, unsupervised algorithms detect subtle changes, which could be missed by human annotators. Especially in cell biology, subtle changes can have strong impacts. For example, cellular subpopulations in a tumor that escape cell-cycle arrest after chemotherapy[150]. The enhanced detection of subtle object-variations within images, using unsupervised learning, might allow the identification of new cell phenotypes or subpopulations that differ from the remaining cell population.

7 Acknowledgements

Throughout my time at the MPIP, I had the pleasure of meeting and collaborating with fantastic colleagues and friends. This thesis and the work behind it would not have been possible without tremendous help and assistance from many people at the MPIP, the IMB, and the JGU.

I would like to thank Sapun Parekh for his supervision over the last four years. At times, I'm sure, it was not easy to supervise a biotechnologist in a polymer institute. Thank you for putting faith in me even when I was close to giving up, for giving me the freedom to shape my projects, for your advice when I got stuck, and for motivating the whole group in- and outside the lab! Although it might sound strangely selfish at first, I want to thank Mischa. Mischa Bonn, who gave me the opportunity to work and learn in his department. Thank you so much for steering my projects, editing my manuscripts, and keeping an eye on the big picture, even though my topics deviated from the spectroscopy field. I want to thank Ron Unger, my supervisor from the Uniklinikum Mainz. Your advice was indispensable during my project – thank you for your constant positive attitude, for correcting various paper manuscripts, and for offering your microscopes, cell lines, and labs whenever I needed help or support.

I want to thank all members of the CARS group! Sabine, thank you so much for keeping the Biolab functioning, for having an open ear for all work and off-work issues, and for all the years of advice in our group meetings. Sachin Kumar Binay Kumar and YuJen, thank you for all the discussions about science and the great trip to Heidelberg. Also, I want to thank Samet for shaping my sense for the importance of error bars and discussing food origins. Thank you to Nils, Xiao, Yelena, Shruti, Tarek, and Lukas for all your support in the lab or in our group meetings. Most importantly, I want to thank Frederik F. Fleissner, who had a substantial impact not only on my work, but also on my personal development during my PhD. Thank you for your guidance in the lab, thank you for your scientific advice, thank you for your brutally honest criticism, thank you for being my friend!

Of course, I want to thank Laurie Gangloff, who "manages the manager" and honestly everyone else in the department. Yet still, I have not seen her annoyed or stressed in all the years I spent at the institute! Thank you for doing such an amazing job – I don't know what the institute would do without you! Speaking of "what would the institute do without you": Thank you Marc-Jan and Florian for being able to build/fix whatever on earth is needed!

I also wish to thank Sandra Ritz and Maria Hanulova for the access to and training on the microscopes at the IMB, and Anke Kaltbeitzel for assistance with the confocal microscope at the MPIP. Thank you, Henrick Muller for the Email correspondence!

Apart from lab-work, I want to thank Oya Ustahüseyin, who made the beginning of my PhD far more entertaining! Thank you especially for teaching the dancing class with me in the beginning! Thank you, Amelie, Laura, Simon, and Malte for regular kicker matches in the breaks, I hope I can use these skills in my future! Of course, I also want to thank the people who left over the years: Ruth and Andy for being the social epicenter of the after-work-group, Saman for hours of lunch talks, and Sergio for the freeletics group.

I want to express my eternal gratitude to the whole office 2.504! Thank you for arguing over thousands of hypothetical social questions, thank you for all the jokes, the coffee breaks, and the amazing team spirit! Thank you, Christoph for the daily exchanges about news and politics,

and your support during acute frustration! Thank you, Sudipta for enduring my parent-like behavior for almost four years, I'm proud of you! Thank you, Jan for sporadic football chats and fellow suffering during the freeletics-age. Maksim, thank you for your efforts in teaching me physics, for the office-beers, and your never-ending willingness to discuss scientific, social, or personal issues!

In the beginning of my PhD, I was extremely lucky to meet Christian and Lisa. Thank you both so much for your friendship, the evenings we spent, the trivia nights in the pub, and endless hours of chatting about the world! Chris thank you for four great years of sharing an office and sometimes even a desk!

Zuletzt möchte ich meinen Freunden und meiner Familie danken! Danke, dass ihr mich nicht fallengelassen habt, selbst in den Wochen, als ich kaum mehr Zeit für euch hatte! Bitte verzeiht mir die „Programmierwochenenden" und „Thesisabende". Besonders möchte ich hier Corinna Mieth, Kevin Kellner und Marco Metzger hervorheben! Ich danke euch für eure moralische Unterstützung und die gelegentlichen Ablenkungen am Wochenende! Corinna, dir ein besonderer Dank dafür, dass du in den letzten Jahren den Tanzkurs mit mir unterrichtet hast! Ein unendliches Dankeschön geht an meine Eltern Karin und Steffen Schwendy, meine Schwester Natalie und meinen Bruder Sascha! Danke, dass ihr mich großgezogen, beraten und unterstützt habt! Danke, dass ihr mir die Werte vermittelt habt, die mich zu diesem Punkt geführt haben!

Liebe Evelyn, das war eine lange Reise. Tausend Dank, dass du mich darauf begleitet hast. Verzeih mir die Nächte, die ich schreibend oder programmierend verbracht habe! Danke für dein Verständnis und deine Unterstützung auch in den schwersten Zeiten! Danke, dass du mein ganzes Leben besser machst!

8 Bibliography

1. Edkins, K. The Project Gutenberg, Micrographia, by Robert Hooke. *Society* 1–178 (2005). doi:10.5962/bhl.title.904
2. Amos, B. Lessons from the history of light microscopy. *Nat Cell Biol* **2,** E151-2 (2000).
3. Schultheiss, D. & Denil, J. History of the microscope and development of microsurgery: A revolution for reproductive tract surgery. *Andrologia* **34,** 234–241 (2002).
4. Abbe, E. VII.-On the Estimation of Aperture in the Microscope. *J. R. Microsc. Soc.* **1,** 388–423 (1881).
5. Zernike, F. How I Discovered Phase Contrast. **121,** 345–349 (1955).
6. Chalfie, M., Tu, Y., Euskirchen, G., Ward, W. & Prasher, D. Green fluorescent protein as a marker for gene expression. *Science (80-.).* **263,** 802–805 (1994).
7. Ruska, E. The development of the electron microscope and of electron microscopy. *Biosci. Rep.* **7,** 607–629 (1987).
8. Klar, T. A., Jakobs, S., Dyba, M., Egner, A. & Hell, S. W. Fluorescence microscopy with diffraction resolution barrier broken by stimulated emission. *Proc. Natl. Acad. Sci.* **97,** 8206–8210 (2000).
9. Betzig, E. *et al.* Imaging Intracellular Fluorescent Proteins at Nanometer Resolution. **x,** 1642–1646 (2006).
10. Nagerl, U. V., Willig, K. I., Hein, B., Hell, S. W. & Bonhoeffer, T. Live-cell imaging of dendritic spines by STED microscopy. *Proc. Natl. Acad. Sci.* **105,** 18982–18987 (2008).
11. Manley, S. *et al.* High-density mapping of single-molecule trajectories with photoactivated localization microscopy. *Nat. Methods* **5,** 155–157 (2008).
12. Alberts, Bruce; Johnson, Alexander; Lewis, Julian; Morgan, David; Raff, Martin; Roberts, Keith; Walter, P. *Molecular Biology of the Cell*. (W. W. Norton & Company, 2014).
13. Pollard, T. D. & Cooper, J. A. Actin, a central player in cell shape and movement. *Science (80-.).* **326,** 1208–1212 (2009).
14. Caviston, J. P. & Holzbaur, E. L. F. Microtubule motors at the intersection of trafficking and transport. *Trends Cell Biol.* **16,** 530–537 (2006).
15. Fletcher, D. A. & Mullins, R. D. Cell mechanics and the cytoskeleton. **463,** 485–492 (2010).
16. Herrmann, H., Bär, H., Kreplak, L., Strelkov, S. V. & Aebi, U. Intermediate filaments: From cell architecture to nanomechanics. *Nat. Rev. Mol. Cell Biol.* **8,** 562–573 (2007).
17. Pullarkat, P. A., Fernández, P. A. & Ott, A. Rheological properties of the Eukaryotic cell cytoskeleton. *Phys. Rep.* **449,** 29–53 (2007).
18. Huang, S. & Ingber, D. E. MINIREVIEW Shape-Dependent Control of Cell Growth , Differentiation , and Apoptosis : Switching between Attractors in Cell Regulatory Networks. **103,** 91–103 (2000).
19. Engler, A. J., Sen, S., Sweeney, H. L. & Discher, D. E. Matrix Elasticity Directs Stem Cell Lineage Specification. 677–689 (2006). doi:10.1016/j.cell.2006.06.044
20. McWhorter, F. Y., Wang, T., Nguyen, P., Chung, T. & Liu, W. F. Modulation of macrophage phenotype by cell shape. *Proc. Natl. Acad. Sci. U. S. A.* **110,** 17253–8 (2013).
21. Chen, S. *et al.* Characterization of topographical effects on macrophage behavior in a foreign body response model. *Biomaterials* **31,** 3479–3491 (2010).
22. Mcbeath, R., Pirone, D. M., Nelson, C. M., Bhadriraju, K. & Chen, C. S. Cell Shape , Cytoskeletal Tension , and RhoA Regulate Stem Cell Lineage Commitment. **6,** 483–495 (2004).
23. Reilly, G. C. & Engler, A. J. Intrinsic extracellular matrix properties regulate stem cell differentiation. *J. Biomech.* **43,** 55–62 (2010).
24. Mcwhorter, F. Y. *et al.* Macrophage secretion heterogeneity in engineered microenvironments revealed

using a microwell platform. *Integr. Biol.* **8,** 751–760 (2016).

25. Dorweiler, B. *et al.* A novel in vitro model for the study of plaque development in atherosclerosis. *Thromb. Haemost.* **95,** 56–64 (2005).

26. Insull, W. The Pathology of Atherosclerosis: Plaque Development and Plaque Responses to Medical Treatment. *Am. J. Med.* **122,** S3–S14 (2009).

27. A.E., M. *et al.* The global burden of ischemic heart disease in 1990 and 2010: The global burden of disease 2010 study. *Circulation* **129,** 1493–1501 (2014).

28. Libby, P., Ridker, P. M. & Hansson, G. K. Progress and challenges in translating the biology of atherosclerosis. *Nature* **473,** 317–25 (2011).

29. Zuniga, M. C., White, S. L. P. & Zhou, W. Design and utilization of macrophage and vascular smooth muscle cell co-culture systems in atherosclerotic cardiovascular disease investigation. *Vasc. Med.* **19,** 394–406 (2014).

30. Yu, X. H., Fu, Y. C., Zhang, D. W., Yin, K. & Tang, C. K. Foam cells in atherosclerosis. *Clin. Chim. Acta* **424,** 245–252 (2013).

31. Pasterkamp, G. *et al.* Atherosclerotic arterial remodeling and the localization of macrophages and matrix metalloproteases 1, 2 and 9 in the human coronary artery. *Atherosclerosis* **150,** 245–253 (2000).

32. Tracqui, P. *et al.* Mapping elasticity moduli of atherosclerotic plaque in situ via atomic force microscopy. *J. Struct. Biol.* **174,** 115–123 (2011).

33. Witztum, J. L. & Witztum, J. L. You are right too! **115,** 2072–2075 (2005).

34. Yuan, Y., Li, P. & Ye, J. Lipid homeostasis and the formation of macrophage-derived foam cells in atherosclerosis. *Protein Cell* **3,** 173–181 (2012).

35. Moore, K. J. & Freeman, M. W. Scavenger receptors in atherosclerosis: Beyond lipid uptake. *Arterioscler. Thromb. Vasc. Biol.* **26,** 1702–1711 (2006).

36. Ghosh, S., Zhao, B., Bie, J. & Song, J. Macrophage cholesteryl ester mobilization and atherosclerosis. *Vascul. Pharmacol.* **52,** 1–10 (2010).

37. Collot-Teixeira, S., Martin, J., McDermott-Roe, C., Poston, R. & McGregor, J. L. CD36 and macrophages in atherosclerosis. *Cardiovasc. Res.* **75,** 468–477 (2007).

38. Bessi, V. L. *et al.* EP 80317, a selective CD36 ligand, shows cardioprotective effects against post-ischaemic myocardial damage in mice. *Cardiovasc. Res.* **96,** 99–108 (2012).

39. Park, Y. M. CD36, a scavenger receptor implicated in atherosclerosis. *Exp. Mol. Med.* **46,** e99 (2014).

40. Herijgers, N., Van Eck, M., Groot, P. H. E., Hoogerbrugge, P. M. & Van Berkel, T. J. C. Low density lipoprotein receptor of macrophages facilitates atherosclerotic lesion formation in C57B1/6 mice. *Arterioscler. Thromb. Vasc. Biol.* **20,** 1961–1967 (2000).

41. Khoo, J. C., Miller, E., Pio, F., Steinberg, D. & Witztum, J. L. Monoclonal antibodies against LDL further enhance macrophage uptake of LDL aggregates. *Arterioscler. Thromb. Vasc. Biol.* **12,** 1258–1266 (1992).

42. Haka, A. S. *et al.* Macrophages create an acidic extracellular hydrolytic compartment to digest aggregated lipoproteins. *Mol. Biol. Cell* **20,** 4932–4940 (2009).

43. Patel, M. *et al.* The Cytoplasmic Domain of the Low Density Lipoprotein (LDL) Receptor-related Protein, but Not that of the LDL Receptor, Triggers Phagocytosis. *J. Biol. Chem.* **278,** 44799–44807 (2003).

44. Schrijvers, D. M., De Meyer, G. R. Y., Herman, A. G. & Martinet, W. Phagocytosis in atherosclerosis: Molecular mechanisms and implications for plaque progression and stability. *Cardiovasc. Res.* **73,** 470–480 (2007).

45. Asmis, R., Begley, J. G., Jelk, J. & Everson, W. V. Lipoprotein aggregation protects human monocyte-derived macrophages from OxLDL-induced cytotoxicity. **46,** (2005).

46. Paul, A., Chan, L. & Bickel, P. The PAT family of lipid droplet proteins in heart and vascular cells. *Curr. Hypertens. Rep.* **10,** 461–6 (2008).

47. Bhakdi, S. *et al.* On the pathogenesis of atherosclerosis: enzymatic transformation of human low density lipoprotein to an atherogenic moiety. *J. Exp. Med.* **182,** 1959–1971 (1995).

48. Öörni, K., Pentikäinen, M. O., Ala-korpela, M. & Kovanen, P. T. Aggregation , fusion , and vesicle formation of modified low density lipoprotein particles : molecular mechanisms and effects on matrix interactions. **41,** 1703–1714 (2000).

49. Li, H., Horke, S. & Förstermann, U. Oxidative stress in vascular disease and its pharmacological prevention. *Trends Pharmacol. Sci.* **34,** 313–319 (2013).

50. Murphy, D. B., Davidson, M. W. & Wiley, a J. *LIGHT MICROSCOPY AND ELECTRONIC IMAGING FUNDAMENTALS OF LIGHT MICROSCOPY AND ELECTRONIC Second Edition*. (2013).

51. Mondal, P. P. & Diaspro, A. *Fundamentals of Fluorescence Microscopy*. (Springer Netherlands, 2014). doi:10.1007/978-94-007-7545-9

52. Drucker, H., Wu, D. & Vapnik, V. N. Support Vector Machines for Spam Categorization. **10,** 1048–1054 (1999).

53. Schafer, J. Ben; Konstan, Joseph A.; Riedl, J. E-Commerce Recommendation Applications. 115–153 (2001).

54. Gandomi, A. & Haider, M. Beyond the hype : Big data concepts , methods , and analytics. *Int. J. Inf. Manage.* **35,** 137–144 (2015).

55. Mountrakis, G., Im, J. & Ogole, C. Support vector machines in remote sensing : A review. *ISPRS J. Photogramm. Remote Sens.* **1,** 1–13 (2010).

56. Lecun, Y., Bengio, Y. & Hinton, G. Deep learning. *Nature* **521,** 436–444 (2015).

57. Hubel, B. Y. D. H. *et al.* Receptive fields, binocular interaction and functional architecture in the cat's visual cortex. *J. Physiol.* **160,** 106–154 (1962).

58. Amato, F., López, A., Peña-méndez, E. M., Vaňhara, P. & Hampl, A. Artificial neural networks in medical diagnosis. (2013). doi:10.2478/v10136-012-0031-x

59. LeCun, Y., Bengio, Y. & Haffner, P. Gradient-Based Learning Applied to Document Recognition. **86,** (1998).

60. Krizhevsky, A., Sutskever, I. & Hinton, G. E. ImageNet Classification with Deep Convolutional Neural Networks. *Adv. Neural Inf. Process. Syst.* 1–9 (2012). doi:http://dx.doi.org/10.1016/j.protcy.2014.09.007

61. Girshick, R., Donahue, J., Darrell, T. & Malik, J. Rich feature hierarchies for accurate object detection and semantic segmentation. *Proc. IEEE Comput. Soc. Conf. Comput. Vis. Pattern Recognit.* 580–587 (2014). doi:10.1109/CVPR.2014.81

62. Girshick, R. Fast R-CNN. *Proc. IEEE Int. Conf. Comput. Vis.* **2015 Inter,** 1440–1448 (2015).

63. Ren, S., He, K., Girshick, R. & Sun, J. Faster R-CNN: Towards Real-Time Object Detection with. *IEEE Trans. Pattern Anal. Mach. Intell.* **39,** 1137–1149 (2017).

64. He, K., Gkioxari, G., Dollar, P. & Girshick, R. Mask R-CNN. *Proc. IEEE Int. Conf. Comput. Vis.* **2017–Octob,** 2980–2988 (2017).

65. Uijlings, J. R. R., Van De Sande, K. E. A., Gevers, T. & Smeulders, A. W. M. Selective Search for Object Recognition. (2012). doi:10.1007/s11263-013-0620-5

66. Paszke, A., Chaurasia, A., Kim, S. & Culurciello, E. ENet: A Deep Neural Network Architecture for Real-Time Semantic Segmentation. 1–10 (2016). doi:10.1109/CRV.2016.27

67. Deng, J. *et al.* ImageNet : a Large-Scale Hierarchical Image Database ImageNet : A Large-Scale Hierarchical Image Database. (2009). doi:10.1109/CVPR.2009.5206848

68. Lin, T. Y. *et al.* Microsoft COCO: Common objects in context. *Lect. Notes Comput. Sci. (including Subser. Lect. Notes Artif. Intell. Lect. Notes Bioinformatics)* **8693 LNCS,** 740–755 (2014).

69. Schmidt, U., Weigert, M., Broaddus, C. & Myers, G. Cell Detection with Star-convex Polygons.

70. Tsuchiya, S. *et al.* Establishment and characterization of a human acute monocytic leukemia cell line (THP-1). *Int. J. Cancer* **26,** 171–6 (1980).

71. Qin, Z. The use of THP-1 cells as a model for mimicking the function and regulation of monocytes and

macrophages in the vasculature. *Atherosclerosis* **221,** 2–11 (2012).

72. Chanput, W., Mes, J. J. & Wichers, H. J. THP-1 cell line: An in vitro cell model for immune modulation approach. *Int. Immunopharmacol.* **23,** 37–45 (2014).

73. Tse, J. R. & Engler, A. J. Preparation of Hydrogel Substrates with Tunable Mechanical Properties. 1–16 (2010). doi:10.1002/0471143030.cb1016s47

74. Khoo, J. C., Miller, E., McLoughlin, P. & Steinberg, D. Enhanced macrophage uptake of low density lipoprotein after self- aggregation. *Arterioscler. Thromb. Vasc. Biol.* **8,** 348–358 (1988).

75. Brenner, S. L. & Korn, D. Inhibition of actin polymerization by latrunculin A. *FEBS Lett.* **2,** 316–318 (1987).

76. Morton, W. M., Ayscough, K. R. & Mclaughlin, P. J. Latrunculin alters the actin-monomer subunit interface to prevent polymerization. **2,** 376–378 (2000).

77. Parekh, S. H. *et al.* Modulus-driven differentiation of marrow stromal cells in 3D scaffolds that is independent of myosin-based cytoskeletal tension. *Biomaterials* **32,** 2256–2264 (2011).

78. Hwang, J., Byun, M. R., Kim, A. R., Kim, K. M. & Cho, H. J. Extracellular Matrix Stiffness Regulates Osteogenic Differentiation through MAPK Activation. 1–16 (2015). doi:10.1371/journal.pone.0135519

79. Ravelli, R. B. G. *et al.* Insight into tubulin regulation from a complex with colchicine and a stathmin-like domain. *Nature* **428,** 198–202 (2004).

80. Goldman, R. D. The role of three cytoplasmic fibers in BHK-21 cell motility: I. Microtubules and the effects of colchicine. *J. Cell Biol.* **51,** 752–762 (1971).

81. Georges, P. C. & Janmey, P. a. Cell type-specific response to growth on soft materials. *J. Appl. Physiol.* **98,** 1547–1553 (2005).

82. Smith, P. J., Wiltshire, M. & Errington, R. J. DRAQ5 Labeling of Nuclear DNA in Live and Fixed Cells. *Curr. Protoc. Cytom.* 1–11 (2004). doi:10.1002/0471142956.cy0725s28

83. Listenberger, L. L. & Brown, D. A. Fluorescent Detection of Lipid Droplets and Associated Proteins. *Curr. Protoc. Cell Biol.* 1–11 (2007). doi:10.1002/0471143030.cb2402s35

84. Ravikumar, B., Moreau, K., Jahreiss, L., Puri, C. & Rubinsztein, D. C. Plasma membrane contributes to the formation of pre-autophagosomal structures. *Nat. Cell Biol.* **12,** 747–757 (2010).

85. Radford, R. J., Chyan, W. & Lippard, S. J. Peptide-based targeting of fluorescent zinc sensors to the plasma membrane of live cells. *Chem. Sci.* **4,** 3080–3084 (2013).

86. Branco da Cunha, C. *et al.* Influence of the stiffness of three-dimensional alginate/collagen-I interpenetrating networks on fibroblast biology. *Biomaterials* **35,** 8927–8936 (2014).

87. Wong, A. D. & Searson, P. C. Live-cell imaging of invasion and intravasation in an artificial microvessel platform. *Cancer Res.* 4937–4946 (2014). doi:10.1158/0008-5472.CAN-14-1042

88. Mask R-CNN implementation by Matterport Inc. (2018). Available at: https://github.com/matterport/Mask_RCNN.

89. Wu, S., Zhong, S. & Liu, Y. Deep residual learning for image steganalysis. *Multimed. Tools Appl.* 1–17 (2017). doi:10.1007/s11042-017-4440-4

90. Meyer, F. & Beucher, S. Morphological Segmentation. (1990).

91. Carpenter, A. E. *et al.* CellProfiler : image analysis software for identifying and quantifying cell phenotypes. **7,** (2006).

92. Ingram, M. & Jr, K. P. Automatic analysis of blood cells. **223,** 72–83 (1970).

93. Schindelin, J. *et al.* Fiji - an Open Source platform for biological image analysis. **9,** (2012).

94. Edelstein, A., Amodaj, N., Hoover, K., Vale, R. & Stuurman, N. Computer Control of Microscopes Using μ Manager. 1–17 (2010). doi:10.1002/0471142727.mb1420s92

95. Wählby, C., Lindblad, J., Vondrus, M., Bengtsson, E. & Björkesten, L. Algorithms for cytoplasm segmentation of fluorescence labelled cells. **24,** 101–111 (2002).

96. Ronneberger, O., Fischer, P. & Brox, T. U-Net: Convolutional Networks for Biomedical Image Segmentation. 1–8 (2015). doi:10.1007/978-3-319-24574-4_28

97. Kim, J. Y., Kim, Y. & Lee, G. M. CHO cells in biotechnology for production of recombinant proteins : current state and further potential. 917–930 (2012). doi:10.1007/s00253-011-3758-5

98. Raw data and processing files. Available at: https://edmond.mpdl.mpg.de/imeji/collection/quuxweXFiBEQnctM?q=.

99. Buggenthin, F. *et al.* An automatic method for robust and fast cell detection in bright field images from high-throughput microscopy. *BMC Bioinformatics* **14,** (2013).

100. Bajcsy, P. *et al.* Modeling , Validation and Verification of Cell- Scaffold Contact Measurements over Terabyte-sized 3D Image Collection. 3951–3953 (2016). doi:10.1111/jmi.12303.Florczyk

101. Hotaling, N. A. *et al.* Training to Improve Precision and Accuracy in the Measurement of Fiber Morphology. 1–14 (2016). doi:10.1371/journal.pone.0167664

102. Aldo, P. B., Craveiro, V., Guller, S. & Mor, G. Effect of Culture Conditions on the Phenotype of THP-1 Monocyte Cell Line. **70,** 80–86 (2013).

103. Daigneault, M., Preston, J. a., Marriott, H. M., Whyte, M. K. B. & Dockrell, D. H. The identification of markers of macrophage differentiation in PMA-stimulated THP-1 cells and monocyte-derived macrophages. *PLoS One* **5,** (2010).

104. Kumar, N., Gammell, P., Meleady, P., Henry, M. & Clynes, M. Differential protein expression following low temperature culture of suspension CHO-K1 cells. **13,** 1–13 (2008).

105. Vergara, M., Becerra, S., Berrios, J., Osses, N. & Reyes, J. Differential Effect of Culture Temperature and Specific Growth Rate on CHO Cell Behavior in Chemostat Culture. **9,** 1–6 (2014).

106. Kaufmann, H., Mazur, X., Fussenegger, M., Bailey, J. E. & Zu, C.-. Influence of Low Temperature on Productivity , Proteome and Protein Phosphorylation of CHO Cells. (1999).

107. Russell, R. A. *et al.* Segmentation of fluorescence microscopy images for quantitative analysis of cell nuclear architecture. *Biophys. J.* **96,** 3379–3389 (2009).

108. Balomenos, A. D. *et al.* Image analysis driven single-cell analytics for systems microbiology. *BMC Syst. Biol.* **11,** 1–21 (2017).

109. Sliusarenko, O., Heinritz, J., Emonet, T. & Jacobs-Wagner, C. High-throughput, subpixel precision analysis of bacterial morphogenesis and intracellular spatio-temporal dynamics. *Mol. Microbiol.* **80,** 612–627 (2011).

110. Goñi-Moreno, Á., Kim, J. & de Lorenzo, V. CellShape: A user-friendly image analysis tool for quantitative visualization of bacterial cell factories inside. *Biotechnol. J.* **12,** (2017).

111. Stylianidou, S., Brennan, C., Nissen, S. B., Kuwada, N. J. & Wiggins, P. A. SuperSegger: robust image segmentation, analysis and lineage tracking of bacterial cells. *Mol. Microbiol.* **102,** 690–700 (2016).

112. Ducret, A., Quardokus, E. M. & Brun, Y. V. MicrobeJ, a tool for high throughput bacterial cell detection and quantitative analysis. *Nat. Microbiol.* **1,** 1–7 (2016).

113. Puck, Theodore T.; Marcus, Philip I., Cieciura, S. J. Clonal growth of mammalian cells in vitro. *J. Exp. Med.* **103(2),** 273–283 (1956).

114. Missirlis, D. The effect of substrate elasticity and actomyosin contractility on different forms of endocytosis. *PLoS One* **9,** (2014).

115. Solon, J., Levental, I., Sengupta, K., Georges, P. C. & Janmey, P. A. Fibroblast adaptation and stiffness matching to soft elastic substrates. *Biophys. J.* **93,** 4453–4461 (2007).

116. Frank, S. R., Adelstein, M. R. & Hansen, S. H. GIT2 represses Crk- and Rac1-regulated cell spreading and Cdc42-mediated focal adhesion turnover. *EMBO J.* **25,** 1848–1859 (2006).

117. Pang, J. *et al.* Automatic neuron segmentation and neural network analysis method for phase contrast microscopy images. *Biomed. Opt. Express* **6,** 4395 (2015).

118. Kerrison, N. & Bulpitt, A. Automated Segmentation of Cell Structure in Microscopy Images. *2014 Int. Conf.*

Comput. Vis. Theory Appl. 98–105 (2014).

119. Legland, D., Arganda-Carreras, I. & Andrey, P. MorphoLibJ: Integrated library and plugins for mathematical morphology with ImageJ. *Bioinformatics* **32,** 3532–3534 (2016).

120. Takaku, M. *et al.* An in vitro coculture model of transmigrant monocytes and foam cell formation. *Arterioscler. Thromb. Vasc. Biol.* **19,** 2330–2339 (1999).

121. Van Varik, B. J. *et al.* Mechanisms of arterial remodeling: Lessons from genetic diseases. *Front. Genet.* **3,** 1–10 (2012).

122. Marleau, S. *et al.* EP 80317, a ligand of the CD36 scavenger receptor, protects apolipoprotein E-deficient mice from developing atherosclerotic lesions. *FASEB J.* **19,** 1869–1871 (2005).

123. Joseph, S. B. *et al.* Synthetic LXR ligand inhibits the development of atherosclerosis in mice. **99,** 7604–7609 (2002).

124. Saeed, O. *et al.* Pharmacological Suppression of Hepcidin Increases Macrophage Cholesterol Efflux and Reduces Foam Cell Formation and Atherosclerosis. **30308,** (2011).

125. Weber, T. *et al.* Arterial Stiffness, Wave Reflections, and the Risk of Coronary Artery Disease. *Circulation* **109,** 184–189 (2004).

126. Tsamis, A., Krawiec, J. T. & Vorp, D. a. Elastin and collagen fibre microstructure of the human aorta in ageing and disease: a review. *J. R. Soc. Interface* **10,** 1–22 (2013).

127. Zarkoob, H., Bodduluri, S., Ponnaluri, S. V., Selby, J. C. & Sander, E. A. Substrate Stiffness Affects Human Keratinocyte Colony Formation. *Cell. Mol. Bioeng.* **8,** 32–50 (2015).

128. Guilak, F. *et al.* Review Control of Stem Cell Fate by Physical Interactions with the Extracellular Matrix. *Stem Cell* **5,** 17–26 (2009).

129. Tee, S., Fu, J., Chen, C. S. & Janmey, P. A. Cell Shape and Substrate Rigidity Both Regulate Cell Stiffness. *Biophysj* **100,** L25–L27 (2011).

130. Discher, D. E., Janmey, P. & Wang, Y. Tissue Cells Feel and Respond to the Stiffness of Their Substrate. *Science (80-.).* **310,** 1139–1144 (2005).

131. Irwin, E. F. *et al.* Modulus-dependent macrophage adhesion and behavior. *J. Biomater. Sci. Polym. Ed.* **19,** 1363–1382 (2008).

132. Yashima, Saburo; Morohashi, Shoichi; Saito, F. Single Particle Crushing under Slow Rate of Loading. *Sci. reports Res. Institutes, Tohoku Univ. Ser. A, Physics, Chem. Metall.* **28,** 116–133 (1979).

133. Sakr, S. W. *et al.* The Uptake and Degradation of Matrix-Bound Lipoproteins by Macrophages Requires an Intact Actin Cytoskeleton , Rho Family GTPases , and Myosin ATPase Activity. *J. Biol. Chem.* **276(40),** 37649–37658 (2001).

134. Kruth, H. S. *et al.* Macropinocytosis Is the Endocytic Pathway That Mediates Macrophage Foam Cell Formation with Native Low Density Lipoprotein. **280,** 2352–2360 (2005).

135. Doherty, T. M. *et al.* Calcification in atherosclerosis : Bone biology and chronic inflammation at the arterial crossroads. *Proc. Natl. Acad. Sci. U. S. A.* **100,** 11201–11206 (2003).

136. Erba, E. *et al.* DNA Damage , Cytotoxic Effect and Cell-Cycle Perturbation of Hoechst 33342 on L E I 0 Cells In Vitro. **6,** (1988).

137. Knight, M. M., Roberts, S. R., Lee, D. A. & Bader, D. L. Live cell imaging using confocal microscopy induces intracellular calcium transients and cell death. *AJP Cell Physiol.* **284,** C1083–C1089 (2003).

138. Bojarski, M. *et al.* End to End Learning for Self-Driving Cars. 1–9

139. Schroff, F. & Philbin, J. FaceNet : A Unified Embedding for Face Recognition and Clustering.

140. Esteva, A. *et al.* Dermatologist-level classification of skin cancer with deep neural networks. *Nature* **542,** 115–118 (2017).

141. Johnson, J. W. Adapting Mask-RCNN for Automatic Nucleus Segmentation. 1–7 (2018).

142. Bhooshan, S., Garg, A. & Marshall, W. Automated Nuclei Detection.

143. Ulman, V. *et al.* An objective comparison of cell-tracking algorithms. *Nat. Methods* **14,** 1141–1152 (2017).

144. Gurari, D. *et al.* How to collect segmentations for biomedical images? A benchmark evaluating the performance of experts, crowdsourced non-experts, and algorithms. *Proc. - 2015 IEEE Winter Conf. Appl. Comput. Vision, WACV 2015* 1169–1176 (2015). doi:10.1109/WACV.2015.160

145. Ljosa, V., Sokolnicki, K. L. & Carpenter, A. E. Annotated high-throughput microscopy image sets for validation. *Nat. Methods* **9,** 637 (2012).

146. Ding, Q. *et al.* Permanent Alteration of PCSK9 With In Vivo CRISPR-Cas9 Genome Editing. 488–492 (2014). doi:10.1161/CIRCRESAHA.115.304351

147. Krause, Jonathan; Johnson, Justin; Krishna, Ranjay; Fei-Fei, L. A Hierarchical Approach for Generating Descriptive Image Paragraphs. *IEEE Conf. Comput. Vis. Pattern Recognit.* 317–325 (2017).

148. Xia, X. & Kulis, B. W-Net: A Deep Model for Fully Unsupervised Image Segmentation. *arXiv* (2017).

149. Moriya, T. *et al.* Unsupervised Pathology Image Segmentation Using Representation Learning with Spherical K-means. *arXiv* (2018). doi:10.1117/12.2292172

150. Reyes, J. & Lahav, G. Leveraging and coping with uncertainty in the response of individual cells to therapy. *Curr. Opin. Biotechnol.* **51,** 109–115 (2018).